The Dissertation Committee for Karl Matthew Martin certifies that this is the approved version of the following dissertation:

ACOUSTIC MODIFICATION OF SOOTING COMBUSTION

Committee:

Ofodike A. Ezekoye

David T. Blackstock

Noel T. Clemens

Mark F. Hamilton

Matthew J. Hall

Ronald L. Panton

Acoustic Modification of Sooting Combustion

by

Karl Matthew Martin, B. S., M. S.

Dissertation
Presented to the Faculty of the Graduate School of
the University of Texas at Austin
in Partial Fulfillment
of the Requirements
for the Degree of

Doctor of Philosophy

The University of Texas at Austin
May 2002

ProQuest Information and Learning Company
300 North Zeeb Road
PO Box 1346
Ann Arbor, MI 48106-1346

ACKNOWLEDGMENTS

I first need to thank my wife, Cheryl, who has been my motivation and my strength through these years of graduate school. It's the things we do together that we do best. Thanks also to my parents. The mechanical intuition I learned from Dad and the creativity I learned from Mom are what have made me a successful engineer.

Thanks to my advisor, Dike Ezekoye. Besides being a great boss and a great friend, you gave me the chance to take advantage of every opportunity presented to me through my graduate career, and helped me through the long days when it seemed like this thing would never end. I hope some day I can repay you for all you've done for me. Thanks also to the members of my doctoral committee, David Blackstock, Noel Clemens, Matthew Hall, Mark Hamilton, and Ronald Panton. Your insight and guidance have contributed much to this research.

Thanks to Cindy Palacios and Terry Alger, fellow graduate students in the lab who have been great people to consult with on myriad topics over the years. Thanks also to the many friends who have made these years fun, especially Marc and Sue Polanka, Ryan McKay and Renee Nieh, Stan Farnsworth, and Kyle Fisher. You all make my life better.

Thanks to Dennis Wilson and Darrin Willauer, my bosses at Nanotechnologies Inc. You've been very supportive of me when I needed to take time to work on this doctorate, and I deeply appreciate it.

Through most of my graduate career, I was supported by a Fannie and John Hertz Foundation Graduate Fellowship. The Foundation's support allowed me the freedom to pursue this work without financial worries, for which I am very grateful.

April 30, 2002

ACOUSTIC MODIFICATION OF SOOTING COMBUSTION

Publication No. _____________

Karl Matthew Martin, Ph.D.
The University of Texas at Austin, 2002
SUPERVISOR: Ofodike A. Ezekoye

Acoustic-combustion interactions have interesting potential as a pollution control technology. Studies by a number of authors have shown it to be effective in reducing emissions of NO_x and CO from flames, and suppression of soot in flames has been indicated qualitatively. In order to understand the interaction of high intensity acoustics with sooting flames, a laminar co-flow acetylene burner apparatus was developed which allowed a gaseous jet flame to be acoustically driven at sound pressure levels above 140 dB. It was found that the acoustic field could somewhat increase soot emissions from the flame, and could also completely suppress soot emissions from the flame, depending on the frequency and intensity of the acoustic driving. Acoustic driving changed the shape of the flame, creating a pulsed shape. High speed video of the pulsations showed that the acoustic driving was imposing a velocity on the flame that was proportional to, and of the same order as, the first-order RMS acoustic particle velocity. This velocity is comparable to, or greater than, the fuel jet velocity.

Spectrometry measurements performed on the flame showed that the temperature of the flame increased with increasing acoustic forcing. Extinction measurements in the flame were used to reconstruct the radial distribution of soot in the flame. The measurements show quantitatively that, just as with the emitted soot, low power acoustic forcing increased the in-flame soot concentration

somewhat, but high power forcing suppressed soot formation almost completely. The in-flame soot profile and the spectrometry measurements were also performed on partially premixed flames, where air was mixed with the fuel to create equivalence ratios from infinity (no premixing) to 3. The results from the two flames were quite similar, demonstrating that the primary effect of the acoustic driving on the flame is to premix air into the fuel just before it burns. While a detailed analysis of the flow patterns in the burner was not performed, the preponderance of the available data indicates that the acoustic driving is causing a synthetic jet flow pattern, which draws air from the burn zone into the fuel tube and premixes it with the fuel before the mixture burns.

TABLE OF CONTENTS

LIST OF FIGURES

1 INTRODUCTION

In 1997, 63% of the United States energy consumption was in the form of liquid petroleum products and natural gas. 58% of that total was consumed in the residential and industrial sectors, where the majority of these fuels is burned in continuous burners, such as the burners in industrial boilers and radiant heaters, oil- and gas fired forced-air heaters, and residential gas stoves, rather than an intermittent burner like an internal combustion engine. Because of the safety risks associated with storing and transporting combustible mixtures, almost all of these continuous burning devices use diffusion flames, where the fuel and air come into contact only as they enter the flame zone. This safety issue is, rightfully, the dominant consideration in spite of the fact that diffusion flames tend to produce much more pollutants per unit of heat released than premixed flames. Hence, nearly 36% of the United States' energy needs are met by diffusion flames in continuous burning devices of one form or another (EIA, 1997).

Pressuring the market for these continuous-burning diffusion flame devices are a host of new pollution regulations on the major pollutants they create, including carbon monoxide (CO), nitrogen oxides (NO_x), and hydrocarbons (e.g. methane, CH_4). Many new combustion devices are covered by New Source Performance Standards (NSPS) mandated by the United States Environmental Protection Administration (EPA) in order to meet the goals of the Clean Air Act and its various amendments. These performance standards limit the amount of various pollutants that can be emitted by an installation (Benítez, 1993). Although failure to meet the applicable NSPS often leads to installation of pollution remediation equipment, the most effective form of remediation is often suppressing the original formation of the pollutant. Liquid-fueled burners have problems, not only with the gaseous pollutants described above, but also with soot production. Oil-fired burners tend to produce large amounts of soot particles. The EPA's new standard for ambient particulate matter less than 2.5 µm in diameter, PM 2.5, bears on soot more than previous particulate standards, since the sources of these small particles are almost entirely anthropogenic (EPA, 1997). Soot also represents unburned fuel, therefore a loss in efficiency for the burner. Sooting burners generate plumes of black smoke which are politically embarrassing for industry. Finally, soot deposits on the burner and downstream equipment reduce the effectiveness of that equipment, leading to periodic shutdowns to clean combustors, heat exchangers, and exhaust stacks. For this reason, research that can reduce the amount of soot generated by diffusion flames is of definite interest in industry.

Given that soot is known to be a problem, the processes which lead to soot formation and growth should be examined, in the interest of finding ways to modify them. Following Bockhorn (1994), the formation of soot begins with the pyrolisation of fuel in the intense heat near the reaction zone of a flame to produce molecules of short hydrocarbons, especially acetylene. (This step is short circuited when acetylene is the incoming fuel. The abundance of acetylene to drive later steps explains the tremendous sooting tendencies of acetylene.) One of the bonds in the triple bond in the acetylene molecule breaks and links with others, forming unsaturated hydrocarbon chains. When the chains reach a length of 5 or 6 carbons, they are able to form aromatic (e.g. benzene) rings. Further acetylenes and larger molecules bond with the benzene to form a polyaromatic hydrocarbon (PAH), which is a single molecule with a multiple ring structure. The aromatics also react with each other to grow the ring structures. The PAH eventually grows large enough that it precipitates from the gas phase to the solid phase and becomes a soot nucleus.

The soot nuclei at this point are quite small, on the order of 1 nanometer in diameter. They continue to grow by two processes. First, the unsaturated gaseous fuels deposit on the solid particle, a phenomenon called surface growth. Surface growth determines the total volumetric concentration of soot in the flame. Far downstream of the flame, surface growth also involves the condensation of liquid fuels onto the surface of the soot particle. Second, soot nuclei can agglomerate to form larger structures. Agglomeration determines the size of the soot particles.

Opposing the processes of surface growth and agglomeration is oxidation, which reduces the size of soot particles by reacting the hydrocarbons on the outside of the particle with oxygen to form gaseous combustion products. In a methane diffusion flame, soot particles are formed in the flame, but usually fully oxidize, so that soot emissions from methane diffusion flames are generally very small.

The author has performed research on the use of acoustics to agglomerate soot particles well after the combustion event has occurred (Martin, 1997; Martin and Ezekoye, 1997). The strong acoustic fields used in those experiments were seen to create significant flows in a closed chamber, flows that could in fact blow out the polystyrene flame used to create the soot particles. A hypothesis was formed that these flows might be used to modify soot production in flames that were both more stable and analytically simpler and more repeatable than a burning pile of polystyrene.

The research described here tests that hypothesis. Acoustic driving is used to suppress soot generation in an acetylene diffusion flame. Acetylene is used as a fuel because it produces large amounts of soot, but it is a gaseous fuel, which presents less complications and difficulties in understanding than a liquid fuel. The study focuses on soot suppression and the forces driving it, but also touches on the emissions of gaseous pollutants from the flame.

Chapter 2 of this work reviews the current understanding of the nature of soot particles, including their fractal geometry and their fluid mechanical and optical properties. Chapter 3 reviews previous work on sooting flames and acoustic-flame interactions. Chapter 4 describes the experimental system. Chapter 5 examines the changes in flame shape that result from acoustic driving, and infers data about the flow velocities caused by the acoustic field. Chapter 6 describes the global pollutant emissions from the flame, including two forms of soot measurements, and gaseous pollutant measurements. Chapter 7 describes the total and spectral radiation emitted by the flame, and describes a model of soot cloud emissivity that yields estimates of the flame temperature. Chapter 8 describes in-flame soot concentration measurements done with a laser extinction apparatus. The data from this chapter is numerically manipulated to produce profiles of the soot distribution in the flame. Chapter 9 discusses spectrometry and in-flame soot measurements made on partially premixed flames. The similarities between the data from the partially premixed flames and the acoustically driven flames are used to support the conclusion that acoustic driving in this system serves primarily to drive premixing of the air into the flame. Chapter10 presents final conclusions.

2 REVIEW OF SOOT PROPERTIES

A treatise on soot and sooting flames depends strongly on an understanding of the properties and structure of soot. This chapter reviews the current best understanding of soot geometry, fluid mechanical properties, and optical properties.

2.1 Soot geometry: Fractals

Soot tends to exhibit irregular, odd shapes, such as those shown in figure 2.1. It is made up of primary particles that are roughly spherical and have a fairly uniform diameter. The spheres are agglomerated to form chains. The picture on the left shows clearly some of the individual primary spheres. Note that the primaries are fairly uniform in diameter. The picture on the right gives an idea of the size to which soot agglomerates can grow.

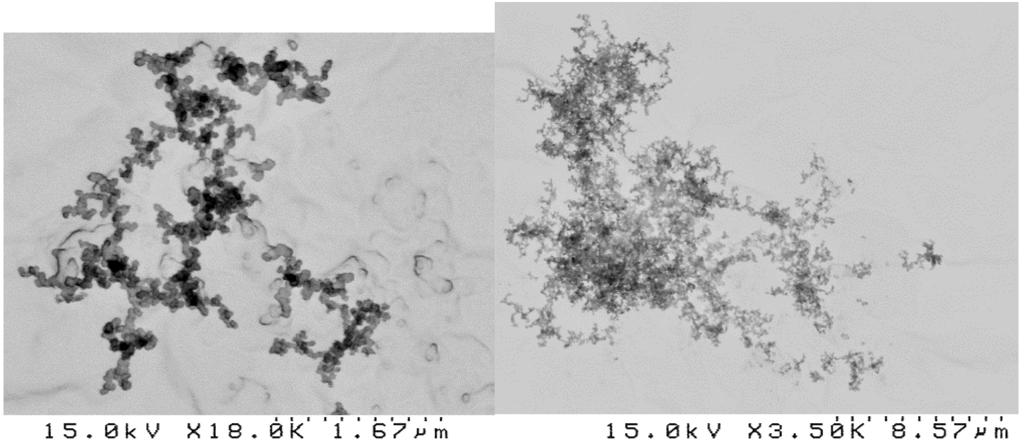

Figure 2.1. Scanning Electron Micrographs of Soot Particles.
Scanning Electron Micrographs courtesy Cindy Palacios.

Up until fairly recently, many scientists struggled to find some mathematical description of soot geometry. For example, Medalia and coworkers describe different methods of characterizing soot aggregate structure with sets of four experimentally determined parameters (1967) and with graphical comparison charts (1971). Nothing of great elegance was found until Mandelbrot (1977) wrote his first treatise on fractal geometry, which inspired Forrest and Witten (1979) to apply the concept of non-integer, or fractal, dimensions to smoke particles. Mandelbrot's subsequent publication of the widely read *Fractal Geometry of Nature* (1983) cemented the idea of applying fractal geometry to many irregular natural shapes, and many combustion researchers began to examine soot as a fractal particle.

The basic premise of fractal geometry is that a fractal object can be broken into a set of miniscule parts, called initiators, which cannot be broken further without a significant change in initiator structure. The initiator of the soot particles in figure 2.1 is the primary sphere. The smallest set of initiators that has the gross structure of the fractal object known as the generator. The generator for a soot particle might be a double "Y" branching structure. Generators are then assembled into larger and larger structures which demonstrate a gross structure similar to the generator.

One important property demonstrated by fractal objects is limited scale invariance. A line (of infinite extent) has a self-similar structure across all length scales. Whether one looks at a small segment of the line, or pulls back to look at an immense length, a line is still a line. In both cases, its shape is the same. A fractal particle has a self-similar structure from the scale of the generator to the scale of the particle. Below the scale of the generator, the shape tends toward that of the initiator, and then some part of the initiator. Well above the scale of the particle, the shape tends toward a point. In the intermediate scales, the structure displays self-similarity.

More directly relevant to the current discussion are expressions of the volume of fractal soot particles. If the primary spheres are modeled as having a uniform diameter and composition, their volume is known, and the volume of the particle is determined by that of the primary spheres and the number of primaries. The number of primaries, N, is given by (Mandelbrot, 1983):

$$N = k_f \left(\frac{D}{d_o} \right)^{D_f} \qquad \text{eq. 2.1}$$

where:
D is some length scale of the particle
d_o is a length scale of the primary (generally the diameter)
k_f is a proportionality constant known as the fractal prefactor
D_f is the fractal dimension

Examining this equation makes it clear why D_f is referred to as a dimension. A line of primaries would have a fractal dimension of 1; the number of primaries in the line is proportional to the length of the line. This is true even if the line were not straight, such as the outline of a circle. A flat disk of particles would have a fractal dimension of 2. A sphere of particles would have a fractal dimension of 3. However, the dimension is called fractal because it need not be an integer. Experimental determinations of fractal dimensions for soot particles tend to give fractal dimensions around 1.75, as will be reviewed below.

The preferred particle length scale D varies according to the preference of the researcher. One obvious one would be the geometric diameter D_{ge}, which is the diameter of the smallest sphere that circumscribes the aggregate. Magill

(1991) and Rogak and Flagan (Rogak and Flagan, 1990) used the geometric diameter in their works, and set k_f equal to 1, which gives the intuitive result:

$$N = \left(\frac{D_{ge}}{d_o} \right)^{D_f} \qquad \text{eq. 2.2}$$

For a line of primaries ($D_f = 1$) this obviously gives the correct number of aggregates. However, for larger fractal dimensions, setting k_f to 1 implies perfect packing of primaries into an aggregate. This is not generally the case.

Most authors have used a less intuitive length scale, the radius of gyration of the particle, R_g. The radius of gyration is important because it directly affects optical scattering properties computed using Rayleigh Debye Gans theory, which will be discussed later. Because of the assumption of identical primaries, the radius of gyration can be expressed as:

$$NR_g{}^2 = \sum_{i=1}^{N} r_i{}^2 \qquad \text{eq. 2.3}$$

where r_I is the distance from the center of mass of the aggregate to the center of the *i*th primary. Several authors (Hess et al., 1986; Rogak and Flagan, 1990; Cai et al., 1993) relate D_{ge} and R_g with the equation

$$R_g = \frac{D_{ge}}{2} \sqrt{\frac{D_f}{D_f + 2}} \qquad \text{eq. 2.4}$$

This equation is always presented with neither derivation nor reference. Note though that, for a sphere, $D_f = 3$ and $R_g = \frac{D_{ge}}{2} \sqrt{\frac{2}{5}}$ (Meriam and Kraige, 1986). This is not consistent with eq. 2.4, which gives $R_g = \frac{D_{ge}}{2}\sqrt{\frac{3}{5}}$. To derive this relation, start with the definition of the radius of gyration,

$$R_g = \sqrt{\frac{J}{M}} \qquad \text{eq. 2.5}$$

where J is the mass moment of inertia of the aggregate and M is the mass of the aggregate. The density of the aggregate of geometric radius R_{ge} varies with radius r as:

$$\rho(r) = \rho_o \left(\frac{r}{R_{ge}}\right)^{D_f - 3} \qquad r \le R_{ge} \qquad \text{eq. 2.6}$$

$$\rho = 0 \qquad r > R_{ge}$$

ρ_o is the density of the aggregate material. ρ is the average density of the spherical shell of radius r. The shell is actually part solid material of density ρ_o and part empty space, in proportions that lead to the average given in eq. 2.6. The mass of the particle is:

$$M = \int_0^{R_{ge}} 4\pi r^2 \rho(r) dr = \frac{4}{D_f}\pi\rho_o R_{ge}{}^3 \qquad \text{eq. 2.7}$$

and the moment of inertia is:

$$J = \int r^2 dM = 2 \int_0^{R_{ge}} \left(\int_0^{\sqrt{R_{ge}{}^2 - x^2}} r^2 \rho_o \left(\frac{\sqrt{r^2 + x^2}}{R_{ge}} \right)^{D_f - 3} (2\pi r) dr \right) \qquad \text{eq. 2.8}$$

$$J = \frac{8}{3(D_f + 2)} \pi \rho_o R_{ge}{}^5$$

The radius of gyration is then

$$R_g = R_{ge} \sqrt{\frac{2}{3} \frac{D_f}{D_f + 2}} \qquad \text{eq. 2.9}$$

This equation gives the correct relation for a compact sphere.

Efforts have been made to determine three dimensional structure from two dimensional soot micrographs. Cai *et al.* (1993) used multiple shades of gray in their processing to detect the overlap of primaries in 2-D soot micrographs. Samson *et al.* (1987) have used stereopairs (micrographs of soot taken at 2 different rotations, then viewed in a special apparatus which allows three dimensional structure to be seen) as an aid in counting overlapping primaries in small aggregates. Köylü *et al.* (1995) used both computer simulated aggregates and aggregates captured from actual flames to compare analysis with 2-D projections (such as single TEM micrographs), and analysis using full 3-D structure (such as TEM stereopairs). They all found that the value of D_f is not changed by projection of a 3-D aggregate onto a 2-D surface. The ratio of the actual (3-D) radius of gyration of an aggregate to the projected (2-D) radius of gyration has been found to be 1.1:1 (Samson et al., 1987) to 1.24:1 (Köylü et al., 1995). N is adjusted for projection by the relation:

$$N = k_a \left(\frac{A_a}{A_p} \right)^{\alpha} \qquad \text{eq. 2.10}$$

where A_a is the projected area of the aggregate and A_p is the projected area of a primary. Köylü *et al.* (1995) and Medalia and Heckman (1971) both give values for α of 1.1, while they give k_a as 1.16 and 1, respectively.

The number of primaries is then given by the equation

$$N = k_f \left(\frac{R_g}{d_o} \right)^{D_f} \qquad \text{eq. 2.11}$$

where all of the quantities have been adjusted for projection. The volume of an aggregate particle is simply N times the volume of a primary, and a volume equivalent diameter, D_{ve}, is defined as the diameter of a sphere with the same volume as the aggregate:

$$D_{ve} = d_o \left[k_f \left(\frac{R_g}{d_o} \right)^{D_f} \right]^{\frac{1}{3}} \qquad \text{eq. 2.12}$$

The density of the primaries is generally taken to be that of amorphous carbon, 1950 kg/m^3, and the mass of the aggregate can be calculated. This density value is consistent with experimental findings of Dobbins and Megaridis (1990) for soot.

The findings of various researchers regarding d_o, D_f, and k_f are listed in table 2.1. It is interesting to note that the last two researchers, who worked with flames in microgravity, found that the soot structure parameters listed here did not change strongly from the terrestrial case. However, the aggregate size (i.e. D_{ge}) approached 1 mm, up to 1000 times larger than aggregates formed by flames at normal gravity. This is because the lack of buoyant flows in microgravity flames allows soot particles much more time to sit in regions where they can grow.

For this work, the values of Köylü and Faeth (1994) for laminar acetylene diffusion flames (d_o = 53 nm, D_f = 1.74, k_f =8.1) will be used for the soot above the flame, as they were measured above flames similar to the one being investigated here.

Table 2.1 Fractal Geometry Properties of Soot

Reference	d_o (nm)	D_f	k_f	Flame	Method
(Mountain et al., 1986)	____	1.7 to 1.9	___	________	Comp. simulation
(Samson et al., 1987)	30	1.5 to 1.6	___	Laminar acetylene diffusion flame	TEM
(Megaridis and Dobbins, 1990)	22	1.62	5.8	Laminar ethene diffusion flame	TEM
(Forrest and Jr., 1979)	4	1.5-1.9	___	Evaporated and condensed metals and silica	TEM
(Cai et al., 1993)	8 – 18	1.57 – 1.93	___	Premixed methane/oxygen flames	TEM
(Köylü and Faeth, 1992)	30-51	1.7-1.79	5.8	Various turbulent diffusion flames	TEM
(Köylü and Faeth, 1994)	21-54	1.73-1.77	8.1	Ethylene and acetylene laminar diffusion flames	TEM
(Köylü et al., 1995)	_____	1.82	8.5	Various laminar diffusion flames	TEM, Comp. simulation
(Nyeki and Colbeck, 1994)	50	1.89 – 2.19	1	Butane laminar diffusion flame	Millikan Cell
(Colbeck and Wu, 1994)		1.4-1.96		Butane laminar diffusion flame	Millikan Cell
(Ku et al., 1995)	15-45	1.41-1.93	___	Propane & ethylene laminar diffusion flames, some microgravity	TEM
(Ito et al., 1994)	50	_____	___	Butane laminar diffusion flames	TEM

2.2 Fluid Mechanics of Fractal Particles

The mechanics or particles in fluids can be broken into two areas: the behavior of particles in response to fluid motion (drag), and changes in the behavior of a fluid due to the presence of particles. This discussion focuses on the first point. The second can be important in certain fields, such as the rheology of slurries, but is generally neglected in the soot and aerosol communities.

The drag that a fluid flow exerts on small particles is often represented by the radius or diameter of some sphere that exhibits a drag characteristic similar to the particle in question, which is referred to here as an equivalent drag length. Two different variants of this technique are common in the literature. Both depend on the Stokes drag law, which gives the drag force F_{drag} on a sphere of diameter D in response to the velocity U with which it is moving through a medium of viscosity μ:

$$F_{drag} = 3\pi\mu UD \qquad \text{eq. 2.13}$$

One equivalent drag length is the aerodynamic diameter, which is the diameter of a spherical water droplet with the same terminal settling velocity in air as the particle in question. This is commonly used in aerosols, where the low viscosity of gaseous media leads to an appreciable (though small) settling velocity. Mathematically,

$$D_{ae} = \left(\frac{18\mu U_{ts}}{\rho_w g} \right) \qquad \text{eq. 2.14}$$

where μ is the viscosity of the fluid medium (usually air), U_{ts} is the real terminal settling velocity of the particle in question, ρ_w is the density of water (1000 kg/m^3), and g is the acceleration due to gravity (9.81m/s^2).

The other common equivalent drag length is the hydraulic radius. It is the radius of a hypothetical spherical particle with the same density as the actual particle in question (ρ_p) that has the same terminal velocity in response to an actual applied force, $F_{applied}$. This quantity is commonly used in colloids, where settling is almost negligibly slow, and forces are often applied to particles by means other than gravity, such as electrostatic fields. The hydraulic radius is mathematically defined by:

$$R_h = \frac{F_{applied}}{6\pi\mu U} \tag{eq. 2.15}$$

Several authors have investigated the relation of R_g and R_h. Using either numerical simulations (Meakin et al., 1985; Chen et al., 1987; Rogak and Flagan, 1990) or experiments (Wiltzius, 1987), it has been shown consistently that the ratio $\delta = R_g/R_h$ approaches a constant value. Rogak and Flagan (Rogak and Flagan, 1990) in particular examine clusters with a fractal dimension of 1.79, a value similar to that found in soot studies (Köylü and Faeth, 1992) and aerosol agglomeration simulations(Mountain et al., 1986). They found that the limiting value of δ for these aggregates is 1.12, which is achieved for $N > 1000$. For aggregates even as small as $N = 10$, δ is not more than 10% from its asymptotic value.

A caveat here is that all of the above work has been done in liquids, or with a continuum assumption in the computer simulation. A question remains regarding the non-continuum effects. For small particles, a Cunningham slip correction factor is often used to account for slip (Allen and Raabe, 1985). Slip is almost certainly significant, since the mean free path of air at STP is 67 nm, larger than a soot primary. Conversion between equivalent drag lengths and soot geometry parameters like D_{ge} and R_g should take slip into account. Allen and Raabe (1985) show that, for 2 and 3 particle aggregates, the slip correction factor should not be based solely on the primary diameter. The value of the primary diameter should be modified by a factor that increases with the number of primaries in the aggregate. While they are able to establish that the factor is not simply the square or cube root of the number of particles, they do not present a theory to explain the data they have. Due to the dearth of data in the literature on this topic, slip will be neglected here.

The hydrodynamic radius and the aerodynamic diameter can be related by setting the force $F_{applied}$ in eq. 2.15 to the actual weight of the particle and solving for the terminal settling velocity of the aggregate in air. The actual weight of the particle is simply the weight of a primary times the number of primaries in an aggregate. This leads to the expression:

$$D_{ae} = \sqrt{\frac{N\rho_o\, d_o^3}{2R_h\rho_w}} \qquad \text{eq. 2.16}$$

It is surprising to see the aerodynamic diameter expressed as inversely proportional to a positive power of the hydrodynamic radius. However, this is misleading because the value of N is proportional to R_h^{Df}. Because D_f is greater than 1, D_{ae}, R_h, and N all increase together. Substituting R_g and simplifying:

$$D_{ae} = \sqrt{\frac{k_f}{2}\beta\frac{\rho_o}{\rho_w}R_g^{D_f-1}d_0^{3-D_f}} \qquad \text{eq. 2.17}$$

2.3 Optics of Fractal Particles

The optical properties of soot are of interest for two reasons. First, soot particles are the primary radiators of heat from flames. This is clearly seen in a Bunsen burner. When the Bunsen burner is run with the air intake at the base fully closed, soot forms in the flame and it takes on a bright yellow color. This color is consistent with blackbody radiation from a body at flame temperatures, 1800 to 2500 K. When the Bunsen burner is run with the air intake open, less soot is formed and the flame is a translucent blue color, and not terribly bright. The dominant radiation mechanism is emission from hot gases, which is relatively weak compared to blackbody emission. Understanding soot optics then helps to predict the behavior of flames in situations where radiation is the dominant heat transfer mechanism. It helps in the modeling of flames by clarifying the modeling of radiant heat losses. It also helps in the development of nonintrusive optical diagnostics, which allow researchers to probe the inner structure of flames.

In contrast to the previous sections of this chapter, little compilation was required to develop this section. The discussion here is taken from a few accurate and detailed references. In addition to those references noted in the text, the book by van de Hulst (van de Hulst, 1981) is an excellent and detailed reference for particle optics.

In this work, the optical properties of soot will be applied in the context of an optical extinction measurement, which uses the attenuation of a laser beam to find the volume fraction of the soot through which the laser has passed. The extinction measurement relies on the Lambert-Beer law. The transmitted intensity, I, of a monochromatic beam passing through a homogeneous polydisperse aerosol is related to the initial intensity I_O by

$$\frac{I(z=L)}{I(z=0)} = \exp(-\tau S)$$ eq. 2.18

where S is the beam path length and τ is the aerosol extinction coefficient or turbidity. A starting point for analysis of the turbidity is

$$\tau = \int_0^\infty C_{ext} n(D) dD$$ eq. 2.19

where $n(D)$ is the aggregate number concentration in the size range dD about D , and C_{ext} is the aggregate extinction cross-section. C_{ext} is primarily a function of the wavelength λ, the complex index of refraction m, the diameter of the primaries d_o, and the aggregate radius of gyration R_g. C_{ext} is the sum of two parts, the absorption cross section C_{abs} and the scattering cross section C_{sca}.

The index of refraction m is of vital importance to particle optics. The value of m that will be used here is $1.57 + 0.56i$, which is commonly attributed to Dalzell and Sarofim (1969). There are questions as to the history and accuracy of this value (Smyth and Shaddix, 1996), and some suggest other values, but no other value of the index of refraction of soot has gained widespread acceptance.

The form of the expressions for the cross sections depends on the optical model used. The simplest model is Rayleigh scattering, which applies for particles that are much smaller than the wavelength. Specifically, the value of the optical size parameter $x_p << 1$, where x_p is defined by

$$x_p = \frac{\pi d_p}{\lambda}$$ eq. 2.20

Soot primaries are one tenth to one hundredth the wavelength of visible light, so they are reasonably represented with Rayleigh scattering. Use of Rayleigh scattering neglects aggregate structure entirely.

The absorption cross section of a primary is given by:

eq. 2.21

$$C_{abs}^{p} = \frac{4\pi x_p^3}{k^2} E(m)$$

k is the wave number, $2\pi/\lambda$. *E(m)* relates the complex index of refraction of the particle to its light absorption. It is given by:

eq. 2.22

$$E(m) = \mathrm{Im}\left[\frac{m^2 - 1}{m^2 + 2}\right] = \mathrm{Im}\left[G(m)\right]$$

The function *G(m)* will be used again later. If the index of refraction is real only, then the particle does not absorb light. It does still scatter.

The scattering cross section can be expressed in differential or integrated forms. The differential scattering cross section applies only to light which enters with a certain polarity, either parallel or perpendicular to the plane formed by the incoming and scattered light rays, and is scattered at a particular angle, as shown in figure 2.2.

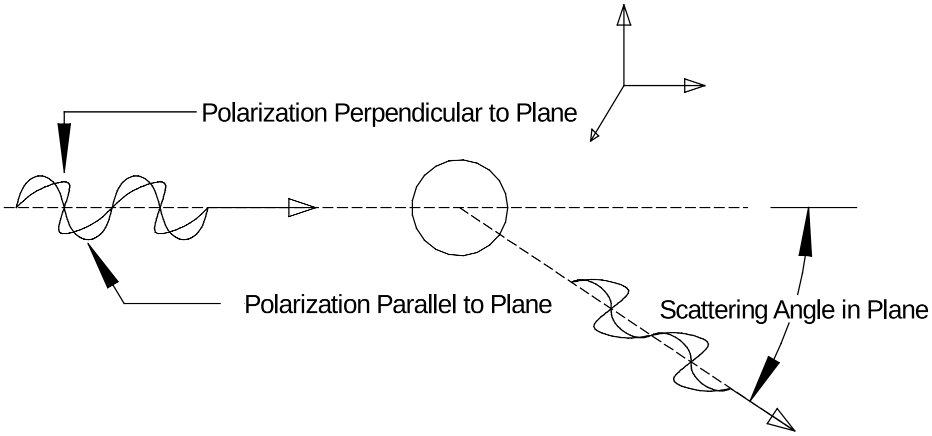

Figure 2.2. Differential scattering of both parallel and perpendicular polarizations. The ratio of the light intensity leaving the particle to that incoming can be different for the two polarizations.

The integrated, or total scattering cross section, is the differential scattering cross section integrated over all directions. The scattering cross sections for Rayleigh scattering are given by (Farias et al., 1995)

eq. 2.23

$$C_{sca}^{p} = \frac{8\pi x_p^6}{3k^2} F(m)$$

$$C_{\perp}^{p} = \frac{x_p^6}{k^2} F(m)$$

$$C_{\parallel}^{p} = \frac{x_p^6}{k^2} F(m)\cos^2\theta$$

where:

eq. 2.24

$$F(m) = |G(m)|^2 = \left|\frac{m^2-1}{m^2+2}\right|^2$$

The differential scattering cross sections of a 53 nm sphere in 488 nm incident light are shown graphically in figure 2.3. The perpendicular cross section does not vary with scattering angle. The parallel cross section has a zero at 90°, and is symmetric about 90°.

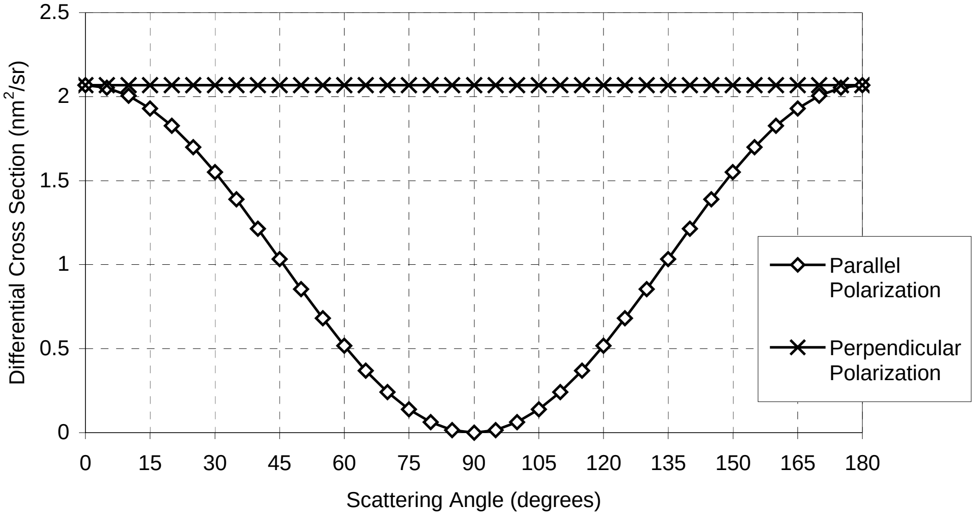

Figure 2.3. Differential scattering cross sections for Rayleigh scattering.

In spite of the fact that soot primaries can reasonably be represented as Rayleigh scatterers, it has been found that using Rayleigh scattering alone to model soot extinction tends to greatly overpredict the volume fraction of soot in an extinction measurements taken above the flame zone, where aggregates can become large (Köylü and Faeth, 1994). Rayleigh scattering is still used for soot extinction measurements inside the flame itself, where there has been little time for aggregation (Lin and Faeth, 1996). Rayleigh scattering tends to be quite weak compared to other scattering models, and so pure Rayleigh scattering has been abandoned in favor of other scattering models.

Spheres of arbitrary size are rigorously modeled using Mie scattering. This model is named after Gustav Mie, who solved the full set of Maxwell's equations inside and outside of the sphere to find the scattering of an incident plane wave by a homogeneous sphere (van de Hulst, 1981). The complete solution is analytical, but computationally complex, with infinite sums of Legendre polynomials and Bessel functions. For this reason, Mie scattering has only become a widely used tool in the past 20 years, with the development of inexpensive fast computers. There are now Mie scattering calculators that run over the world wide web (e.g. MieCalc, (2000), http://www.lightscattering.de/MieCalc/eindex.html).

When Mie scattering is used in soot, the scattering profile is used to find an equivalent diameter. For purposes of comparison with Rayleigh Gans scattering (below), the equivalent diameter will be arbitrarily interpreted here as the volume equivalent diameter D_{ve}, from eq. 2.12. A plot of the Mie scattering cross section of a particle with the volume equivalent diameter of a soot particle with d_o = 53 nm, and N = 1000, giving D_{ve} = 530 nm, is shown in figure 2.4. While Rayleigh scatterers show symmetry between forward and backward scattering, particles in the Mie scattering regime tend to scatter forward much more than backward. In this case, scattering at 0° is two orders of magnitude stronger than at 180°. The parallel polarization shows a minimum near 90°, though not precisely at it, and minimum is greater than zero, unlike the Rayleigh case.

The absorption cross section in Mie scattering is not directly defined. Rather, the extinction and scattering cross sections are defined, and the absorption cross section is simply the difference of the two. For the particle in question, Mie theory puts the extinction cross section at 5.9 x 10^5 nm^2, the scattering cross section at 2.7 x 10^5 nm^2, and the absorption cross section at 3.2 x 10^5 nm^2.

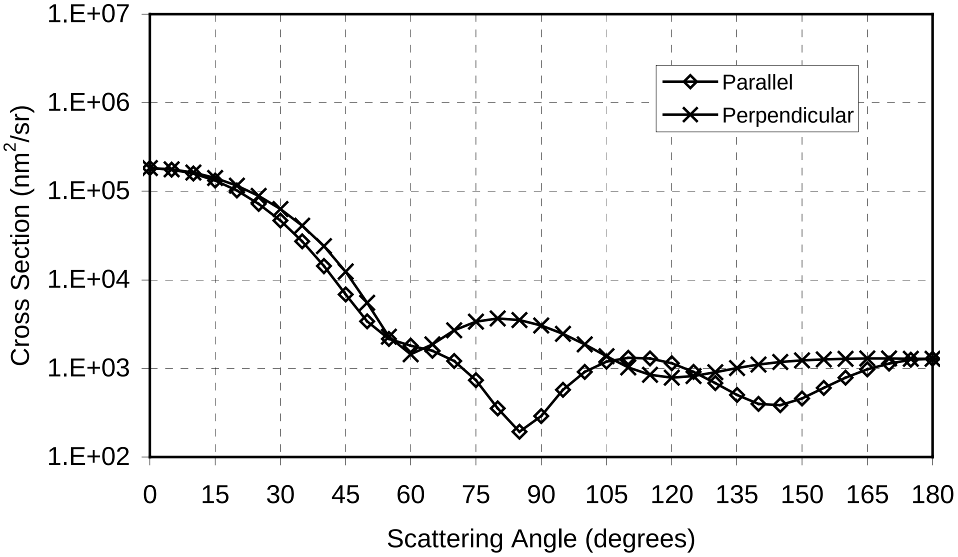

Figure 2.4 Mie Scattering Patterns, calculated with MieCalc 1.2 (Michel, 2000). N = 1000, d_o = 53 nm, D_{ve} = 530 nm, λ=488 nm.

The use of Mie scattering with soot is an approximation because of the irregular particle structure. The value of Mie theory is that it is an exact solution for a sphere, even though getting numbers from it is computationally challenging. If, however, the particle in question is nowhere near spherical, Mie theory is quite an expensive and complex approximation, without theoretical support.

The accuracy of Mie theory for fractal aggregates is also not supported in the literature. Iskander *et al.* (1989) performed a sophisticated scattering simulation, solving Maxwell's equations over a discretized volume in which existed either a sphere or a branched aggregate particle. The scattering behavior calculated for the sphere agreed with Mie theory. However, the scattering for the branched chains exhibited quite a different behavior. Farias *et al.* (1995) compared scattering profiles developed with Iskander *et al.*'s method with those of the Rayleigh Gans scattering theory. They showed very good agreement. The Rayleigh Gans model has become the most widely used model for soot optics.

Rayleigh Gans scattering is an extension of Rayleigh scattering to particles which are potentially much larger than the incident wavelength. The requirement of the model is that the particle be composed primarily of a medium with an index of refraction very near 1. A set of discrete scattering centers is distributed throughout the particle. This model was first developed to simulate scattering of X-rays by loosely bound electrons in an atom or molecule, but in this case the medium is air and the discrete scattering centers are soot primaries. This is a reasonably accurate description of soot structure. The Rayleigh Gans theory is described in detail and tested against more detailed computational simulations by Dobbins and Megaridis (1991) and Berry and Percival (1986).

In the Rayleigh Gans (RG) model, the aggregates are considered to have such a sparse distribution of primaries that each primary receives, absorbs, and scatters incident light independently. Note that this sparse distribution requirement would not be met by aggregates with fractal dimensions that are much above 2. The absorption cross section of an aggregate is then simply C_{abs} for the primary sphere from Rayleigh theory times the number of spheres in the aggregate:

eq. 2.25

$$C_{abs}^{RG} = N\frac{4\pi x_p^3}{k^2}E(m)$$

The scattering profile is more complex. It starts with a definition of the average index of refraction of the aggregate, including the open space and the primaries within its bounds. The average index of refraction m_{ps} is defined by:

$$G(m_{ps}) = \eta_v G(m) \qquad \text{eq. 2.26}$$

$$\eta_v = \frac{Nd_o^3}{D_{ge}^3}$$

As N increases, the real part of m_{ps} tends strongly to 1, and the imaginary to zero. With ten primaries in the aggregate, both are within 10% of their terminal value. With 100 primaries, they are within 2%.

The index of refraction comes into the absorption and scattering cross sections through the function $G(m)$. Note that substituting D_{ge} and $G(m_{pe})$ into the absorption cross section eq. 2.21 gives eq. 2.25, so the formula is consistent. The scattering profile depends on m by way of F, which is $|G|^2$. This means that the scattering profile is proportional to the square of the number of primaries in the aggregate.

The scattered rays from different primaries interfere constructively and destructively at the receiver depending on the primaries' positions in the aggregate, and the positions of the source and the receiver (Mountain and Mulholland, 1988). This behavior is modeled using a structure function, which is generally between 0 and 1. The total and directional scattering cross sections are as follows:

$$
\begin{aligned}
C_{sca}^{RG} &= N^2 \frac{8\pi x_p^6}{3k^2} F(m) g_{struct}(kR_g) \\
C_{\perp}^{RG} &= \frac{x_p^6}{k^2} F(m) f_{struct}(qR_g) \\
C_{\parallel}^{RG} &= \frac{x_p^6}{k^2} F(m) \cos^2(\theta) f_{struct}(qR_g)
\end{aligned}
\qquad \text{eq.2.27}
$$

where g_{struct} is the integrated structure function, and f_{struct} is the directional form of the structure function. Each function is averaged over all orientations of the aggregate with respect to the incoming ray of light.

Mountain and Mulholland (1988) used a random walk simulation to create a set of simulated fractal aggregates, and then did scattering and interference calculations on the aggregates in 216 different orientations. They showed that the behavior of the structure function changes in small and large angle regimes. The final form of the scattering cross sections is given below:

$$
\begin{aligned}
g_{struct}(kR_g) &= \left(1 + \frac{4}{3D_f} k^2 R_g^2\right)^{-Df/2} \\
f_{struct}(qRg) &= \begin{cases} \exp\left(-\dfrac{q^2 R_g^2}{3}\right); & q^2 R_g^2 \le 1.5 D_f \\ \left(\dfrac{3D_f}{2eq^2 R_g^2}\right)^{D_f/2}; & q^2 R_g^2 > 1.5 D_f \end{cases} \\
q &= 4\pi \sin(\theta/2)/\lambda
\end{aligned}
\qquad \text{eq. 2.28}
$$

While the structure functions themselves tend to 0 with increasing N, the scattering cross sections are proportional to N^2. In order to compare Rayleigh Gans scattering from an aggregate and Rayleigh scattering by N primaries, multiply the *N* by the structure functions. Given D_f of 1.78 (Köylü and Faeth, 1994) and λ of 488 nm (the wavelength of an argon ion laser, used extensively later) *Ng* converges to 19.85, meaning that the aggregate scattering cross section is almost 20 times the sum of the cross sections of the primaries.

Figure 2.5 shows the RG scattering cross section for the same aggregate considered in figure 2.4. The RG values tend to be larger than the Mie values, and the curves are smoother. RG theory shows preferential scattering in the forward direction, similar to the Mie curve for the same particle, but it also shows a null at 90° for parallel polarization, as Rayleigh scattering did. Figure 2.6 shows the ratio of RG to Mie differential cross sections at each angle. The RG values tend to be about 10 times greater. The oscillations in the ratios generally reflect the Mie scattering oscillations, while the null is due to RG theory.

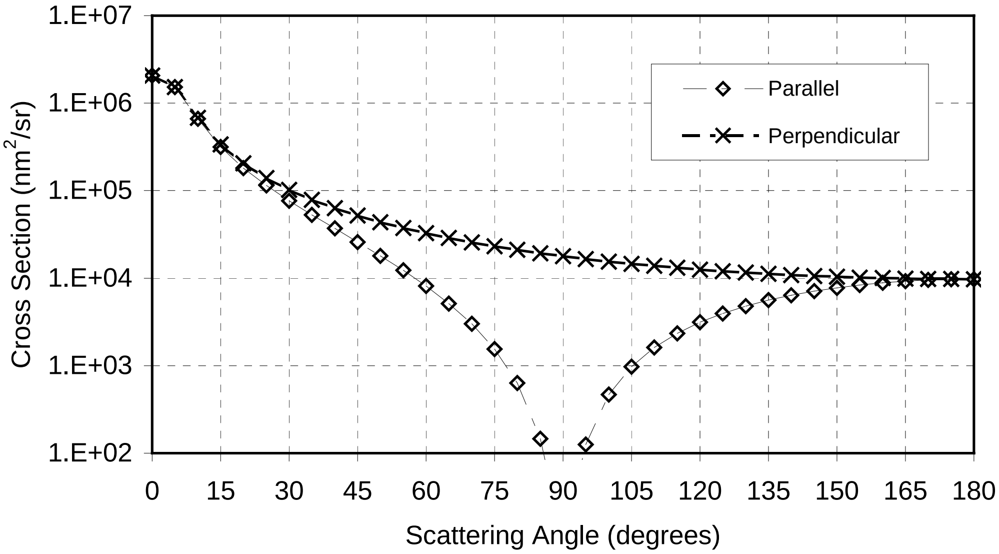

Figure 2.5. Differential scattering cross sections of a soot aggregate in Rayleigh Gans theory. N = 1000, d_o = 53 nm, D_{ve} = 530 nm, λ=488 nm

Under RG theory, the total scattering cross section of the aggregate being considered is 3.4 x 10^5 nm^2. This is only slightly more than the value from Mie theory, which is surprising in light of figure 2.6. The reason for the discrepancy is that the bulk of the scattering happens between 0 and 45°, where the ratio of differential cross sections is generally lower. The absorption cross section is 7.8 x 10^5 nm^2, which is more than twice the Mie value. The extinction cross section is 1.1 x 10^6 nm^2.

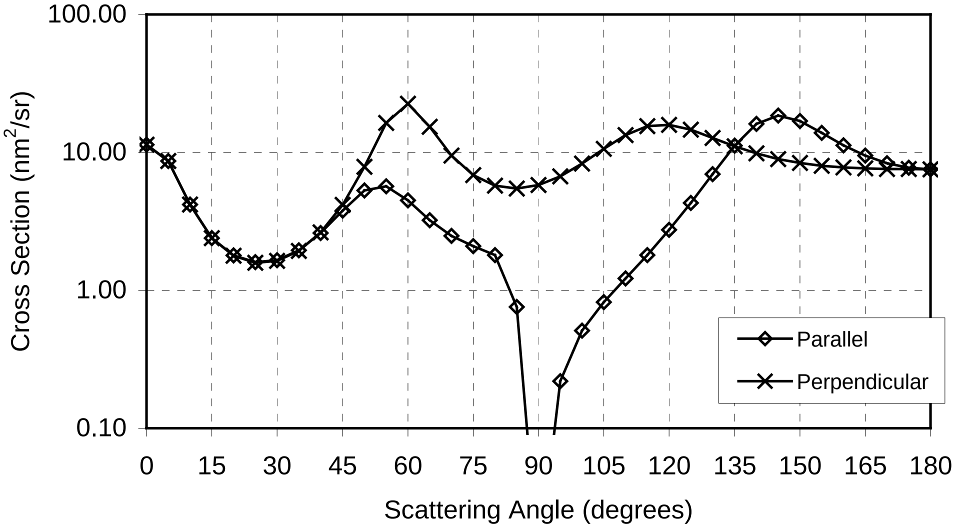

Figure 2.6. Ratio of Rayleigh Gans to Mie differential scattering cross sections. N = 1000, d_o = 53 nm, D_{ve} = 530 nm, λ=488 nm.

3 LITERATURE REVIEW: SOOTING AND ACOUSTICALLY DRIVEN FLAMES

3.1 Sooting Flames

Much research has gone into characterizing sooting laminar diffusion flames. Many researchers have used axisymmetric co-flow laminar diffusion flame apparatuses such as the schematic in figure 3.1. In such a system, the fuel enters the burner through a center tube. The air enters the burner through an annular region around the fuel tube. The burners are often small enough that the fuel flow is quite laminar without further conditioning. The airflow is usually straightened and balanced to produce a uniform velocity profile. Because of the large amount of research using these devices, a similar setup is the basis of this research. It is described in detail in the next chapter. In this section, previous experiments in steady sooting flames are discussed.

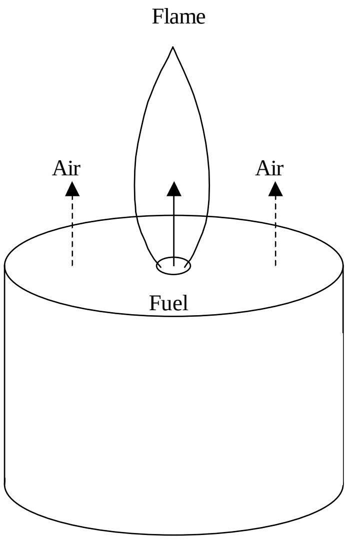

Figure 3.1. Axisymmetric coflow diffusion flame schematic

Santoro and coworkers have done several studies in this area. Santoro et al. (1983) used an axisymmetric geometry and measured soot particle distributions in ethane flames using a combined laser scattering and extinction experiment. By combining soot extinction and scattering measurements, they were able to calculate soot volume fraction, number density, and particle size. Near the base of the flame, they found that soot is concentrated in an annular region just inside the main reaction zone. Moving up through the flame, the regions with appreciable soot concentrations spread into the center of the flame until the entire flame contains soot particles. They report soot particle diameters as large as 100 nm in the flame, although the numerical results are suspect because they used Rayleigh scattering for their optical measurements. Santoro et al (1987) report laser Doppler velocimetry, extinction and scattering, and temperature measurements in the same system. They found that the rate of soot formation in the annular high-soot region of the flame tends to be constant. This is also a high temperature region of the flame, being just on the fuel side of the reaction front. Increasing the fuel flow rate increased the residence time of soot particles in the annular region, leading to larger particles. They found similar time-temperature growth behavior along the centerline of the flame, provided that they introduced a minimum temperature for soot formation in the flame. This temperature was 1300 K in their flame. Because the formation of soot was much stronger in the hot annular part of the flame, it is this part of the flame which controls the transition from non-smoking (no soot emissions) to smoking flames.

Santoro and Miller (1987) discuss soot formation in both the axisymmetric burner and a Wolfhard Parker slot burner. This slot burner has a center channel of fuel, with an air channel on each side of it. The channels have long aspect ratios, so that measurements taken near the center will reflect an essentially two-dimensional process. They show that soot particles are formed by pyrolisation of fuel to form certain chemical precursor species such as acetylene and the vinyl radical ($C_2H_3^*$). These species in turn form benzene rings. Further acetylene molecules attach to the particles to form linked aromatic ring structures called polyaromatic hydrocarbons (PAH's). These molecules eventually become so large that they can no longer exist in the gas phase, and they become solid particles. The incipient soot particles are 5 to 10 nm in diameter. Acetylene species continue to attach to the particles, causing surface growth. At the same time, the primary particles begin to agglomerate, forming chains of primaries. The black, solid soot particles radiate heat well, and so their presence tends to cool the flame by radiation. The soot particles eventually encounter oxygen diffusing into the flame. At low fuel flow rates, sufficient oxygen can enter the flame to fully oxidize the soot particles. At higher flow rates, the soot particles have more time in the high temperature fuel rich zone, so they grow larger before beginning to oxidize. Some of the particles are not consumed, and soot is emitted from the flame.

Puri, Santoro, and Smyth (1994) measured the competing processes of soot and carbon monoxide oxidation in the axisymmetric burner. They used laser induced fluorescence to determine the concentration of OH· radicals throughout the flame. They correlated this data with primary particle size information determined using the thermophoretic sampler of Dobbins and Megaridis (1987). They found that the primary oxidizer of soot is the OH· radical, rather than molecular oxygen. As this radical is also the primary oxidizer of CO, there is a competition between the two carbon species for OH· radicals. Soot is found to generally win that competition, which implies that the presence of soot in a flame, even in cases when the soot is fully oxidized and does not exit the flame, can contribute to higher emissions of carbon monoxide.

A number of other researchers have examined sooting laminar diffusion flames. Kang *et al.* (1997) examined soot formation in axisymmetric co-flow and counterflow flames. A counterflow flame has two jets, one with oxidizer and one with fuel, flowing directly at each other from opposite sides of a reaction zone. This geometry leads to a flat disk flame with well-characterized, controllable strain rates. The concentration of nitrogen in the fuel and oxidizer were varied to adjust the position of the flame relative to the stagnation plane between the two jets. It was found that the flame could be positioned on the fuel side of the stagnation plane. Soot was always formed between the flame zone and stagnation plane. In the "normal" case of pure fuel and air as the oxidizer, the flame was on the oxidizer side of the stagnation plane. The fuel diffuses "upstream" against bulk flow to reach the flame. The fluid mechanical drag of the soot is such that it cannot diffuse to the flame. It is advected away from the flame, so that little of the soot formed by the flame is oxidized. In the inverse case, the fuel is diluted with over 80% nitrogen, and the oxygen has only 30% nitrogen in it. The flame is on the fuel side of the stagnation plane, and the oxygen must diffuse "upstream" to reach the flame. In this case the soot still forms on the fuel rich side. It is carried by the bulk flow into the flame where it is oxidized.

Du, Axelbaum, and Law (1988) used a similar counterflow burner to examine the effect of strain on the soot formation process. They found that strain rate can suppress soot formation in C_1 through C_4 alkane flames. They defined four strain rate limits. The first is the soot luminosity limit, above which a yellow, luminous soot zone is no longer observed optically. The second is the particle light scattering limit, above which light scattering signals from soot particles cannot be detected. The third is the precursor fluorescence limit. The PAH's which are the precursors of soot particles exhibit broadband fluorescence in response to excitation by a 488 nm argon ion laser. The fluorescence signal is not detected for strain rates above the precursor fluorescence limit. The final limit is the extinction limit, above which the flame extinguishes and cannot burn. They found that, for the alkane fuels tested, the soot luminosity and soot particle light scattering limits are generally close together, perhaps within the experimental error. These limits increase with the number of carbons in the fuel. The precursor fluorescence limit is 2 to 4 times the luminosity and scattering limits. The precursor limit increases with number of carbons as well, but the ratio of the two signals decreases. The extinction limit is the highest strain rate, at 2 to 4 times the precursor limit. It does not increase monotonically with number of carbons as the other limits do, but peaks for ethane and then decreases for propane and butane. Extrapolation of this trend to larger molecules may indicate that the "strain rate window" where soot is suppressed but the flame is not extinguished closes for heavy fuels where soot formation can be stronger, but this is not tested, probably because the burner is not designed for liquid flames. Also, strain rate limits for the most strongly sooting gaseous fuels like acetylene are unfortunately not investigated.

Another investigation of soot suppression by strain was undertaken by Lin and Faeth (1996). They used a low pressure (0.1 atm) burner to minimize the effects of buoyancy in the flame relative to hydrodynamic strain. This is intended to mimic the conditions in a turbulent jet flame, where strain effects are much stronger than buoyant effects. The burner had an axisymmetric co-flow geometry, and the ratio of the fuel and oxidizer velocities was varied to produce different strain rates in the flame zone. They found that strain produced in this way could suppress soot formation in the heavily sooting fuel rich zone just inside the flame sheet. Soot was formed within the core of the flame, but the relatively cool core did not cause enough surface growth for the soot particles to avoid being oxidized at the flame tip.

Another method of suppressing soot that has been investigated is premixing some air into the fuel stream before the combustion zone. Chakraborty and Long (1968) reported early work in the area. They captured soot from ethylene and ethane flames on filters and analyzed it in a gas chromatograph. They found that the emissions of soot and soot precursors increased with small amounts of oxygen addition to the fuel line of a diffusion flame. However, larger amounts of oxygen addition reduced the soot emissions below the level of the diffusion flame. Mitrovic and Lee (1998) used laser induced incandescence to measure the spatially resolved soot volume fractions within a partially premixed ethylene diffusion flame. They found that the soot in the flame and the flame length increased as the premixing increased from a pure diffusion flame to an equivalence ratio between 10 and 20. For lower equivalence ratios, the volume fraction of soot in the flame and the flame length both decreased below the level of a pure diffusion flame. When the equivalence ratio is 1, almost no soot is formed in the flame. Hura and Glassman (1988) partially premixed flames of propane and ethane in both coflow and counterflow geometries. In counterflow ethene flames they found results similar to those of Mitrovic and Lee. More soot was emitted from a slightly premixed flame than from a pure diffusion flame. Below an equivalence ratio of 6, the soot in the flame decreased sharply. They showed that the addition of small amounts of oxygen to ethene flames causes more rapid pyrolysis of fuel molecules to form soot precursor species. The smallest soot particles form earlier in the flame than they would with no oxygen in the flames. The log of the specific surface growth rate of soot (measured in cm^3 /second of soot formation/ cm^2 of existing particle surface area) was found to be inversely proportional to temperature in the range from 1000 to 2000 K, which covers many flames. The surface specific growth rates for both ethene and propane flames actually collapsed onto a single curve when plotted against temperature. This shows the great effect that early formation of soot particles can have. The sooner surface area forms, the longer growth can occur in hot regions of the flame. The addition of further oxygen to the fuel eventually causes soot oxidation to overtake formation, and suppresses soot in the flame.

Other authors have investigated in more detail the chemistry behind the effects of partial premixing. Hwang *et al.* (1998) found a similar increase of soot with small additions of oxygen to the fuel in ethylene diffusion flames. They used simulations of chemical kinetics to show that oxygen reacts with acetylene (C_2H_2) molecules to form CH_2, which combines with acetylene to form C_3H_3. The C_3H_3 then combines with itself or acetylene to form a ring structure, the beginning of a polyaromatic molecule. McEnally and Pfefferle (2000) used inflame gas species sampling to extend this understanding, by showing that partial premixing of the ethylene fuel in a coflow diffusion flame tends to break the double and triple bonds in species with even number of carbons, forming species with odd numbers of carbons. This leads especially to increased concentrations of methane and C_3 species. The C_3 species react with themselves to form benzene, which was found in much higher concentrations in the partially premixed flames than in the nonpremixed flames.

3.2 Acoustic - Flame Interactions

Research in pulsating flames and other acoustic-flame interactions can be broken roughly into small and large scale devices. The small scale devices have less complicating effects, but are also farther from industrially viable devices. Each is considered below.

3.2.1 Small Scale

Smyth's research group at the National Institute of Standards and Technology conducted several studies into the behavior of acoustically driven methane/air diffusion flames. Smyth *et al.* (1993) forced a laminar methane co-flow diffusion flame at 10 Hz through a speaker acting on a plenum in the fuel supply tube just before the burner. They showed that the flame and the soot in the flame both would divide in to discrete lobes due to the forcing. They showed that the light scattering signal from the soot in the flame increased by a factor of 5. This is due to either an increase in soot volume fraction or particle diameter, but they were not able to discern which in that study. A year later, Shaddix *et al.* (1994) reported the extinction measurements needed to verify that there was a 4 to 5 times increase in the soot volume fraction of the pulsed flame versus the unpulsed flame. Kaplan *et al.* (1996) performed simulations that showed that the increase in soot volume fraction in this flame was caused by longer residence times in rich, high temperature areas in the flame.

Strayer *et al.* (1998) performed experiments using a laminar co-flow methane diffusion flame in a 2-D Wolfhard Parker slot burner, rather than the axisymmetric geometry used by Smyth's group. They drove the two air plenums and the fuel plenum with separate speakers, allowing independent air and fuel actuation, although the control signals were the same (amplitude and phase) for this study. They showed that acoustic driving could be used to reduce the luminosity of the flame, and that various time-luminosity tracks (e.g. ramps, square waves, and constants) could be achieved using closed-loop control of the system, with the speakers as the actuators, the luminosity as the controlled variable, and a photodiode as the sensor.

Lovett and Turns (1990) drove the fuel tube of a turbulent propane jet diffusion flame issuing into a quiescent air atmosphere. They used frequencies from 2 to 1300 Hz and amplitudes from 1.7 to 12 m/s. The fuel velocity was 13.5 m/s. They found that low frequency forcing divides the flame into discrete flame regions with a longer flame than the unforced case, while higher frequency forcing (greater than100 Hz) drove substantial increases in mixing and shortening of the flame. In a later study, (1993) they showed that the effectiveness of the acoustic forcing in producing a reaction in the flame depends strongly on the coupling between different parts of the flame structure and the acoustic driving. High frequency driving interacts with mixing vortices to enhance local mixing and combustion rates.

Parikh and Moffat (1981) did not work primarily in a combustion system, but their work is interesting and relevant from the standpoint of actuator design. They examined an air jet that was pulsed by a rotary valve arrangement. The valve is simply a disc with a number of small holes in it at a fixed radius. The air for the jet is directed through the disc at the same radius as the holes, so that the air flow is only open when each hole passes the air line. In between the holes, the air flow is blocked. They found substantial increases in entrainment of ambient air into the pulsed jet versus the unpulsed case, particularly at frequencies which were acoustic resonances for the air jet tube downstream of the rotary valve.

Cook et al (1996) used a piezoelectric driver to modulate the velocity of kerosene feeding a pressure-jet atomizer. By driving the spray feed at 9.0 and 11.8 kHz and a high amplitude, they substantially reduced the average droplet diameter emitted from the spray nozzle. This indicates the potential for improved fuel-air mixing before ignition, which should lead to reduced pollutant emission.

3.2.2 Larger Scale

Quite a bit of research has been done into the interactions of acoustic fields and flames in different situations. Poppe, Sivasegaram, and Whitelaw (1998) showed that NO_x emissions from gaseous and liquid spray diffusion flames in gas turbine combustors could be reduced by up to 40% by creating velocity oscillations in the combustor. The magnitude of the oscillations was not well described in this case, but they seemed to be on the order of the average velocity in the combustor. Pont et al (1998) used acoustic driving of a premixed flame in a dump combustor to achieve high destruction efficiencies of hazardous gases. With sound pressure levels near 150 dB (re 20 μPa) and forcing frequencies of 200 to 1000 Hz, they achieved destruction efficiencies of ethylene and benzene which were one to two orders of magnitude better than the unforced case, indicating that improved mixing was achieved through acoustic forcing. At the same time, reduced levels of hydrocarbons and NO_x were detected in the combustor exhaust gases for the forced case. Haile *et al.* (1996) showed that acoustically forcing the combustion air going to a turbulent fuel oil spray flame can cause a substantial augmentation of the premixing of fuel and air prior to ignition of the spray. Haile *et al.* found that the response of the flame to the acoustic forcing is determined by the Strouhal number, which is the ratio of periodic (in this case acoustic) and convective time scales, the Stokes number, which is the ratio of the acoustic time to the droplet relaxation time, and a parameter Δ, which is the ratio of acoustic and droplet evaporation times. Haile *et al.* used frequencies from 31 to 700 Hz and acoustic velocities from 5 to 10 m/s.

A substantial amount of the research on acoustic-flame interactions has been driven by interest in pulse combustors. Zinn (1992) presents a review of pulse combustion, its benefits and challenges. A pulse combustor is a device which uses periodic heat addition from a combustion process to excite harmonic resonances in a chamber. Figure 3.2 shows a schematic of a pulse combustor. The supply pressures for the fuel and air are elevated above that in the mixer head, forcing flapper valves on the air and fuel inlet to open, admitting air and gas into the mixing chamber. A spark plug in the combustor ignites the air/fuel mixture. As the mixture burns in the partially enclosed space, the pressure increases beyond the air and fuel supply pressures, closing off the flapper valves. The elevated pressure forces gases out of the combustor and down the tail pipe. This reduces the pressure in the combustor and mixer until the flapper valves can again open and admit more air and fuel into the combustor. Hot radicals remaining in the chamber from the previous combustion event ignite the new air/fuel mixture, and the process continues. The combustor will operate in this manner as long as sufficient energy is added to the system to outweigh flow losses in the exhaust system from the combustor. Other designs of pulse combustors are known as Rijke and Schmidt pulse combustors. They operate with different combustor geometries, but the basic principles involved are similar.

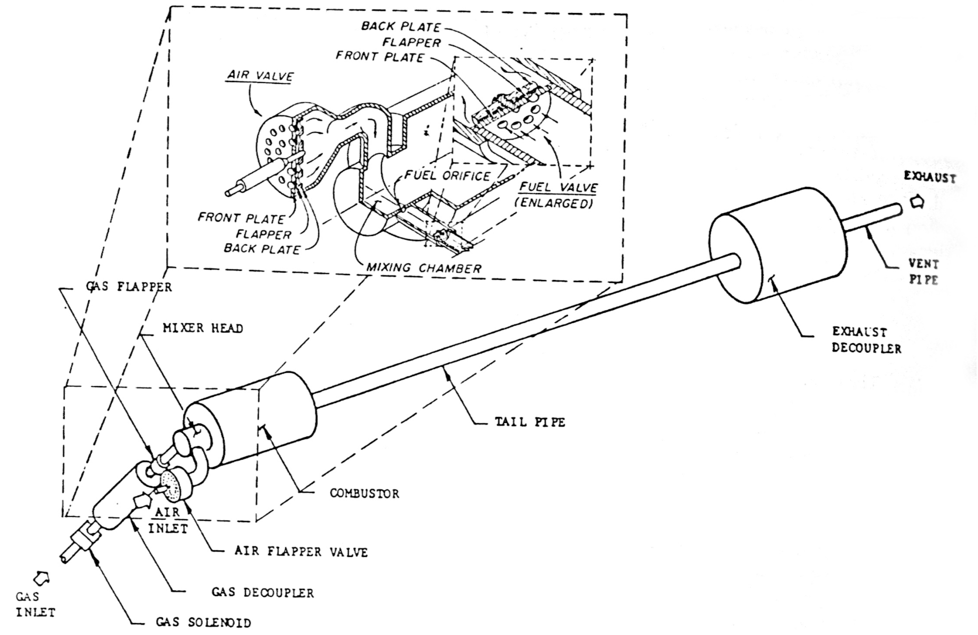

Figure 3.2. Schematic of a mechanically valved, gas fired Helmholtz pulse combustor (Zinn, 1992).

Zinn and co-workers have conducted a large amount of research on pulse combustors. Sujith *et al.* (1992) showed that the acoustic impedance of a pulse combustor is very different in a cold flow configuration, where the pulsations were driven by an external driver on the fuel and air lines, from the impedance of the burner when it is firing and pulsations are driven by the combustor. Sujith *et al.* (1995) used a series of transformations to find an exact solution for one dimensional acoustic fields in ducts with gradients in the average temperature field. This problem is important in situations where combustion and convection cause non-uniformities of the acoustic medium in a combustor. They applied their method to acoustic field in the presence of linear and exponential temperature profiles. Their solution agreed well with experimental profiles of the acoustic field in a non-insulated tube downstream from a pulse combustor, a situation which created a nearly linear temperature distribution in the tube. Sujith *et al.* (1996) showed that evaporation had very little effect on overall droplet drag. The authors theorize that although evaporation is known to increase the form drag (pressure drag), evaporation decreases the friction drag by a similar amount, leading to a negligible change in overall drag.

Matta *et al.* (1996) showed that acoustic driving can improve the rate of mixing in a chamber by several orders of magnitude. They designed a closed chamber with a removable divider in the center and several mounts for acoustic drivers on the outside. One side of the divider was filled with smoke and allowed to become quiescent, while the other side was filled with clean air. When the divider was removed, the acoustic drivers were turned on and the chamber was forced in various resonant modes. The smoke in the chamber was illuminated with a laser sheet and the mixing process was recorded with a high-speed digital camera. The distribution of light and dark pixels in the camera was examined to determine how well mixed the air in the box was. It was found that the mixing rate in the system could be improved by several orders of magnitude by the excitation of the correct modes and the correct orientation of the acoustic drivers around the box. Acoustic streaming was shown to be the major driving factor behind the accelerated mixing. Matta *et al.* (1997) reported a study on the fluid mechanics of solid fuel pyrolysis in an acoustic field. A block of dry ice, subliming at room temperature, was used to simulate pyrolyzing fuel at high temperatures. The block was laid in a chamber with entry and exit ports for driving a constant flow through the chamber, and acoustic driver mounting ports for exciting the chamber in various resonant modes. Stable mean flows of 0.5 to

2 m/s velocity were established in the chambers, and standing waves with peak sound pressure levels of 130 to 150 dB (re 20 μPa) were established. The researchers showed that increased acoustic driving and increased mean flow rates both lead to more rapid transport of the gaseous CO_2 sublimated away from the dry ice. However, for the acoustic effect to be significant, the acoustic velocities over the dry ice block had to be on the order to 1 m/s or greater. This conclusion was further supported by the authors' finding that mixing was much more enhanced when the dry ice block was positioned at an acoustic velocity maximum (pressure node) than an acoustic velocity minimum (pressure antinode) in the standing wave field.

As pulse combustors do represent a significant amount of the research on acoustic-flame interactions, it is worthwhile to note some of the contributions of several other researchers in pulse combustion. Ponizy and Wojcicki (1984) discuss a semi-empirical model of pulse combustors, based on a set of two, linked, well-stirred reactors that effectively modeled actual pulse combustor operation. Margolis (1993) modeled finite amplitude acoustic wave effects in pulse combustors, showing a method by which a theoretically infinite series of equations describing the development of higher harmonics in the combustor can be accurately modeled using less than 20 harmonics. Benelli *et al*. (1992) used Fluent, a commercial computational fluid dynamics code, with reaction rate and turbulence models to find the limit cycle, or periodically stable operating condition, for a pulse combustor. They were successful in predicting self-sustained oscillations, and their results generally agreed with available experimental data regarding the range of achievable operating conditions.

The experiments reported in the literature which most closely resemble the proposed work are those of McQuay and co-workers, in occasional collaboration with Carvalho et al. Figure 3.3 shows the experimental apparatus which they use. The device is based on a Rijke tube pulse combustor, which is essentially an open tube with air being forced through it and a flame situated at a particular spot in the tube. The operation of a Rijke tube is governed by the Rayleigh criterion (Rayleigh, 1945) which states that if heat is added to an acoustically oscillatory mass of gas, the amplitude of oscillation will increase if the heat addition takes place at locations and times when the pressure is higher than the average. Carvalho et al (1989) derived a simple mathematical expression of the Rayleigh criterion and showed the sections of the tube at which a flame should be situated to excite acoustic oscillations of the first, second, and third longitudinal modes. The researchers constructed a Rijke tube with a moveable burner to verify their predictions, and were able to excite the first, second, and third longitudinal modes of the tube by positioning the flame in the appropriate places along the tube.

Dubey *et al.* (1997) used a propane flame to drive the Rijke tube apparatus in its fundamental longitudinal mode. The propane flame was oriented in an annular region in the tube, and an air atomizing nozzle in the center of the annulus injected a spray of liquid ethanol into the combustor. The nozzle sprayed droplets of 3 to 130 μm. The spray flame tended to lift periodically with the acoustic driving, so a small hydrogen pilot flame at the nozzle outlet was used to stabilize the spray flame position. The researchers found that acoustic forcing in the tube, with a peak sound pressure level of 150 dB and a frequency of 80 Hz, caused the ethanol spray flame to shorten from 30 cm (unforced) to 10 cm (forced). The flame color changed from a luminous yellow to a transparent blue, indicating acoustic suppression of soot formation in the flame. The forced flame showed periodic wrinkles in response to the acoustic forcing, and the shape of the flame was much more well-defined in response to the acoustic field. In addition to observing the flame behavior optically, the researchers used a phase-doppler particle analyzer (PDPA) to find the rate of vaporization of the ethanol droplets in the spray. They found that acoustic driving causes an average decrease of 15% in the Sauter mean diameter of the droplets in the spray. The Sauter mean diameter (D_{32}) is a form of average diameter commonly used in sprays research. For a group of droplets divided into n diameter size bins, with the ith bin having N_i members and a median diameter D_I, the Sauter mean diameter is defined as (Eroglu and Chigier, 1991)

$$D_{32} = \frac{\sum_{n} N_i D_i^3}{\sum_{n} N_i D_i^2} \qquad \text{Eq. 3.1}$$

Note that the subscripts 3 and 2 refer to the powers of D_I in the numerator and denominator, respectively. In this notation, a standard arithmetic diameter would be expressed as D_{10},

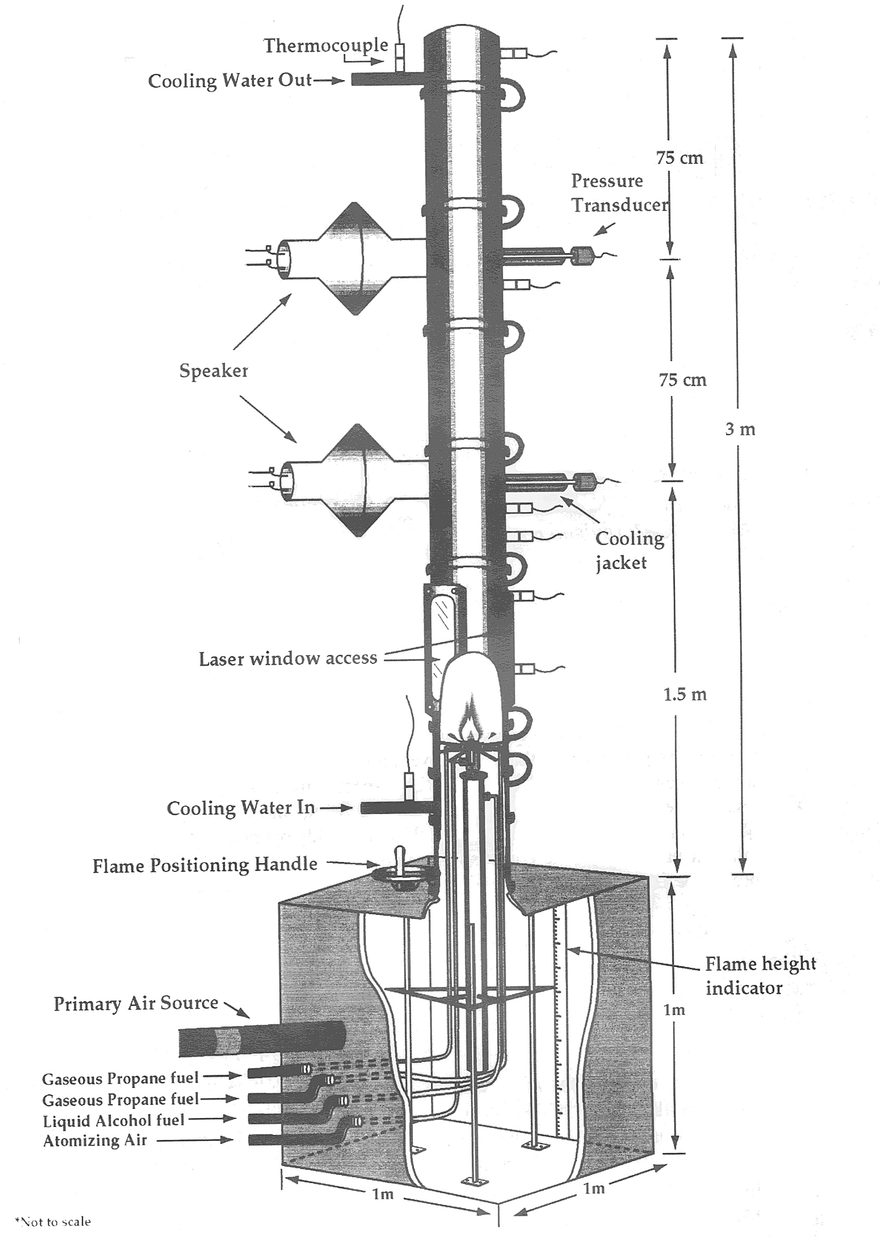

Figure 3.3. Rijke Tube Pulse Combustor with external forcing used by McQuay and coworkers (McQuay et al., 1998).

$$D_{10} = \frac{\sum_n N_i D_i}{\sum_n N_i} \qquad \text{Eq. 3.2}$$

Reduction in D_{32} for constant injection conditions means that the droplets are either evaporating more quickly with acoustic forcing than without, or the acoustics is leading them to break apart more than they otherwise would. This is not surprising given the added convection caused by the intense acoustics. It was found that the reduction in D_{32} is greatest on the nozzle axis near the nozzle tip (26%), and decays both radially and in the direction of jet travel. However, some reduction in D_{32} was seen at every position tested, with both ethanol and water sprays. Furthermore, the number density of the droplets was seen to increase near the nozzle, but did not change further away. This seems to indicate that the acoustic field is causing the breakup of large droplets near the nozzle to proceed more rapidly than it otherwise would, but that the droplets become relatively impervious to breakup once they reach a sufficiently small diameter.

McQuay and Dubey (1998) used the same apparatus shown in figure 3.3 to study the behavior of an evaporating ethanol spray in a non-combusting environment. Rather than using propane burners to excite the tube, they used electrically powered compression drivers to excite the tube in its first three harmonics (54, 106, and 162 Hz). In all cases, the peak sound pressure level in the tube was 150 dB. The spray nozzle was positioned at a distance L/4 from the bottom of the Rijke tube. At this point, the first and third acoustic modes exhibit non-zero particle velocities, while the second mode exhibits a velocity zero, or node. The researchers found that the particle velocity had a strong effect on D_{32} for the spray, as the first and third modes both exhibited very similar spray characteristics, an average decrease in D_{32} of 15%. By contrast, the second mode exhibited almost no change in D_{32}. This behavior correlates well with the magnitude of the particle velocity at the spray location. The velocity at the spray due to first and third modes was 1.68 m/s, while that for the second mode was zero. No significant differences in spray character due to the tripling in frequency from the first to third mode was detected.

McQuay *et al.* (1998) examined the emission of CO and NO from an ethanol spray flame in their apparatus. They drove their device at 80, 156, and 240 Hz (the first, second, and third modes of the Rijke tube with the flame burning), and 140 dB peak sound pressure level. The spray was positioned at L/4 as in the spray study, above, and the excess air was set at 10%, 30%, and 50%. Despite their findings that acoustic forcing in the second mode did not significantly effect the droplet size distribution from the spray, the researchers showed that NO and CO emissions both decreased monotonically with increasing frequency. The researchers were able to show NO emissions reduction to a point below the capability of their device to measure. CO emissions were reduced by a maximum of 90%. In addition, the researchers report that the flame changed from a long, yellow, luminescent flame to a shorter, more blue flame indicating more rapid droplet evaporation and less soot production.

4 EXPERIMENTAL APPARATUS

4.1 Overall Configuration

The experimental system was designed for reasonably small-scale study of the flame. It was also designed for the study of acoustic interactions with a non-premixed flame in a context where the fuel and air are both oscillating, rather than a pulsed fuel experiment. The experimental apparatus used is shown in figure 4.1. A more detailed drawing of the burner is shown in figure 4.2. Supplies of gaseous fuel and air are metered by calibrated rotameters, which have an accuracy of ±2% of full scale and a repeatability of 0.25%. As it goes through the burner, the air passes through a honeycomb, two screens, and a set of glass beads to uniformly distribute the flow. The fuel is passed through a small supply tube in the center of the burner. In the absence of acoustic forcing, the flame is a stable diffusion flame located in the glass cylinder immediately above the burner body. Acetylene is the fuel of choice because it generally causes high emissions of soot, and so provides a large dynamic range for soot measurements. The cold velocity of the acetylene and air are matched at 0.1 m/s. The fuel tube has an inside diameter of 4.32 mm, and a wall thickness of 0.82 mm. In order to safely use acetylene as the fuel, a backflow preventer was placed in the fuel line. It forms a fairly rigid acoustic termination to the fuel tube a distance of 223 mm from the end of the nozzle. The Reynolds number for the cold fuel jet is 45. The inner diameter of the glass cylinder is 70.2 mm, so that the Reynolds number for the air flow is 462. The flame is highly overventilated, with an overall equivalence ratio of 0.045. The chemical energy flow rate, based on the lower heating value of the acetylene fuel, is 75 W.

The exhaust gases travel up the stack, and a sampling probe is positioned in the flow at the center of the stack at a height of 0.65 m above the burner surface. The probe diameter is 9.5 mm (3/8 in). The exhaust flow passes out of the system at a tee just below the acoustic driver, then goes through a muffler and out to the building exhaust system. The exhaust is a totally enclosed system; it is not vented to room air. There is very little likelihood of clean air from the room flowing into the exhaust port and diluting the sample. The exhaust vacuum downstream of the muffler is maintained at 125 Pa (0.5 in H_2O) ± 10% below ambient.

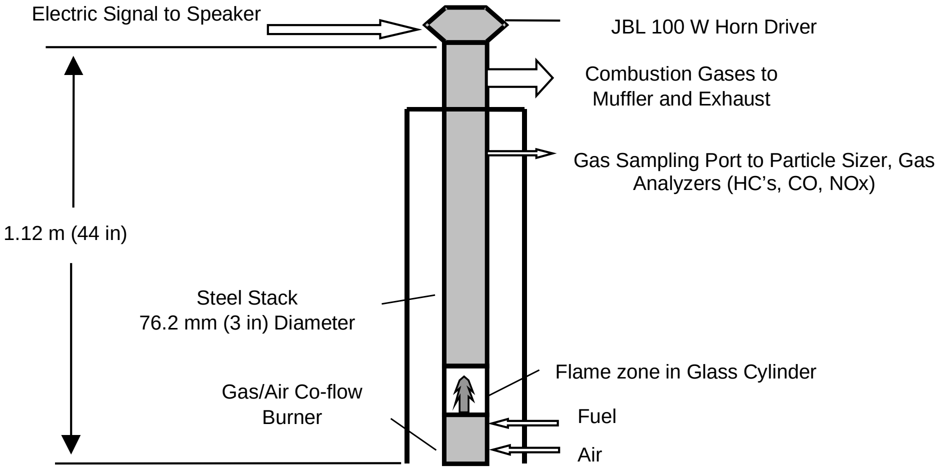

Figure 4.1. Experimental Apparatus

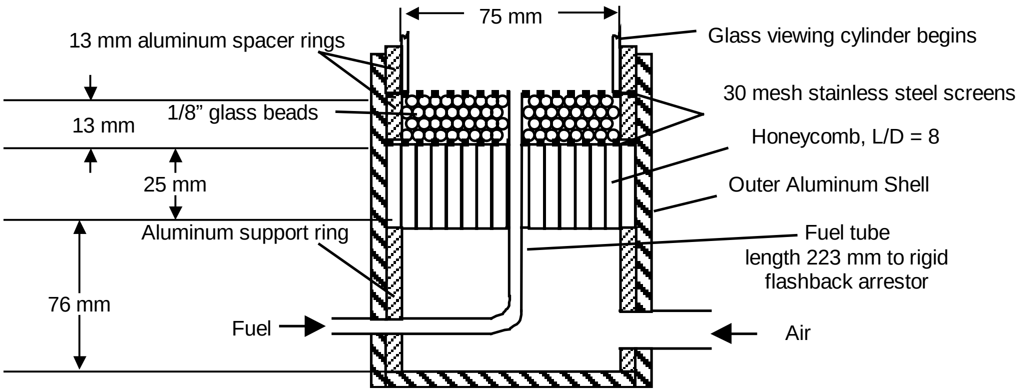

Figure 4.2. Detail of Co-Flow Burner

4.2 Acoustics and Electronics

The acoustic driving in the system is performed by a JBL 2446 J compression driver, with 150 W output capacity (above 1 kHz). The nominal frequency range of the device is 500 Hz to 20 kHz. Frequencies as low as 200 Hz have been achieved with the device, although there is generally some distortion of the sound wave at these low frequencies. The nominal free-field efficiency of the device is 30%, but the efficiency and frequency response of the device in the setup will be largely determined by the standing wave pattern in the system. The compression driver is powered by a QSC MX 2000a 450 W power amplifier, with full power output and flat frequency response from 20 Hz to 20 kHz. The signal is a pure sine wave from a Wavetek 171 function generator. The electrical input to the speaker is measured by a high voltage probe and a Pearson Electronics current transformer outputting 0.1 V/A with an accuracy of ±1% of the reading. The signals from the voltage probe and the current loop are transmitted to a Tektronix TDS 460 digital oscilloscope which internally multiplies the signals to generate the power waveform sent to the speaker, then measures the RMS power transmitted. Due to the warm gases circulating near the speaker diaphragm, and the low frequencies used in this study (with corresponding high diaphragm displacements, which place high current requirements on the coil), high power operation tends to cause rapid failure of the magnetic coil in the speaker. In order to extend coil life, the power used in this study is limited to 10 W and below. Coolant air was injected radially into the space between the exhaust tee and the speaker, in order to protect the speaker from the hot exhaust gases. The flow rate of the coolant air was limited so that the pressure in the exhaust stack was always slightly below ambient.

4.3 Acoustic Characterization

The bead layer, honeycomb, and bottom cavity of the burner pictured in figure 4.2 were chosen to make the air flow uniform as it exits the burner body. However, the acoustic reflection coefficient represented by the burner is not obvious. Without knowing the acoustic reflection coefficient, it is impossible to calculate the standing wave pattern in the flame zone. For this reason, acoustic tests were conducted to quantify the standing wave field in the exhaust stack. These tests were performed with no flow or flame. The flow velocities are quite small and do not cause substantial perturbations to the burner or the acoustic field, so neglecting flow in the exhaust stack is a reasonable simplification. However, the perturbation to the acoustic field by the flame may be more substantial. Generally, the acoustic field in a combustion apparatus can be perturbed substantially by changes in sound speed attributable to both temperature and molecular weight variations. In this case, the flame is highly overventilated, and so the regions where the temperature departs substantially from ambient are quite small. In particular, the luminous length of the flame is small compared to the wavelength of the sound in most cases. Any perturbation to the acoustic field caused by the flame will be localized to the small region in and immediately around the flame. The acoustic field for the low temperature conditions should help in understanding the large features of the flame, even if the detailed field will change due to the temperature gradients.

The standing wave pressure field was measured using the probe tube method (Blackstock, 2000). The fuel tube and bottom plate were removed from the burner, and replaced with a straight tube through the center of the burner and a plate with a hole in the center. This allowed a steel probe tube to be inserted into the flame zone and stack from beneath the burner. A Brüel and Kjær 1/8" microphone was placed in the bottom end of the probe tube, so that the steel tube acts as a waveguide, carrying the signal from the open end in the stack to the microphone at the bottom. The microphone is accurate to ±2 dB. The microphone/probe tube combination was calibrated as a function of frequency, using the microphone alone as the calibration standard. The calibration curve is shown in figure 4.3. The probe tube measurement is discussed further in ASTM standard C384-98 (ASTM, 1998).

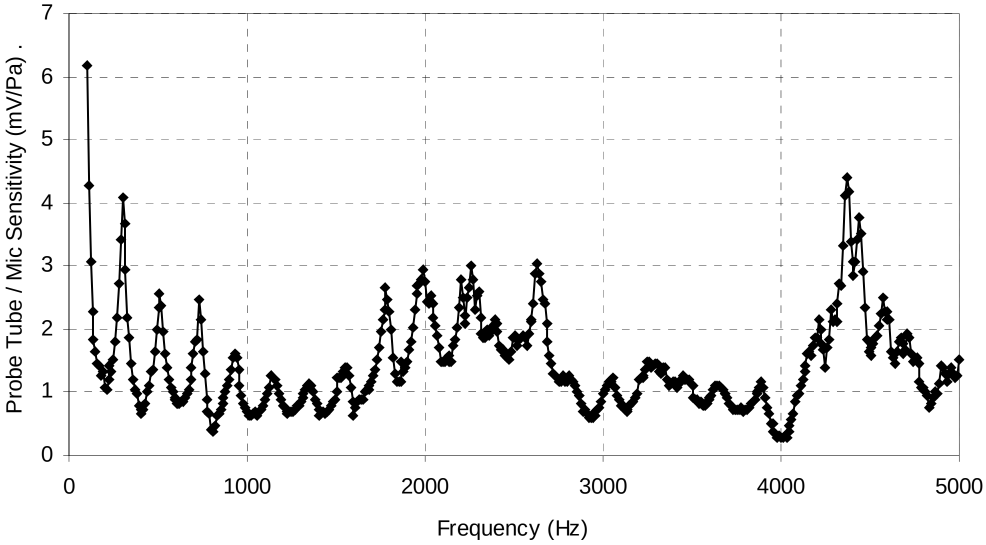

Figure 4.3. Small signal calibration curve for probe tube.

Using the standing wave ratio, which is the ratio of the maximum and minimum harmonic pressure amplitudes, the location of the first pressure minimum or maximum above the burner, the acoustical reflection coefficient R_{ac} of the burner can be calculated, as described by Blackstock. (Blackstock, 2000). Note that R_{ac} is a complex quantity that can be represented as a phasor of magnitude 0 to 1 and rotation angle 0 to 2π. Once the reflection coefficient is known, the amplitude of the pressure signal for the forward traveling component of the standing wave, P^+, can be calculated using:

$$P = P^+(e^{jkz} + R_{ac}e^{-jkz})$$

where P is a measured pressure amplitude and z is the height above the burner for that measurement. In practice this was done at the location of the maximum pressure amplitude. Knowing R_{ac} and P^+, the acoustic particle velocity U_{ac} at all points in the tube can be calculated using:

$$U_{ac} = (P^{+}/Z_{0})\,(e^{jkz} - R_{ac}e^{-jkz})$$

Figure 4.4 shows the pressure and velocity standing wave fields at 230, 500, 940, and 3100 Hz. At each frequency, powers of 0.1, 1, and 10 W are shown. Note that the values of power reported in this work denote the electrical power to the speaker, which is much more easily measured than the acoustic power radiating from the speaker. On each graph, the pressure trace is shown as a solid line, while the velocity trace is shown as a dotted line. One key point to note from these charts is that the pressure and velocity generally scale very closely with the square root of the electrical power to the speaker, W. This signifies that the effect of nonlinear distortions in the system are small. The exception to this is at 230 Hz, which is below the lowest nominal operating frequency of the speaker. At this frequency, there seems to be some harmonic vibration which causes the pressure and velocity to increase slightly faster than $W^{0.5}$ between 1 and 10 W.

In the next chapter, the calculated particle velocities U_{ac} will be compared to velocities measured in the flame.

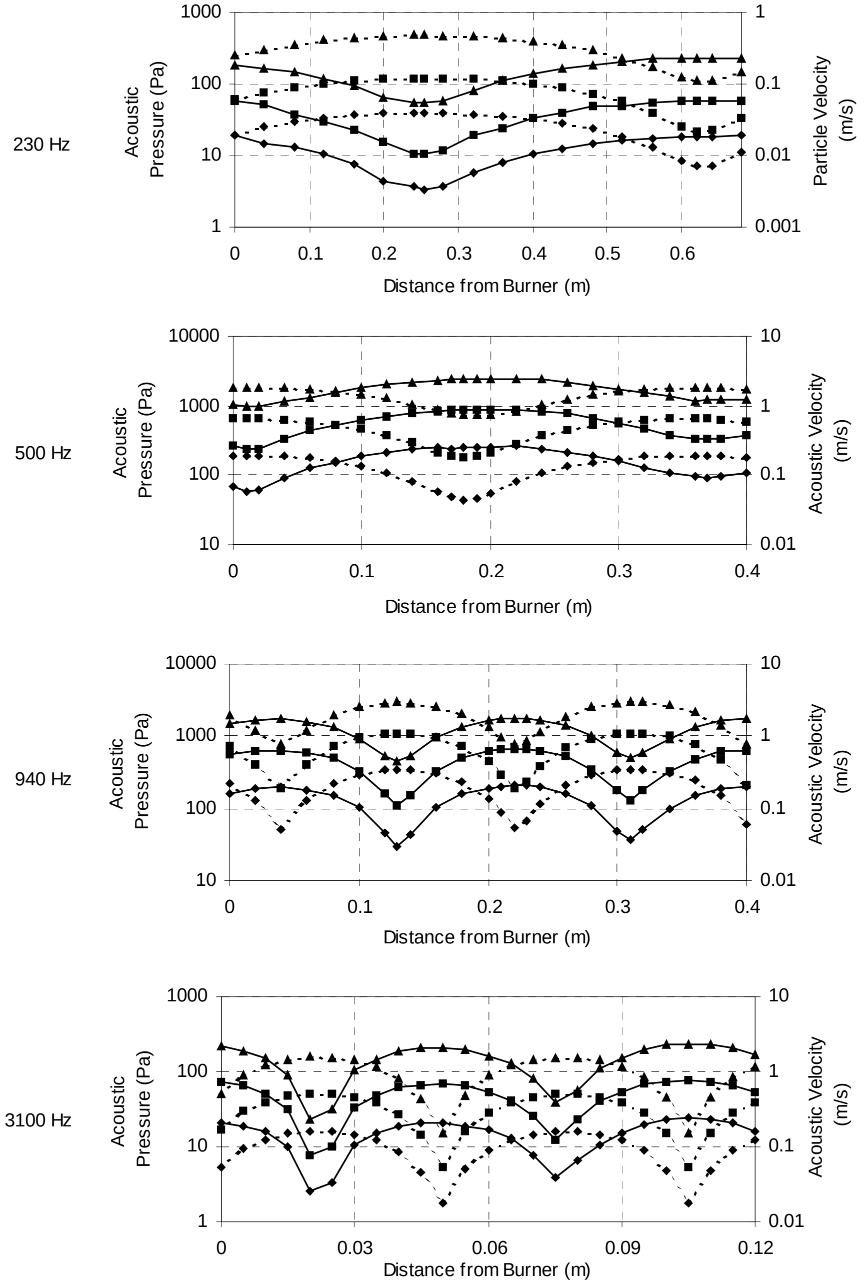

Figure 4.4. Standing wave patterns in the stack at various frequencies

Power Levels: ♦: 0.1 W. ■: 1 W. ▲: 10 W

solid lines are pressure, dashed lines are particle velocity

Some attempt was made to model the acoustical impedance of the burner body. Acoustically, the burner may be represented by three distinct impedances, Z_1, Z_2, and Z_3. Z_1 is the air above the burner surface, whose impedance is simply ρc. ρ is the density of the air and c is the adiabatic sound speed, 1.21 kg/m^3 and 343 m/s respectively at STP, giving Z_1 = 415 rayls. Z_3 is the impedance of the rigidly terminated cavity below the bead layer. This impedance is given by Blackstock (2000):

$$Z_3 = -j\rho c \cot(kh) \qquad \text{Eq. 4.1}$$

k is the wavenumber, defined just as in optics as $\omega/c = 2\pi/\lambda$, but using the speed of sound rather than light. h is the length of the rigidly terminated cavity, 10.2 cm (4.0 in), which is the distance from the bottom of the bead layer to the burner base plate, including both the honeycomb and the plenum below it.

The impedance of a porous layer is discussed by Morse (1948) and Morse and Ingard (1968). They present a phenomenological model of the impedance of the bead layer that involves three parameters. The first is r_p, the pressure drop through the porous layer per unit length of porous media per unit velocity of flow through the layer. This accounts for the viscous dissipation of sound in the narrow channels of the porous bed. The velocity for this is the average velocity, i.e. the volume flow through the porous bed divided by the cross sectional area of the bed. This quantity was measured by putting a pressure tap on the burner body and measuring the pressure drop across the bead bed due to a steady flow of air out of the bed and into open air. r_p is 3.6 kPa/m^2 s. The second parameter p_p is the void fraction of the bed (one minus the volume fraction of beads). This is the fraction of the volume of the bed that is taken up by the beads. The volume of the cylindrical bed was calculated, and the volume of the beads was measured by immersing them in water, giving p_p of 0.43. The final parameter m_p accounts for the mass of the porous bed that moves with the flow of fluid through it. This parameter accounts for light fibrous matter that could be in a bed flapping back and forth with the oscillating acoustic flow. Because the bead bed is composed only of dense glass spheres, it was assumed that there was no flapping occurring, which produces a value of 1 for m_p. Given these parameters, Morse expresses the impedance of the bead bed as:

$$Z_2 = \rho c \sqrt{\frac{m_p + j\dfrac{r_p}{\rho\omega}}{\gamma p_p}} \tag*{Eq. 4.2}$$

The wave number for flow through the porous bed k_2 also changes, and is given by:

$$k_2 = \frac{\omega}{c}\sqrt{\left(m_p + j\frac{r_p}{\rho\omega}\right)\gamma p_p} \tag*{Eq. 4.3}$$

Blackstock gives the formula for the reflection coefficient R_{ac} of a surface which is a composite of two impedances Z_2 and Z_3 facing a medium with impedance Z_1:

$$R_{ac} = \frac{\left(1-\dfrac{Z_1}{Z_3}\right)\cos(k_2 d) + j\left(\dfrac{Z_2}{Z_3}-\dfrac{Z_1}{Z_2}\right)\sin(k_2 d)}{\left(1+\dfrac{Z_1}{Z_3}\right)\cos(k_2 d) + j\left(\dfrac{Z_2}{Z_3}+\dfrac{Z_1}{Z_2}\right)\sin(k_2 d)} \tag*{Eq. 4.4}$$

d is the thickness of bead layer, medium 2.

The reflection coefficient was measured using the probe tube method for a few frequencies. In addition to the standing wave patterns shown in figure 4.4, data was taken at 800, 900, 1000, 1100, and 1200 Hz. The full set of data is compared to the model in figures 4.5 and 4.6. The figures show that the magnitude of the measured reflection coefficient matches only somewhat to the model, but the model and data agree fairly well about the phase of the reflection coefficient. In the end, the data taken was sufficient for the purposes of this study, and the model was not refined further.

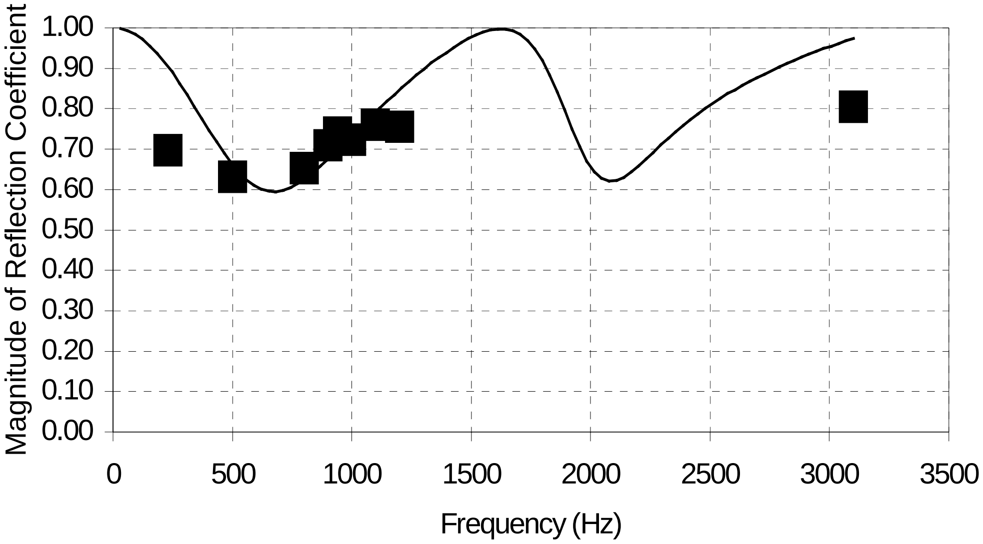

Figure 4.5. Comparison of model and data for the magnitude of the acoustic reflection coefficient of the burner.

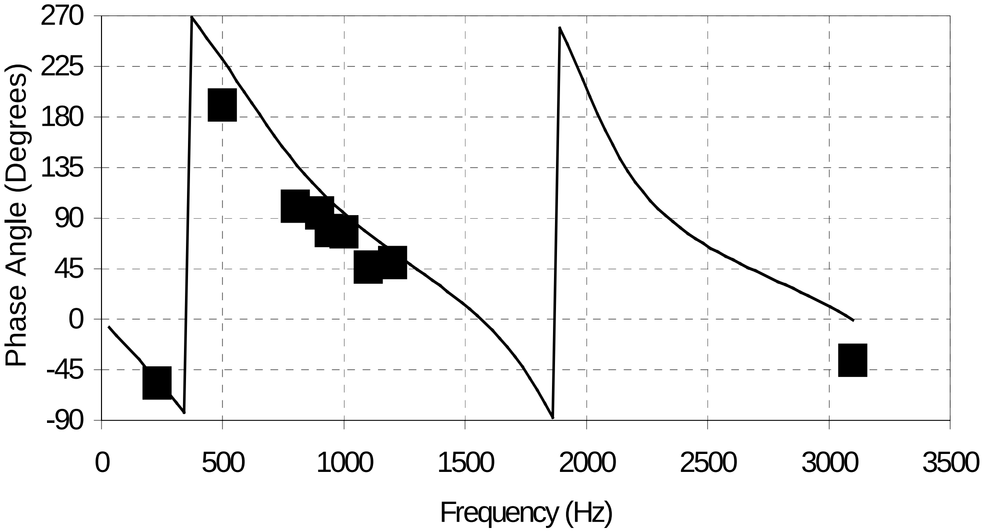
270
225
180
135
90
45
0
-45
-90
Phase Angle (Degrees)
0
500
1000
1500
2000
2500
3000
3500
Frequency (Hz)

5 ACOUSTIC CHANGES TO FLAME SHAPE

High-speed movies of the natural flame luminosity under acoustic excitation were taken using a Red Lake Imaging HR2000 camera. This camera is capable of capturing 2000 frames per second, at shutter speeds up to 1/40,000 of a second. It puts out analog video signals in NTSC format, which can be recorded on VHS tapes and captured by a personal computer using video frame grabbing equipment. At 230 and 500 Hz, the frame rate is sufficient to capture the flame behavior in some detail. 940 Hz is the frequency which elicits perhaps the greatest response from the flame, but 940 Hz is very near the Nyquist frequency for the camera, meaning that the camera is of value only for instantaneous photos, not movie analysis. The flame excited at 3100 Hz displays interesting low frequency behaviors that can be captured effectively.

5.1 Flame Shapes

The major features of the flame shapes captured with the camera generally appear quite repeatable from cycle to cycle. In order to facilitate examination of the flame shapes, an edge detection algorithm was applied to the pictures of the flame. Pictures of the flame before and after edge detection are shown in figure 5.1. The scale in these photos was taken from a picture of a ruler placed where the flame would be. It is accurate to within ±0.3 mm as pictured here, but it is repeatable to within ±0.1 mm. An error in the transfer of the scale from the movie file to analysis software will be reflected in the measurements as a bias rather than a random error. Note that the bits of the flame which are weakly luminous will not be captured as strongly in the high-speed photographs, or by the edge detection algorithm, as the brighter sections. This could have an effect, particularly in those cases where the flame divides into large luminous sections separated by thin luminous strands. To avoid this, the aperture setting on the digital camera was adjusted to give maximum flame detail. Overexposure of the areas where the flame was brightly luminous was not a significant concern compared to capturing the weakly luminous areas. During edge detection, no connecting sections were seen to disappear.

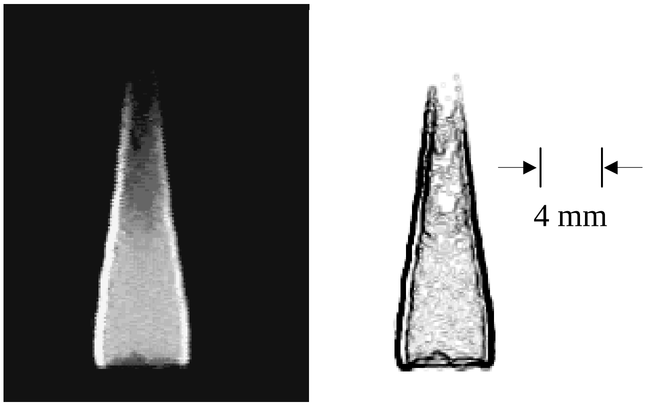

Figure 5.1. Flame with no acoustic driving, before and after edge detection.

The flame shape changes substantially under acoustic forcing. Figure 5.2 shows various pictures of the flame excited at 940 Hz. Recall that the fuel and air flow rates are constant for all flames throughout this study. The only variable changing in this series of pictures is the amount of power applied to the speaker (which in turn changes the acoustic velocity as discussed shown in chapter 4). Note first that, in the 0 W and 2.0 W cases, the flames do not close off at the top, and a smoke trail of unoxidized soot escapes the flame. At the base of the 2.0 W and especially 5.0 W flames there are visible periodic wrinkles, which will be discussed later. Up to 5.0 W, the flame height increases, but above 5.0 W the flame height decreases again.

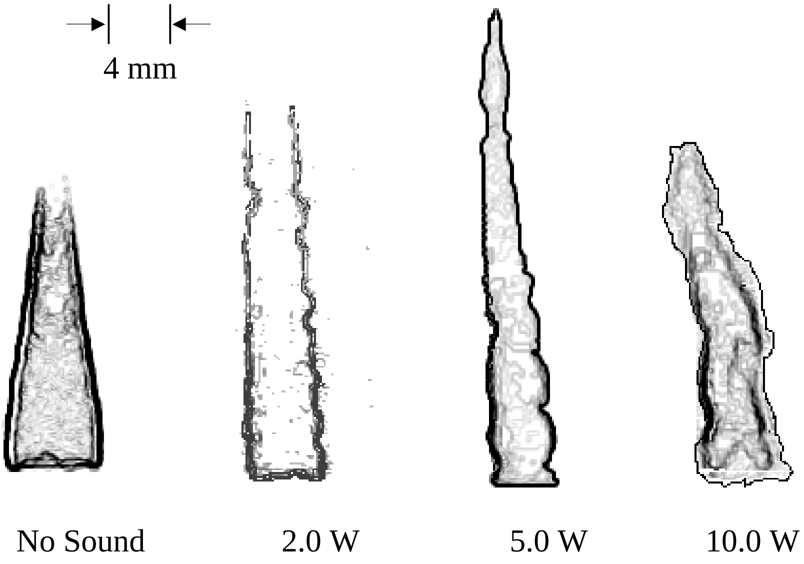

Figure 5.2. High-speed photos of flame excited at 940 Hz.

Pictures of the flame excited at 230 Hz are shown in figure 5.3. There are several striking features to this series of pictures. Most significantly, the periodic wrinkles seen in the 940 Hz flame have become quite pronounced, and at high powers the wrinkles even pinch together, so that the flame divides into separate luminous slugs. It is presumable that the slugs are actually reacting, as they appear to burn up and shrink as they ascend. The height of the flame also increases with power.

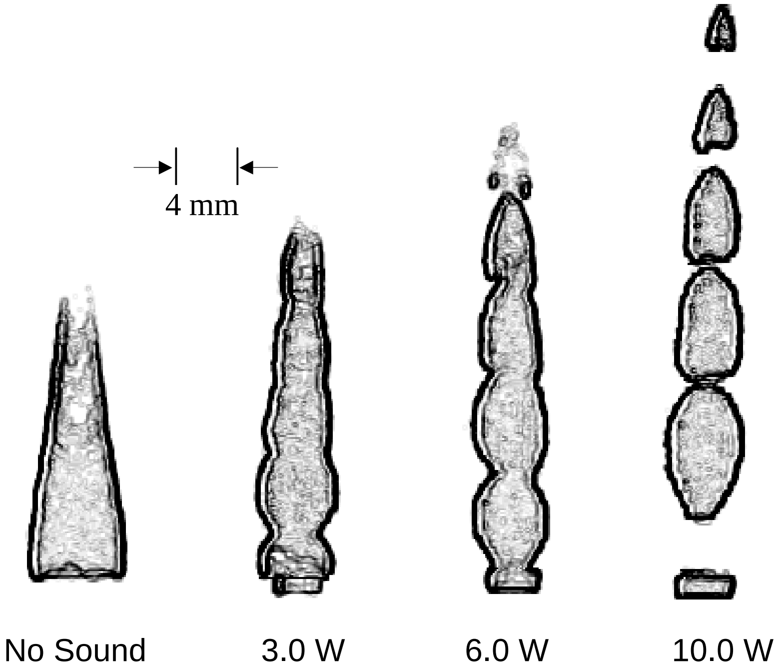

Figure 5.3. High-speed photos of flame excited at 230 Hz.

Figure 5.4 shows the flame under 500 Hz forcing. This flame has very well defined pulses at lower powers, but it tends to deform and collapse at higher powers. The reasons for this will be discussed later. At 500 Hz, the flame tends to deposit large amounts of soot on the fuel nozzle. This soot cake quickly becomes quite large, changing both the shape and the emissions characteristics of the flame. For this reason, it was not possible to repeatably measure emissions from the 500 Hz flame.

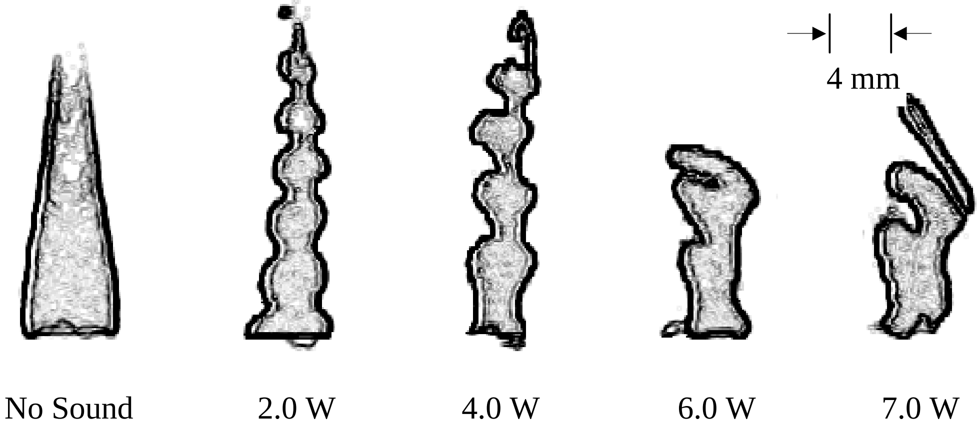

Figure 5.4. High-speed photos of flame excited at 500 Hz.

The changes in flame geometry under acoustic forcing are quantified in figure 5.5, which shows the flame height and average radius as a function of sound power at both 230 and 940 Hz. These numbers are the average of measurements made on scaled photographs such as those shown above. The average radius of the flame is defined as the total (projected) area of the flame in the photograph divided by the flame height, divided by two. As discussed above, the individual measurements are accurate to the nearest 0.5 mm and precise to the nearest 0.1 mm. The measurements are repeatable to within 0.5 mm. The flame height increases to a maximum of twice its unforced value, and the radius shrinks by approximately 20%.

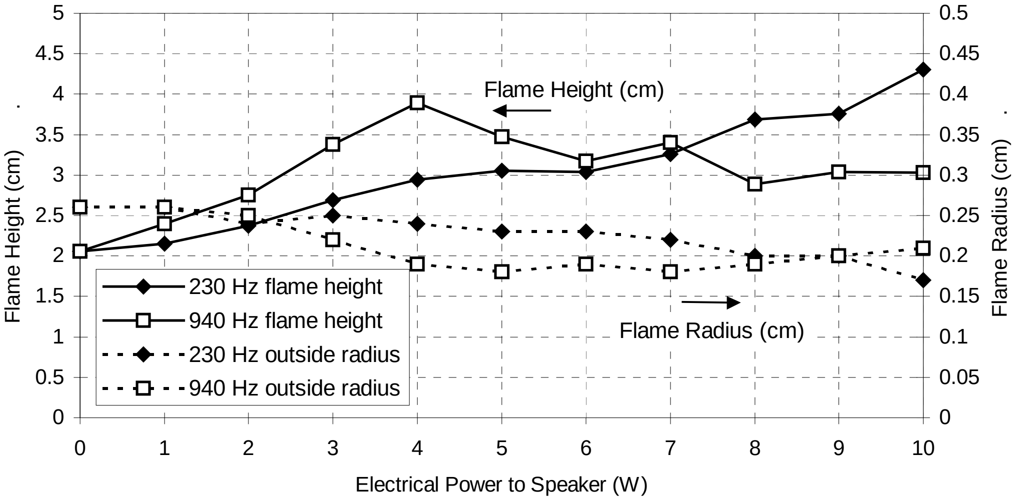

Figure 5.5. Changes in flame height and average radius with sound power for flames excited at 230 and 940 Hz.

5.2 Pulsation Spacing Analysis

In order to draw some further insight into the mechanisms driving the flame pulsation and corresponding soot modifications, the spacing of the flame wrinkles or pulses at 230, 500, and 940 Hz is examined.

In characterizing the pulsation spacing, the first step was to measure the pulse length as a function of frequency and power. In order to measure the pulse length, a clearly identifiable point that repeats on each pulsation must be identified. This point is the narrowest spot on each pulse, or the halfway point between discrete slugs in the 230 Hz high power cases. Figure 5.6 shows the average wrinkle spacing for the 230, 500, and 940 Hz cases as a function of power. The confidence bound lines were omitted on this chart for ease of reading, but the 90% confidence bounds average ±25%. The scatter in the data is partly because the spacing decreases weakly with increasing distance from the fuel nozzle, and that effect has been averaged out here.

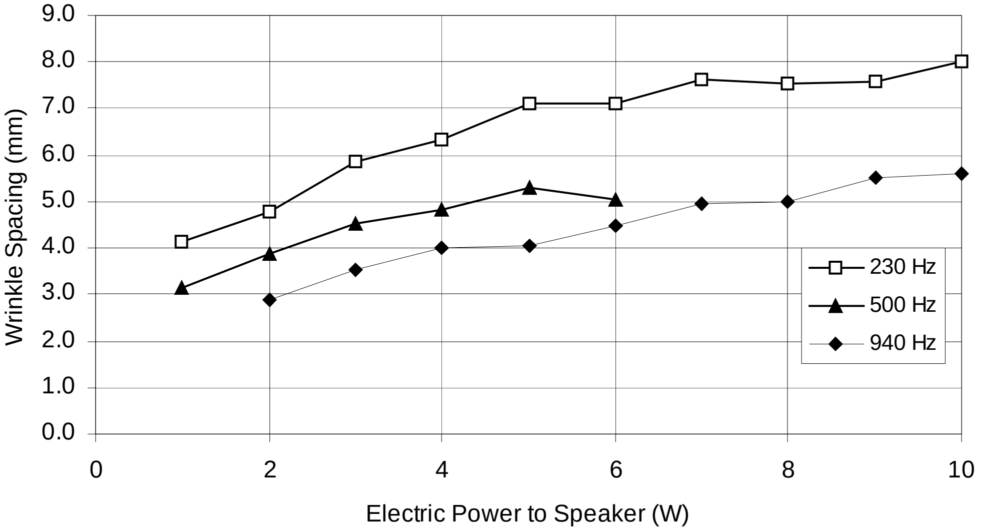

Figure 5.6. Average wrinkle spacing versus power for 230, 500, and 940 Hz driving.

In order to determine the dependence of the pulsation spacing on frequency and intensity, a basic analysis of the velocities in the problem was used. The frequency with which a pulse passes a point in space is equal to the acoustic driving frequency, f. The total velocity with which the pulses travel upward, U_{tot}, is then Lf. Figure 5.7 shows U_{tot} for the powers and frequencies in this study. U_{tot} increases with power for each frequency tested. Note that the maximum value of U_{tot} found was approximately 4.5 m/s, a factor of 45 times larger than the cold flow velocity, 0.1 m/s. This large imposed velocity explains the elongation of the flame observed in figures 5.2 through 5.4. The fact that the flame does not elongate by a factor of 45, and in the 940 Hz case even shortens, calls to mind the well-known result of Hawthorne *et al.* (1949). They found that flame height is directly proportional to jet velocity for laminar jet flames, while it is independent of jet velocity for turbulent jet flames. Both of these effects are driven by the fact that the mixing rate determines the overall rate of reaction for a diffusion flame (Glassman, 1996). The mixing rate in a laminar flame is determined by molecular diffusion rates. A higher velocity exit jet will travel farther before diffusion brings oxygen all the way to its core, allowing the last of the fuel to react. However, once a jet becomes turbulent, turbulent diffusion becomes the dominant mixing mechanism. The turbulence becomes more intense as the jet velocity increases, canceling the elongating effects of increased velocity. In this case, at a velocity of 4.5 m/s, the Reynolds number of the jet is 2000, which would only be transitionally turbulent. However, the fact that the flame height is not directly proportional to velocity implies that there is some other mechanism causing mixing beyond simple molecular diffusion. The mechanism will be discussed in chapter 9.

U_{tot} must equal the fuel jet velocity U_{jet} plus a steady velocity driven by the acoustics, U_{dc}. U_{jet} is approximated by the cold flow jet velocity, 0.10 m/s, multiplied by the ratio of the flame temperature (measured roughly at 1800 K) and room temperature, 298 K. This gives a value for U_{jet} of 0.60 m/s. Solving for U_{dc}:

$$U_{tot} = U_{dc} + U_{jet} = Lf \qquad \text{eq. 5.1}$$

$$U_{dc} = Lf - U_{jet} \qquad \text{eq. 5.2}$$

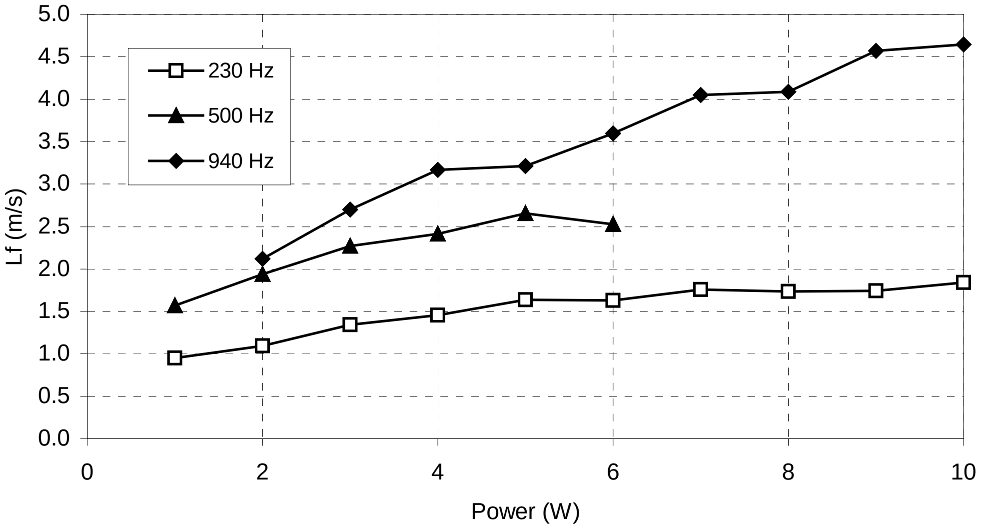

Figure 5.7. Total velocity (*Lf*) versus power and frequency.

Equation 5.2 permits discernment of the appropriate scaling of U_{dc}. Figure 5.8 shows a graph of U_{dc} divided by the oscillating acoustic velocity, U_{ac}. Scaling U_{dc} by U_{ac} removes the dependence of U_{dc} on power at 500 and 940 Hz, showing that this is the appropriate scaling. The fact that the 230 Hz line does not collapse as well is attributed to the nonlinearities in the system at 230 Hz (i.e. U_{ac} does not scale as $W^{0.5}$, as discussed in chapter 4). The finding that the DC and AC velocities are proportional and of comparable magnitude suggest that the flow is a manifestation of the synthetic jet phenomenon, which will be discussed at some length in chapter 9.

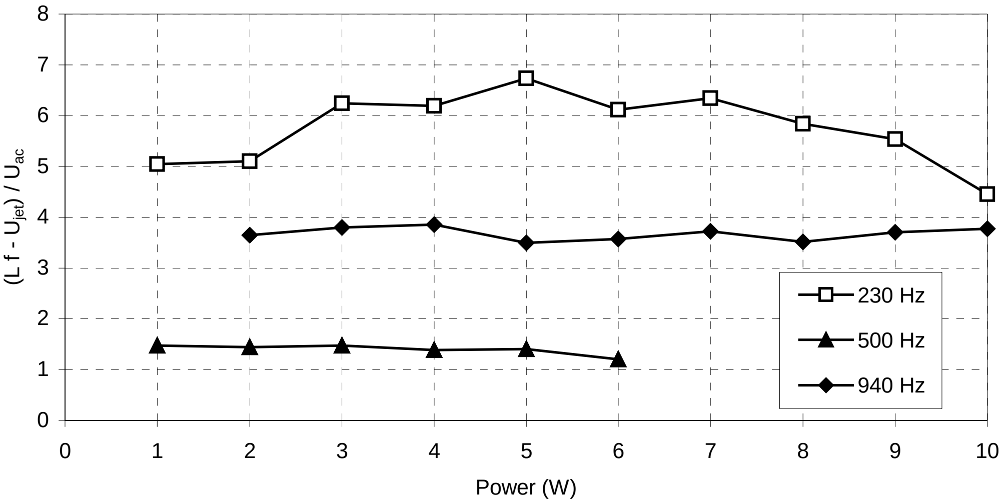

Figure 5.8. U_{dc} scales as U_{ac}.

Figure 5.8 also shows that U_{dc} *is* a non-monotonic function of frequency. The value of U_{dc}/U_{ac} at 500 Hz averages 1.39, while at 230 Hz the average is 5.76 and at 940 Hz it is 3.67. The height of the 230 and 940 Hz flames increases significantly from the unforced case. The 940 Hz case does shorten again at the highest powers, while the 500 Hz flames do not substantially elongate.

5.3 3100 Hz Sound

3100 Hz is an interesting case because of the odd flame shape created by this frequency of excitation. Figure 5.9 shows a side view of the flame, and figure 5.10 shows a view from above. The flame is very flat, and spreads out radially in the shape of a bowl.

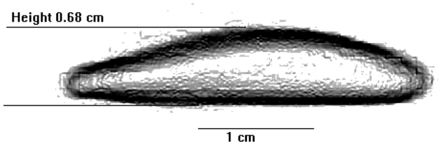

Figure 5.9. Side view of a flame excited at 3100 Hz, 7.5 W

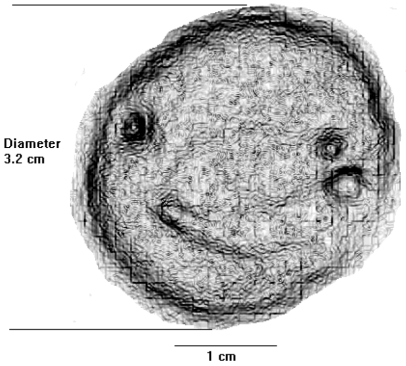

Figure 5.10. Top view of the flame excited at 3100 Hz, 7.5 W.

Most of the soot emitted by this flame leaves the flame at its edges, travels up along the sides of the glass viewing cylinder, circulates into the center of the flame zone, and then moves back down toward the flame. Some of the particles re-entering the flame even become hot enough to incandesce. These particles will convect back out toward the edges of the flame, and can circulate repeatedly until they finally break out of the recirculation zone and ascend the exhaust stack. A schematic of the flow pattern is shown in figure 5.11.

The behavior of the 3100 Hz flame varies substantially at different power levels. At low powers, below about 1 W, the flame looks very much like the unforced flame of figure 5.1. From 1 watt to 4 watts, the flame shape becomes unsteady, oscillating between the unforced shape and the open, bowl shape. The oscillations are regular, making the flame look like it is flapping at a frequency around 1 hertz. Above 4 watts, the flame shape becomes steady in the open, bowl shape.

The behavior of the flame under 3100 Hz forcing seems to indicate that the 3100 Hz sound produces a steady downflow in the center of the flame. At low powers, the downflow is insufficient to counter the effects of buoyancy on the soot and hot gases, and the flame shape is not changed from the unforced flame. At medium powers, the force from the downflow is comparable to buoyancy, and the flame takes on an unstable oscillating balance. At high powers, the downflow dominates buoyancy, driving the soot to the edges. This circulating flow behavior is attributed to Rayleigh streaming, which is the production of time-constant flow in a channel where a standing wave field exists by the action of viscous attenuation along the walls of the channel. Further discussion of this phenomenon is in chapter 9.

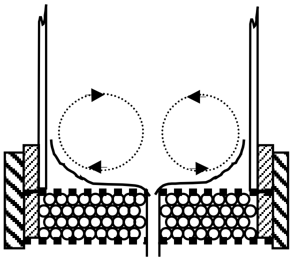

Figure 5.11. Schematic of particle paths in the flame excited at 3100 Hz.

6 GLOBAL POLLUTANT EMISSIONS

This chapter will detail measurements of some of the pollutant outputs of the flame. These include soot particles, which are measured both by an aerodynamic particle sizer and by an optical extinction measurement, as well as the gaseous pollutants carbon monoxide, nitric oxides, and unburnt hydrocarbons.

6.1 Global soot particle measurements by aerodynamic particle sizer

Particulate concentrations and size distributions in the exhaust stream are measured with a TSI model 3320 aerodynamic particle sizer (APS). The APS determines particle size by passing particles in an accelerating air stream through a detection volume where they pass through two closely-spaced laser beams. The particles scatter the light from the laser beams, and some of the scattered light falls on an avalanche photodiode. Larger particles have more inertia, which causes them to be only partially entrained in the accelerating gas flow. They move more slowly through the detection volume, generating a signal of longer duration. In addition, larger particles scatter more light than smaller particles. The strength and duration of the signal from the avalanche photodiode is correlated electronically to determine the size of the particle that scattered the light. The device categorizes the particle in one of 52 channels, distributed logarithmically from 0.5 μm to 20 μm, to produce size distributions based on count. It also measures particles from 0.2 to 0.5 μm with a light scattering measurement and reports those in the size bin at 0.3 μm. (Note that this size range is larger than the ideal, but not so large that it is not useful for a heavily sooting fuel like acetylene. No counter was available in a smaller size range.) The particle counts are uploaded in real time to a personal computer running TSI's proprietary interface software, from which they can be exported to other programs for further analysis.

The APS has a maximum inlet particle concentration of 1000 cm^{-3}. For the high particle counts generated by the base flame, a TSI model 3302A diluter is necessary in order to not saturate the detector. The diluter works by positioning a small diameter capillary tube in the center of the sample stream traveling through a larger diameter tube. The particle laden gases which enter the tube are passed undisturbed to the detector. However, the gases which do not enter the tube are diverted through a HEPA filter before being reinjected into the sample flow. The filtered and unfiltered streams are passed through a mixing cone and then drawn into the APS. Different diameter sampling tubes can be used to produce different dilution ratios. The diluter comes equipped with two capillary tubes, a 20:1 tube with an inlet diameter of 1.4 mm, and a 100:1 tube with an inlet diameter of 0.9 mm (TSI, 1997). The 20:1 tube is generally used in this study, as it dilutes the sample sufficiently to avoid saturating the detector under high soot conditions, but provides as much sample as possible to the detector under less sooting conditions. Switching dilution capillaries during the run is not advisable for two reasons. Operationally, it is a time-consuming process. Also, any uncertainty in the behavior of the diluter will be an error in comparisons of data based on different dilution ratios (or no dilution at all). Using the same diluter allows comparisons to be made directly without adding error to the measurement. The efficiency with which the diluters pass various size particles is measured at the factory and programmed into the interface software, so that the software will automatically compensate for the diluter.

The particle counter is factory calibrated, and the manufacturer recommends recalibration using a suitable standard after 5000 hours of operation. The accuracy of the overall concentration measurement is ±10%. Using the 20:1 capillary on the system, the concentration measurement is then accurate to ±2000 particles / cm^3. Without dilution, the accuracy of the particle counter system is ±100 particles / cm^3. (TSI, 1997)

The particle sizes returned by the APS are aerodynamic diameters, D_{ae}, a length scale discussed in detail in chapter 2. Combining equations 2.9 and 2.17 gives the relation between the aerodynamic and geometric diameters:

$$D_{ge} = 2D_{ae}^{\frac{2}{D_f-1}} \sqrt{\frac{3}{2}\frac{D_f+2}{D_f}} \left(\frac{2\rho_w}{k_f \rho_o \beta} d_0^{D_f-3} \right)^{\frac{1}{D_f-1}} \qquad \text{eq. 6.1}$$

This relation is plotted in figure 6.1. The geometric diameter is proportional to the aerodynamic diameter raised to the 2.8 power, which means that the geometric diameter rapidly becomes quite large. It is key to note that the value of D_f found by Köylü and Faeth (1994) is for aggregates with 1 to 200 primaries (38 nm < D_{ae} < 308 nm). The size range of the APS is larger than the range of their work. Recall that the 20:1 diluter tube has a diameter of 1.4 mm, which would correspond to an aerodynamic diameter of 4.3 μm. Clearly, there is a conflict. Palacios *et al.* (2001) have examined large aggregates from an acetylene flame. They have found fractal dimensions as large as 2.5 for soot particles with radii of gyration as large as 30 μm. However, they admit the uncertainties created by the projection of very large aggregates onto a two dimensional micrograph. Because it is generally unclear what structure correction is needed for aggregates across most of the range of the APS, no correction is applied here, and no attempt is made to relate the aerodynamic diameters to other equivalent lengths.

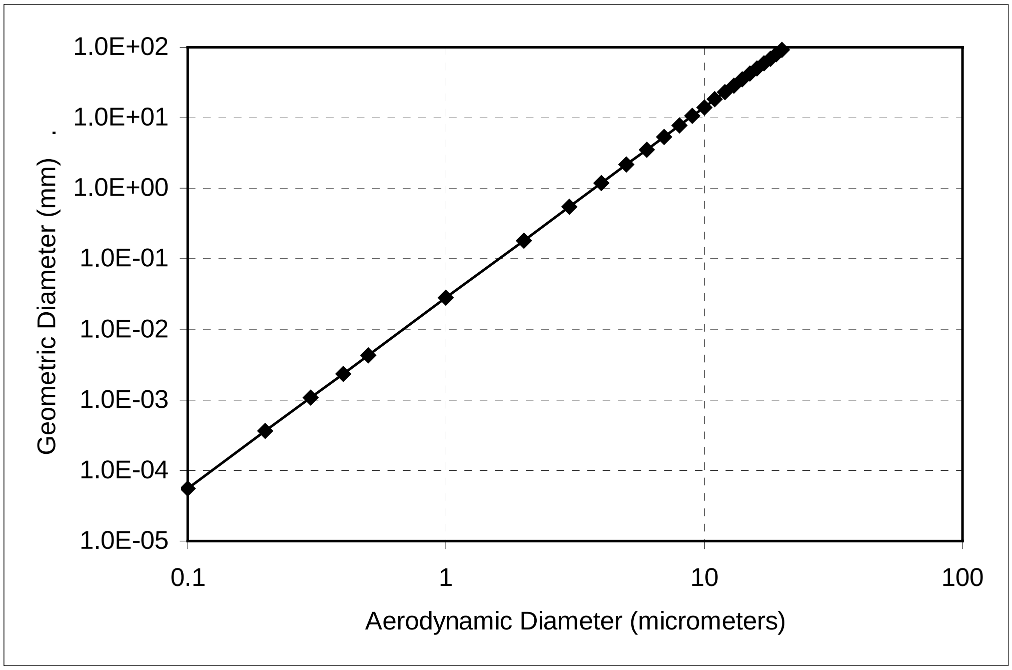

Figure 6.1. Theoretical relation of aerodynamic and geometric diameters.

APS data was taken as follows. The flame was lit, and the sound set to the desired frequency and power. The APS was then activated and allowed to run for a period of 60 seconds. It keeps counts of particles in each bin, and calculates statistics for particle diameters and concentrations at the end of the run. The test was repeated at least 3 times, more if the data exhibited significant scatter.

6.1.1 <u>940 Hz Sound</u>

Figure 6.2 shows the number concentration of soot particles released by the flame as it is irradiated by sound at a frequency of 940 Hz. The concentration initially increases as the sound power is increased from zero watts. At 1.0 W, the concentrations are approximately 3 times the no-sound rate. Equally striking behavior occurs between 3.5 and 6.0 W. The measured number concentration drops from 27,000 cm^{-3} at 3.5 W to 40 cm^{-3} at 6.0 W, a decrease of nearly 3 orders of magnitude. Above 6.0 W, the sooting characteristics do not change significantly.

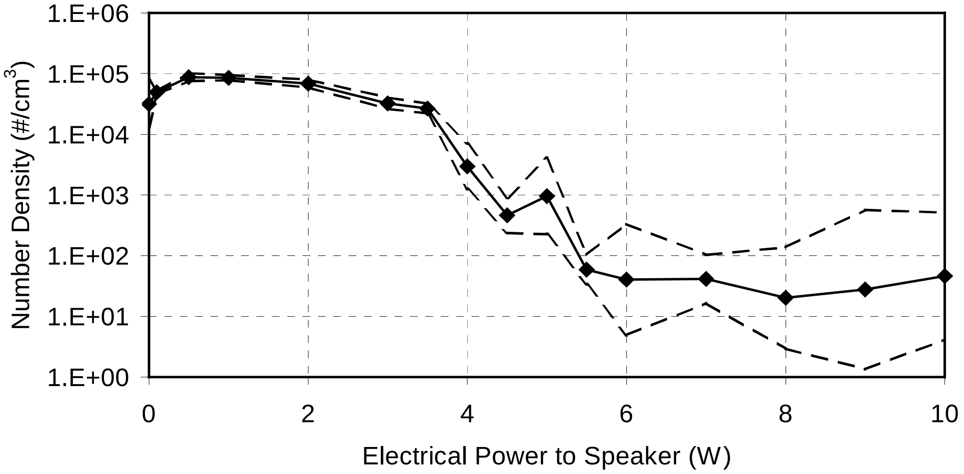

Figure 6.2. Number density of particles detected by the APS as a function of electrical power to speaker. Excitation frequency is 940 Hz. Dashed lines represent 90% confidence bounds.

Figure 6.3 shows the geometric mean aerodynamic diameter of the particles emitted from the flame. The acoustic driving has a limited effect on the mean particle size. From 0 W to 3.0 W, the particle aerodynamic diameter decreases by 15%. A decrease in soot particle diameter would be most likely caused by an increase in the rate of nucleation of soot particles, a decrease in the rate of soot agglomeration, or an increase in the oxidation rate. It is not clear which effect is occurring in this case, or precisely what here would be modifying any of the three processes. At high powers, there is an increase in the mean particle size, and a large increase in the scatter in particle sizing as evidenced by the dotted 90% confidence bounds.

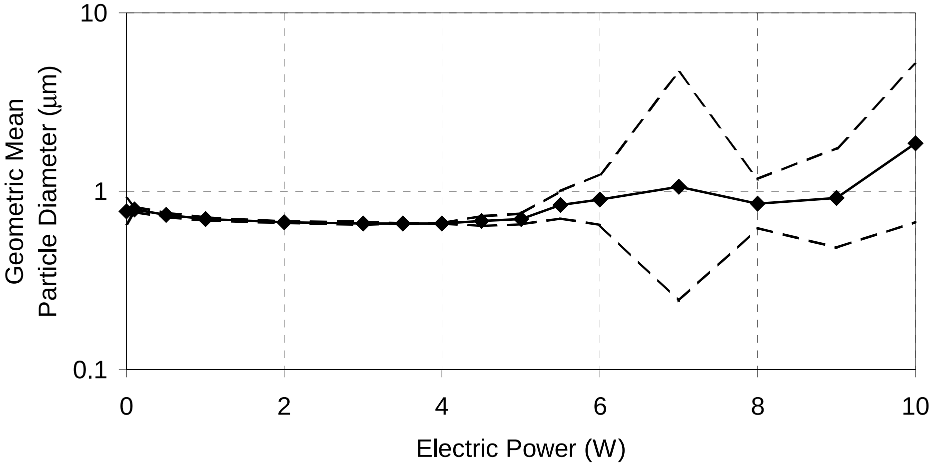

Figure 6.3. Particle aerodynamic diameter versus power for 940 Hz sound. 0 W is no sound case. Top and bottom lines are 90% confidence bounds

Figure 6.4 shows typical particle size distributions measured by the APS for 0, 0.5, and 5 watts, which are representative of the distributions seen in all cases and frequencies. The shape of the size distributions does not change substantially with power. The number density in each bin in the 0.5 W case is on average three times that of the no sound case. The 5 watt case averages one tenth the number density of the no sound case. In all cases, the smallest bin has by far the most particles in it, and so the change in that bin dominates the overall number density change. The fact that the particles tend to be in the smallest bins suggests the possibility that acoustic driving simply shifts the size distributions of the particles sizes that are too small for the APS to count.

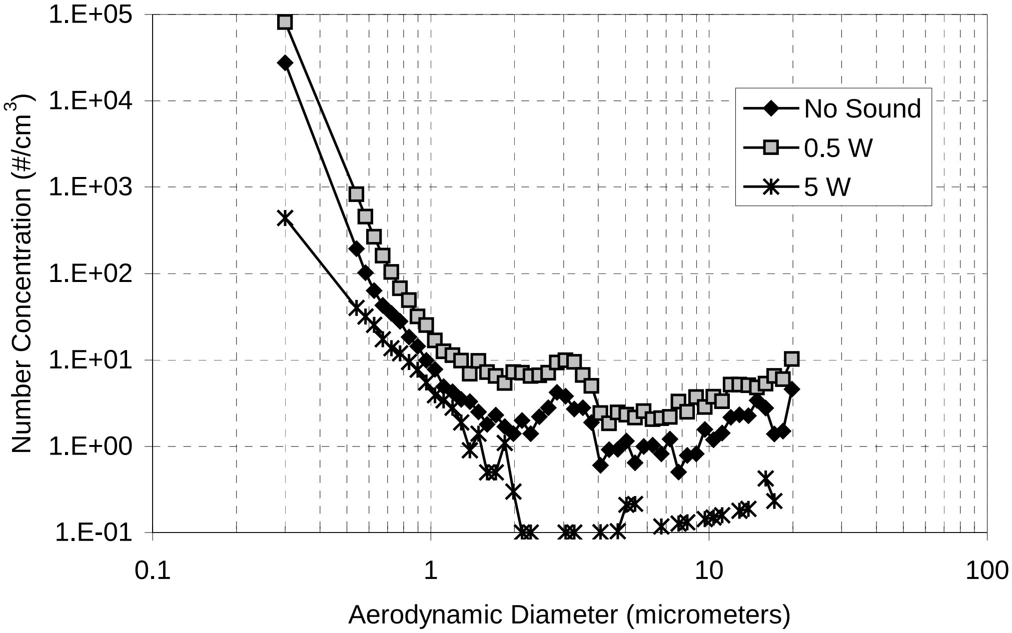

Figure 6.4. Particle size distributions under 940 Hz forcing as measured by the aerodynamic particle sizer. Blank spaces in 5 W curve denote bins where no particles were detected.

6.1.2 230 Hz Sound

As shown in figure 6.5, the soot production does not decrease as dramatically for the 230 Hz case as it did for the 940 Hz case. The particle number concentration and volume fraction both increase by a factor of 4 from 0 to 7 W, then decrease with increasing power. Figure 6.6 shows that the particle diameter decreases with increasing power across the 0 to 10 W power range, decreasing by 18% at 10 W versus the no sound case. This behavior is similar to the low power (0 - 3 W) regime of the 940 Hz case. Referring to figure 4.4, the amplitude of velocity variations is substantially lower at 230 Hz than at 940 Hz for the same electric power.

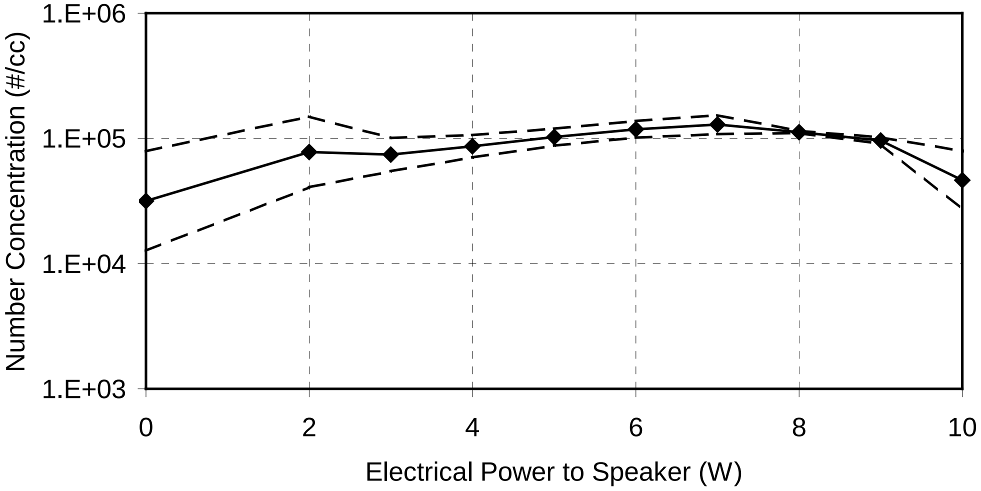

Figure 6.5. Number concentration of particles emitted from the acetylene flame excited at 230 Hz. 0 W is the no sound case. Top and bottom lines are 90% confidence bounds.

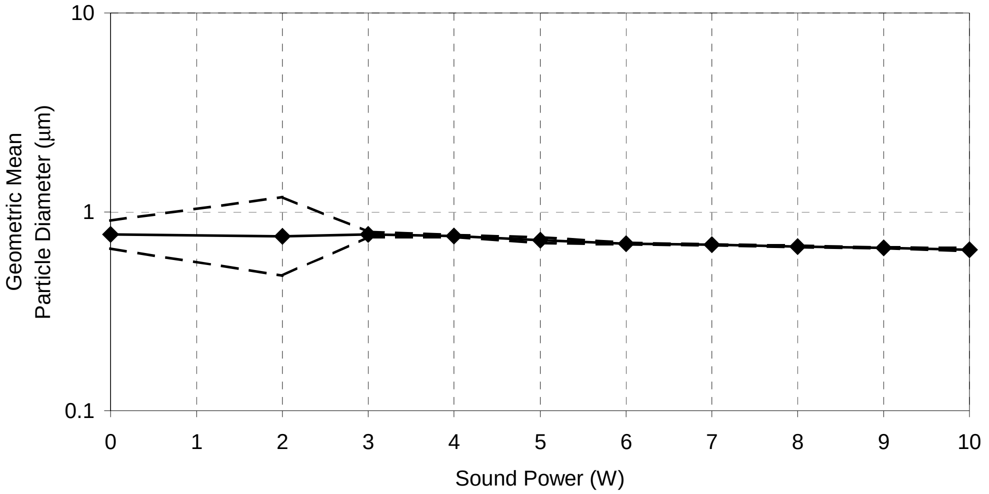

Figure 6.6. Particle aerodynamic diameter versus power for 230 Hz sound. 0 W is no sound case. Top and bottom lines are 90% confidence bounds.

Although it is not clear what specific system characteristics most modify soot emissions, the behavior of the flame is undoubtedly effected more by the acoustic velocity in the area of the flame than by the electrical power driving the speaker. Therefore, it is reasonable to seek a common driving parameter based on the velocity near the flame zone and the frequency of the acoustic driving, i.e. parameters which can be found at the flame. In investigating this, an acoustic Reynolds number was defined based on the acoustic velocity, U_{ac}, at the flame (2 cm above the burner) and the acoustic displacement, S_{ac}, which is in turn the acoustic velocity divided by the frequency, f. That is:

$$Re_{ac} = \frac{U_{ac} S_{ac}}{\nu} = \frac{U_{ac}{}^2}{f\nu} \qquad \text{eq. 6.2}$$

Note that, in linear acoustics, U_{ac}^2 is proportional to power, but the efficiency of the acoustic driver in this case changes with frequency, an effect not accounted for in basic linear theory.

Figure 6.7 shows the soot concentrations versus Re_{ac} for both the 230 and 940 Hz cases. Five points from the 940 Hz curve overlap the 230 Hz curve. The traces collapse, implying that this is an effective scaling. Over the range of Re_{ac} from 0 to 20, the soot emissions from the flame at both frequencies increases by a factor of 3 to 4 from the no sound case. The curve indicates that the 230 Hz excitation required more power than was used to achieve a reduction in soot, in part because the frequency was lower.

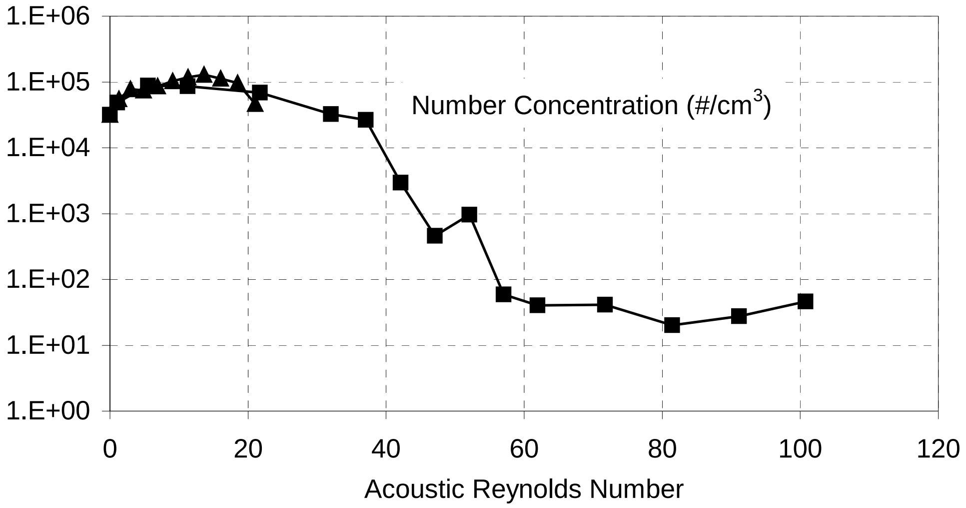

Figure 6.7. Soot number concentration at 230 and 940 Hz versus acoustic Reynolds number. ▲ = 230 Hz ■ = 940 Hz.

This curve seems to indicate that there may be some value to this scaling factor. However, it is important to note that the velocity magnitudes at the flame zone for the 500 and 940 Hz cases are comparable at constant power, yet only the

940 Hz case is effective for soot reduction. The 500 Hz case produces lots of soot deposition on the fuel nozzle. The deposited soot rapidly builds up to a level that it is changing the flame shape and interfering with the combustion. This clearly indicates that there is more to this question than simply the velocity and the frequency.

6.2 Global Soot Concentration by Laser Extinction

In order to corroborate the operation of the APS, a laser extinction measurement was performed in the exhaust stack near the APS sampling port, well above the flame. This was done to address two concerns. First, it was not certain that the distribution of soot across the exhaust stack was uniform or even consistent in all experimental situations. Second, the APS detects no particles with aerodynamic diameters smaller than 0.3 µm, which corresponds to roughly 150 primary spheres. Microscopy studies of soot routinely find smaller aggregates (Köylü and Faeth, 1994), so there is the concern that the APS will miss a significant population of particles.

The laser extinction measurement was done through a slot cut in the exhaust stack. The pressure in the stack is slightly below atmospheric, so soot escape from the slot was not a problem, and using an open slot rather than a window avoids the problem of dirty windows. A laser beam from an argon ion (488 nm) laser was split into a reference beam and a signal beam. The reference beam was aimed directly at a photodiode detector, measuring the reference intensity I_{ref}, while the signal beam was passed through the slot in the exhaust stack and then into a photodiode to measure the signal intensity I. The signal intensity was also measured with no flame burning, giving the baseline intensity

I_o. More details on the measurement setup are available in chapter 8. Using the Rayleigh-Gans optical model discussed in chapter 2, the volume fraction of the soot in the laser beam, f_v, can be calculated from the equation:

$$f_v = \frac{-\ln\left(\dfrac{I/I_{ref}}{I_o/I_{ref}}\right)\dfrac{\lambda}{S}}{6\pi(1+\rho_a)E(m)} \qquad \text{eq. 6.3}$$

Recall that:

λ is the wavelength of the laser (488 nm),

S is the path length of laser beam through exhaust stack,

$E(m)$ = Imag[$(m^2-1)/(m^2+2)$],

m is the index of refraction of soot, 1.57 + 0.56 j, and

ρ_a is the ratio of scattering cross section to absorption cross section.

As noted in section 2.3, as the number of primaries N in an aggregate becomes large, the value of N times the total scattering structure factor g becomes a constant. In this limit, both the scattering and absorption cross sections are proportional to N, so ρ_a becomes independent of N. In this limit, the expression for ρ_a is

$$\rho_a = \frac{2}{3}\frac{F(m)}{E(m)}\left(\frac{\pi d_0}{\lambda}\right)^{3-D_f} k_f \left(\frac{3D_f}{16}\right)^{\frac{D_f}{2}} \qquad \text{eq. 6.4}$$

where:

$F(m) = |(m^2-1)/(m^2+2)|^2$,

d_o is the diameter of the primary particle, 53 nm,

D_f is the fractal dimension of the aggregates, 1.74, and

k_f is the fractal prefactor, 8.1.

Note that the given inputs to eq. 6.4 lead to a value of 0.43 for ρ_a. This means that the Rayleigh Gans model will give volume fractions 43% lower than the most simple model, Rayleigh absorption (as shown by the $1+\rho_a$ factor in the denominator of eq. 6.3).

The path for the optical extinction measurement is a chord of the circular cross section of the exhaust stack. As such, the path length depends on the position of the extinction apparatus, according to the equation

$$S = 2\,(R_{stack}{}^2 - x^2)^{1/2} \qquad \text{eq. 6.5}$$

where R_{stack} is the inside radius of the exhaust stack, and x is the distance from the extinction path to the centerline of the stack. The average stack volume fraction at the elevation of measurement is then computed by an average of the individual path volume fractions:

$$\bar{f}_v = \frac{\int f_v(x)L(x)dx}{\int L(x)dx} \qquad \text{eq. 6.6}$$

Figure 6.8 shows the results of this measurement. The laser extinction measurement exhibits similar trends to the APS measurement, although the magnitudes of the changes are not as large. With no sound, the laser extinction measurement detects 6 ppb of soot. At 2 watts, the volume fraction increases to 12 ppb. At 10 watts, the laser apparatus detects only 0.3 ppb. The minimum volume fraction measured by laser extinction is 19 times less than the no-sound case.

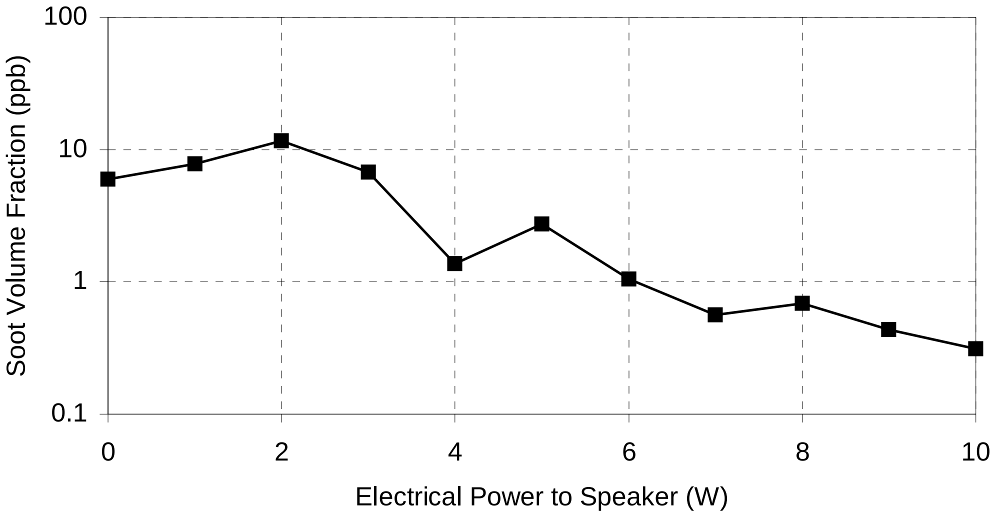

Figure 6.8. Soot volume fraction detected by the laser extinction apparatus versus electrical power to speaker. Frequency is 940 Hz.

The extinction apparatus was used to examine the distribution of soot across the exhaust stack. It had been assumed that the soot would be uniformly distributed across the stack. Figure 6.9 shows that this is not the case. The soot tends to be heavier around the outside of the stack. In spite of the nonuniformity, the general behavior shown in figures 6.5 and 6.8 continues to hold true - acoustic excitation at low powers increases the concentration of soot from the no-sound case, while increasing power drives the concentration of soot to near zero. This is true both at the stack centerline, where the APS sample is taken, and across the entire stack.

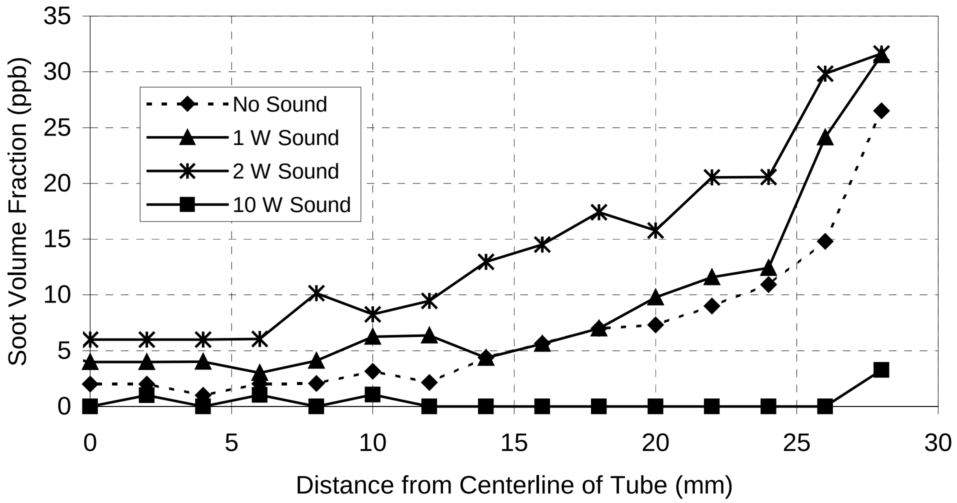

Figure 6.9. Distribution of soot across the stack.

6.3 Gaseous Pollutant Emissions

The emissions of gaseous pollutants from flames is currently the subject of at least as much interest as soot emissions, and often more. While acoustic forcing can be effective in terms of soot reduction, it is important to understand the effect of acoustics on the gaseous pollutant emitted from the flame.

The apparatus for gaseous emission tests samples from the same port as the APS. The sample flow is cooled, then split into three streams to go to the three gaseous pollutant analyzers. Each stream is filtered to remove particulate matter and metered. It then passes through the detector and out to the building exhaust.

6.3.1 Oxides of Nitrogen

Nitric Oxide and Nitrogen Dioxide (NO and NO_2, respectively, or NO_x collectively) are measured with a Rosemount Analytical model 951A chemiluminescent NO_x analyzer. This detector works through a series of nitrogen reactions. The entering sample may carry both NO and NO_2. The sample flows through a heated catalytic reactor that reduces the NO_2 to NO, giving a NO_x stream which is composed only of NO. At the same time, in a separate reactor, the oxygen in a stream of purified zero air is converted to ozone by exposure to ultraviolet radiation. The NO and O_3 are then combined in a reactor chamber, where they form NO_2 and O_2. Some of the NO_2 is in an excited state, but it immediately reverts to the ground state and releases a photon.

$$NO + O_3 \rightarrow NO_2^{*} + O_2$$

$$NO_2^{*} \rightarrow NO_2 + \text{photon}$$

When the temperature and pressure are constant and known, the fraction of NO_2 molecules that release a photon is known. The NO - O_3 reaction chamber is instrumented with a photomultiplier tube which detects the released photons and produces a voltage signal which is proportional to the mole fraction of NO and NO_2 in the sample.

The NOx analyzer measures the concentration of NO and NO_2 with a precision of 0.5% of full scale, and zero and span drifts of ±1% each in a 24 hour period. The device has 7 selectable full scale options from 10 ppm to 10,000 ppm. The calibration gases used for this instrument are zero air (0.1 ppm max NO) and 150 ppm (±3%) NO in N_2. Per the manufacturer's instructions, the device was calibrated once per 24 hour period. Based on using the 250 ppm full scale setting, the overall NOx detection accuracy is ±11 ppm. If necessary, calibration with a lower-concentration span gas can be done, giving an accuracy as good as ±0.5 ppm using the 10 ppm full scale and appropriate 1% accuracy span gas. (Rosemount Analytical Inc., 1997)

Figure 6.10 shows the NO_x emissions from the flame, normalized by the no-sound emissions, under a wider range of acoustic conditions. Powers up to 20 watts and frequencies from 200 to 1200 Hz were tested. The NO_x emissions tend to increase over the range of powers tested, with the emissions from the 940 and 1000 Hz cases increasing by over 60%. It is significant to note that the NO_x emissions do decrease by about 10% from the no-sound case with 1 W forcing at some frequencies. However, the general trend is toward increasing NO_x emissions.

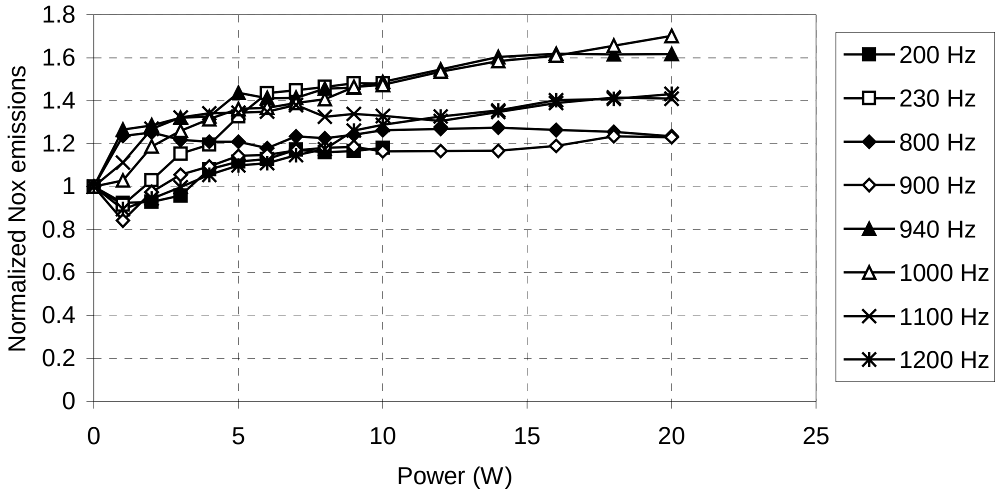

Figure 6.10. NO_x emissions versus power at various frequencies

This trend goes against the behavior that several other authors have found. Poppe *et al*. (1998) found that oscillating the velocity of a premixed methane-air flame reduces NOx emissions from the flame by up to 40% versus the steady case. Pont *et al*. (1998) drove a premixed propane-air flame in a dump combustor and found a reduction in NOx emissions of almost 60% from the steady result. McQuay *et al.* (1998) found that NO emissions from a Rijke Tube burner fueled by an ethanol spray dropped below their limit of detection when the tube was acoustically driven by an oscillating source.

There are two mechanisms for NOx formation in flames where the fuel does not contain oxygen. The most well known is the Zeldovich mechanism, also known as the thermal mechanism. The rate limiting chemical step in the Zeldovich mechanism is:

$$\mathrm{O} + \mathrm{N_2} \leftrightarrow \mathrm{NO} + \mathrm{N}$$

This is a slow mechanism relative to the overall reaction rate of a flame, with a rate of NO creation given by (Glassman, 1996):

$$\frac{d(\mathrm{NO})}{dt} = 4\times10^{14}\exp(-\frac{315\mathrm{kJ/mol}}{RT})(\mathrm{O})(\mathrm{N_2}) \qquad \text{eq. 6.7}$$

R is the ideal gas constant and *T* is the temperature. (X) is the molar concentration of X. The activation energy for this (315 kJ/mol) is quite high. Also, the concentration of the oxygen atom is determined by the equilibrium between monatomic and diatomic oxygen, which shifts toward the monatomic with increasing temperature. Because of all this, the rate of nitrogen formation in the system increases most strongly with temperature, and to a lesser extent with the oxygen concentration. As will be shown in later chapters, the temperature of the flame increases with increasing acoustic power, and the acoustic forcing produces better mixing of air with the fuel, which would elevate the concentration of oxygen near the flame.

The second mechanism for NOx formation is known as prompt NOx, because it is much faster than the Zeldovich mechanism. However its effect is dominant only in lower temperature regions. At temperatures above about 2400 K the Zeldovich mechanism dominates NOx formation (Glassman, 1996).

6.3.2 Unburnt Hydrocarbon Emissions

The gaseous hydrocarbon content of the exhaust gas stream was measured with a Rosemount Analytical model 400A flame ionization detector. In a flame ionization detector, the gas stream being sampled is mixed with a stream of hydrogen fuel, and passed through a nozzle which is charged to +90 VDC. The hydrogen fuel and a separate stream of pure air burn, producing a negligible number of ions. However, when a hydrocarbon molecule enters the flame, it produces a positive ion and an electron for each carbon atom (in an aliphatic compound). The electron is attracted to the positively charged nozzle, while the positive ion is repelled by the charged gas nozzle and attracted to a grounded detection electrode. This produces a small ionization current proportional to the number of carbon atoms passing through the detector. The current is detected and the signal amplified electronically to produce a readout. One issue which is significant to the current problem is that different types of organic gases produce different amounts of ionization. For example, the carbon atoms in acetylenic compounds produce 1.30 ions on average. However, hydrocarbon species are generally so unstable at flame temperatures that the only hydrocarbon species which is actually released from a flame is the most stable species, methane. Larger hydrocarbons are only exhausted when they can flow around the flame, rather than through it. In this simple geometry, it is unlikely that any significant amount of hydrocarbons will bypass the flame.

A Rosemount Analytical model 400A flame ionization detector measures hydrocarbons in the exhaust stream with 7 selectable full scales of 4 ppm to 1% hydrocarbons as CH_4. The device has a precision of 1%, and zero and span drift of 1% in a 24 hour period. Per manufacturer's recommendation, the device was calibrated once every 24 hours. The calibration gases are pure nitrogen and 50 ppm (±3%) CH_4 in zero air. Using the 100 ppm full scale, the detection accuracy for hydrocarbons will be ±4.5 ppm. The best attainable accuracy using the 4 ppm scale and 1% accuracy span gas is ±0.16 ppm. (Rosemount Analytical Inc., 1997)

Figure 6.11 shows the normalized hydrocarbon emissions from the flame. In general, changes with acoustic driving are within 20% of the no-sound case. The exception to this is the 800 Hz case, which brings up a significant point. It is very difficult to take data for the frequencies from 300 Hz to 750 Hz. At these frequencies, soot tends to build up rapidly on the fuel jet nozzle, leading to a solid soot cake which surrounds the fuel jet and strongly modifies the behavior of the flame. At 800 Hz, no soot cake forms, but the tip of the flame tends to be clipped off, almost as if the tip were hitting a solid wall. The tip bends over and extinguishes quickly. This behavior is assumed to provide an opening through which hydrocarbons can escape the flame without burning. This clearly indicates that any application of acoustic forcing to flames must be done with care as to the properties of the acoustic standing wave field, which can significantly modify the results.

Pont *et al.* (1998) demonstrated a reduction in unburned hydrocarbons of two orders of magnitude in their dump combustor with acoustic driving, and found that the efficiency of the waste gas they were incinerating in their device improved by 3 orders of magnitude. This probably indicates improved mixing in their system, leading to improved oxidation of combustibles. In the current system, except for the 800 and 900 Hz cases, the hydrocarbons tend to decrease from their values at 1 watt.

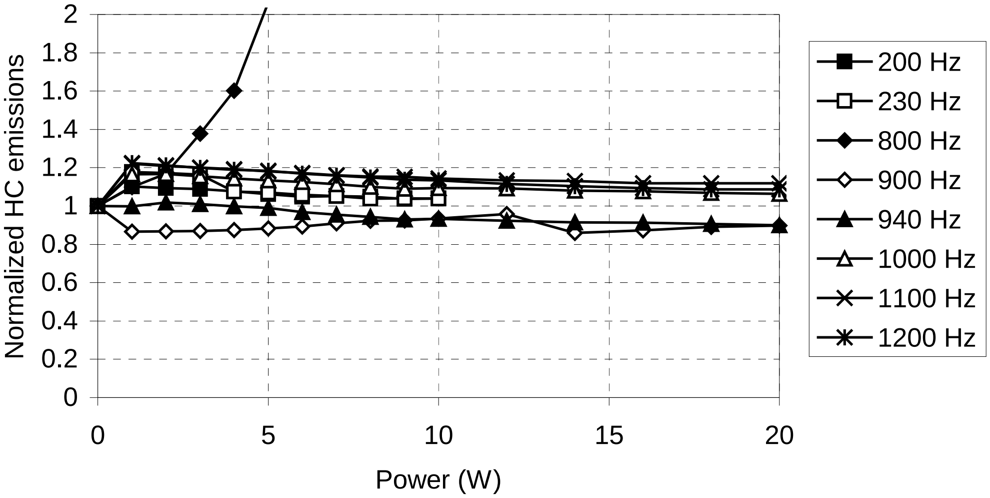

Figure 6.11. Normalized hydrocarbon emissions from the flame.

6.3.3 Carbon Monoxide

Carbon monoxide in the exhaust gas was measured with a Rosemount Analytical model 880A non-dispersive infrared (NDIR) analyzer. NDIR analyzers are applied to the analysis of a number of different gas species. They utilize the IR absorptivity of the gas being detected to determine the concentration of the gas. Specifically, two equal beams of infrared light are passed through bandpass filters. These filters pass a frequency of infrared light which is absorbed by the gas in question, but not by other gases likely to be in the stream being analyzed. The beams then enter parallel optical cells of equal length. One cell is a reference cell containing none of the gas being detected. The other cell is the sample cell, through which a steady stream of the gas being analyzed is passed. The two beams are compared by a Luft detector, which changes capacitance in proportion to the difference between its two inputs. This capacitance change is detected and electronically scaled for output.

The 880A NDIR analyzer measures the concentration of CO in the exhaust stream with selectable full scale values of 100 and 1000 ppm. The device has a precision of 1% of full scale, and zero and span drift of 1% in a 24 hour period. The manufacturer's recommended calibration frequency of once every 24 hours will be used. A noise rating of 1% of full scale is also specified. It is calibrated with pure N_2 as the zero sample and 150 ppm (±3%) CO in N_2. Based on the 1000 ppm full scale setting, the overall CO detection accuracy is ±45 ppm. A peak accuracy using the 100 ppm scale and 1% accuracy span gas is ±5 ppm. (Rosemount Analytical Inc., 1997)

Figure 6.12 shows the normalized CO emissions from the flame. As with hydrocarbons, the tendency toward incomplete combustion in the 800 Hz case is obvious from the high carbon monoxide emissions. The 900 and 940 Hz cases also exhibit high CO emissions, while the rest of the cases tend toward reduced CO emissions compared to the no-sound case.

McQuay *et al.* (1998) found reductions of up to 90% in CO emissions from their ethanol fueled Rijke tube burner. As CO is a product of incomplete combustion, this indicates that mixing was improved by the acoustic driving, but that the hydrodynamic strain rate was not increased so much that strain extinction of the flame became a problem. The conflicting trends shown in the current results denote that there are competing processes at work in the current system, and their relative dominance shifts with acoustic driving frequency.

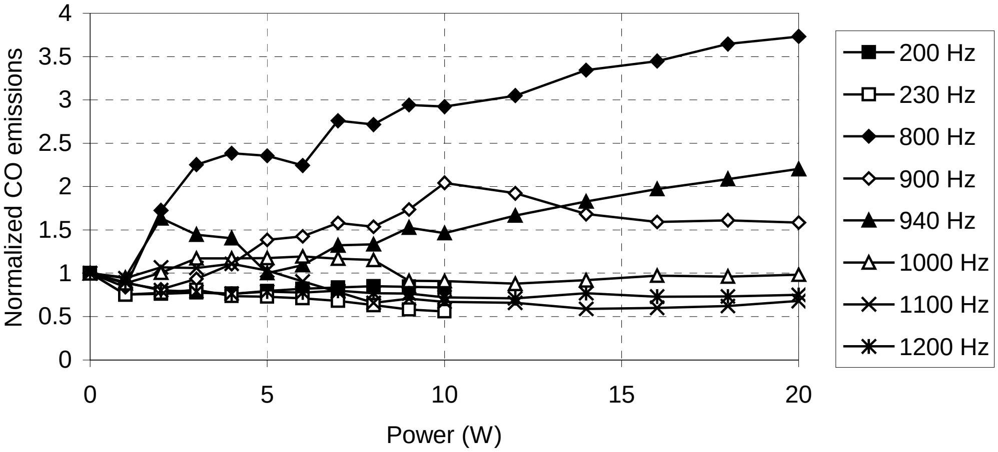

Figure 6.12. Normalized CO emissions from the flame

7 RADIANT CHARACTERISTICS

The emissions discussed in the previous chapter are undesirable pollutant emissions. By contrast, this chapter will discuss radiant heat emissions, which are often desirable. This work is driven by the observation that the normally red to orange acetylene diffusion flame becomes bright white with strong acoustic forcing, to the point of being painful to the eye.

7.1 Total visible radiation

The radiant emissions from the flame were measured by two different devices. The first is a DET 110 photodetector from Thorlabs Inc. This is simply a silicon photodiode with a battery for biasing and a switch in a compact package. The user supplies a resistive terminator which sets the magnitude and speed of the detector's voltage response curve. The photodiode detection band is 350 to 1100 nm. The repeatability of the device is within ±1%.

Figure 7.1 shows the radiant output of the flame as measured by the photodetector. The radiant output in the detection band initially increases for all frequencies tested. The 800, 940, and 1100 Hz cases peak at around 5 watts of acoustic driving. At 5 watts and 940 and 1100 Hz, the photodetector output is 66% higher than the no-sound case. Interestingly, this behavior corresponds reasonably well with the flame height shown in figure 5.5, and the power for the peak photodetector output is close to that where the emitted soot concentration drops off. The 200 and 230 Hz cases peak at 6 watts, and the 1000, 900, and 1200 Hz cases peak at 7, 9, and 14 watts respectively.

It is interesting to note here that the flame area for the 940 Hz case, (the product of the radius and height shown in figure 5.5), tends to show the same pattern as the 940 Hz visible radiation. However, the 230 Hz flame area does not drop off as the visible radiation does. This indicates that the acoustic field increases either the in-flame temperature or the in-flame soot volume fraction (which would change the emissivity of the flame). The increasing NOx emissions noted above imply increased flame temperatures. In chapter 8, it will be shown that the volume fraction of soot in the flame decreases at the powers being discussed here, which means that the emissivity of the flame can only either decrease or stay the same. This strongly implies that the temperature of the flame is increasing due to acoustic forcing.

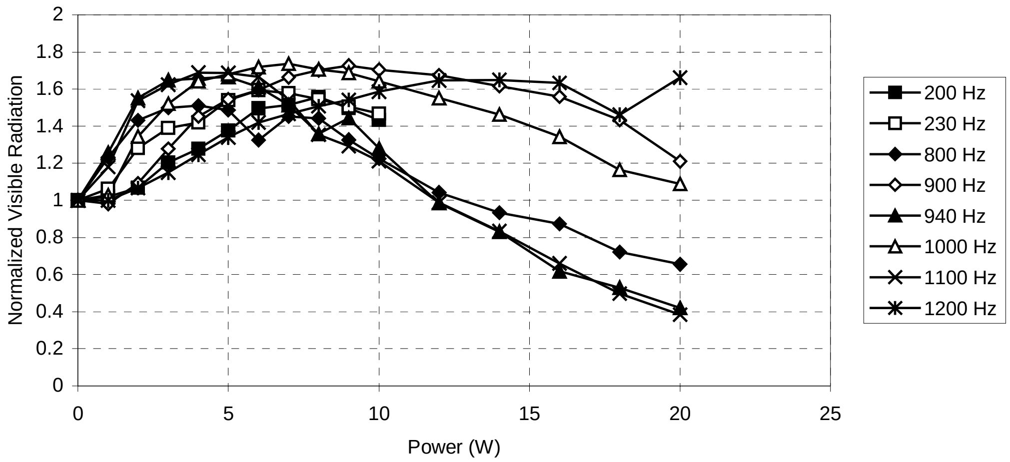

Figure 7.1. Photodetector output versus frequency and power.

7.2 Spectral Content of Visible Radiation

The radiant output of the flame was also measured with a CS400IM spectrometer from Optical Coatings Lab Inc. This device uses a linear filter, which is a series of narrow bandpass filters placed side by side. The linear filter passes a particular narrow band of the incident light to a gradient index (grin) lens behind it, and then to a photodiode. The final output of the device is the spectral composition of the light incident on it. The linear filter technique has an advantage over the traditional method of constructing a spectrometer using a diffraction grating, in that the linear filter is more temperature stable than a diffraction grating. As a diffraction grating gets hot it expands, and the characteristics of the spectrometer changes. There are two disadvantages to the device. First, it is quite view factor dependent. The device will only give accurate output if the radiation incident on the linear filter is uniform along the 13mm length of the filter. If the incident light is stronger on one side of the device than another, it will skew the output spectrum toward the more strongly illuminated side. Luckily, this can be tested simply by rotating the detector over several orientations and verifying that the output from the spectrometer is the same. Generally, this means that the detector cannot be too close to the emitting source. The second disadvantage of the device is that the grin lenses are spherically focusing, as opposed to a single long cylindrical lens. This produces a series of bright and dark spots on the photodiode detectors. This can be reduced with a diffuser plate in front of the device, but such was not available for the measurements reported here. For that reason there is a series of oscillations in the measured spectra. These oscillations are not real, and were averaged out in the processing done on the spectra.

The CS400IM is sensitive over the visible band, 400 to 700 nm. The visible band is used here in order to investigate whether there is some gas phase radiation that is contributing to the great brightness of the acoustically excited flame. Soot tends to radiate as a black body, while gas phase radiation generally shows narrow emission bands. The device is accurate to within ±1 nm. The repeatability of the photodiode power measurements is ±1%.

A graph of the spectral output of the flame without acoustic excitation is shown in figure 7.2. Because it is smooth (except for the double-peaked noise pattern, which is a product of aberrations in the gradient index lenses in the device) and peaks at longer wavelengths, it is possible that it could match the blackbody spectral emission curve at some temperature. In order to investigate this further a blackbody emission curve (Planck's law) was fit to the data. It was necessary to fit two parameters in order to match a curve to the data. First, the curve was scaled so that the average intensity between 691 and 716 nm matches that of the data. Note that this arbitrary scaling implies an assumption that the flame is gray in the visible (its emissivity is constant), but the emissivity of the flame is not necessarily one i.e. the flame is not a truly black body. The second parameter is the temperature of the blackbody curve, which was set using a least squares algorithm. Because this is a fit to the shape of the curve, not to any particular value on the curve, the uncertainties regarding flame emissivity and the view factor between the spectrometer and the flame are irrelevant. If the flame is indeed gray, then the only parameter that will effect the shape of the curve is temperature. The heavy black line in figure 7.2 is a blackbody emission curve at 2069 K. The fit is quite good. None of the narrow bands generally associated with gas-phase radiation are observed.

Figures 7.3 to 7.6 show the spectral output of the flame with various acoustic power levels and blackbody curves at the appropriate temperatures. The fit is generally good in all cases, but an odd anomaly does develop. The slight dip below the blackbody curve from 450 to 550 nm shown in figure 7.2 becomes more significant with increasing acoustic power. The dip also becomes noticeable at shorter wavelengths, although this may simply be due to the fact that the radiation from the flame without acoustics is quite low at the shortest wavelengths measured. Another discrepancy from the blackbody curve develops from 550 to 650 nm, where the data lies above the blackbody curve by an amount which increases with increasing power.

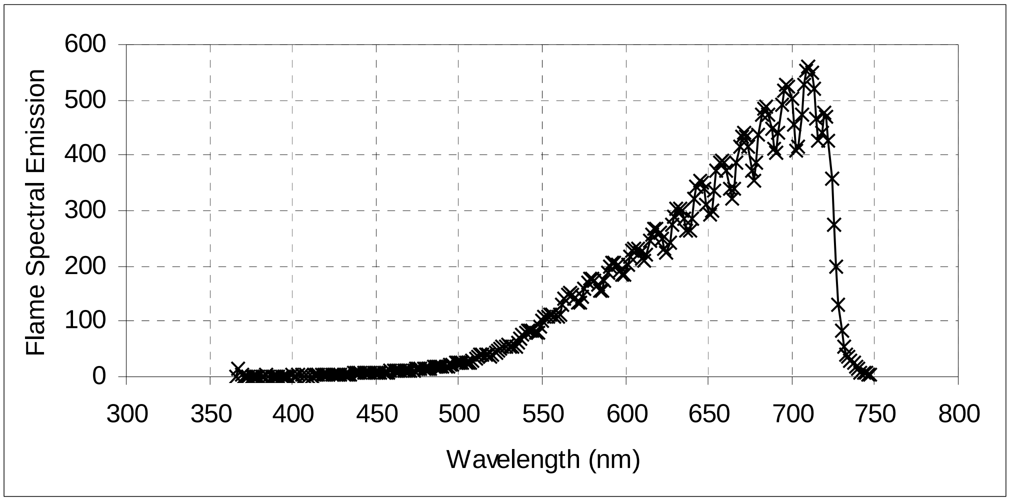

Figure 7.2. Spectral output of the flame without acoustic excitation, and matching blackbody curve. The temperature of the blackbody is 2069 K.

A further difficult point is that the temperatures found by the blackbody emission curve fits are higher than is realistic. The temperature of the non-premixed flame should be somewhere around 1900 K (Santoro et al., 1987). The temperature of a stoichiometric, adiabatic premixed acetylene air flame (calculated with the NASA equilibrium code CET89 (Gordon and McBride, 1976)) is 2539 K, well below the near 2800 K temperatures found for the flames at higher acoustic powers. Although using an inexpensive visible spectrometer is not the most accurate way to measure flame temperatures, the error should not be this great. The difficulties involve the emissivity of the soot particle cloud and a broadband absorption phenomenon associated with pyrolysis of fuel.

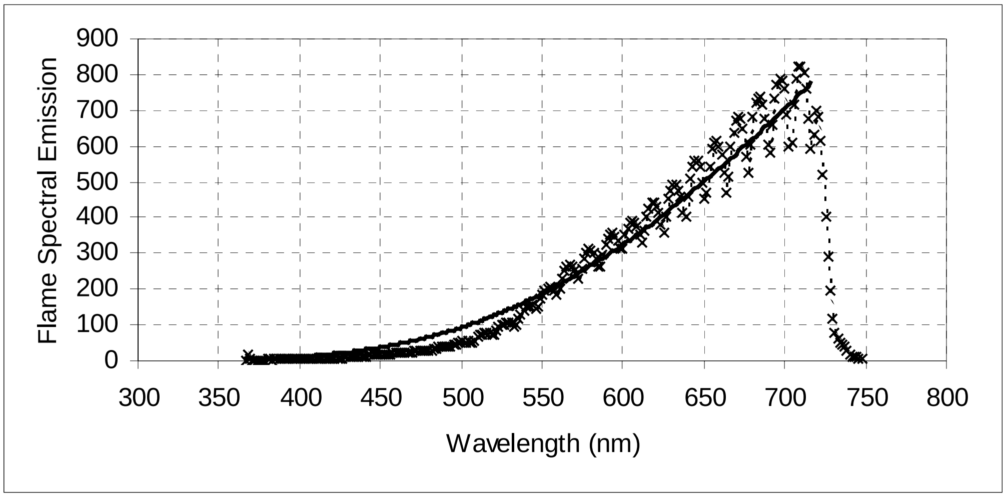

Figure 7.3. Spectral output of the flame with 500 mW acoustic excitation. Solid line is blackbody curve at 2217 K.

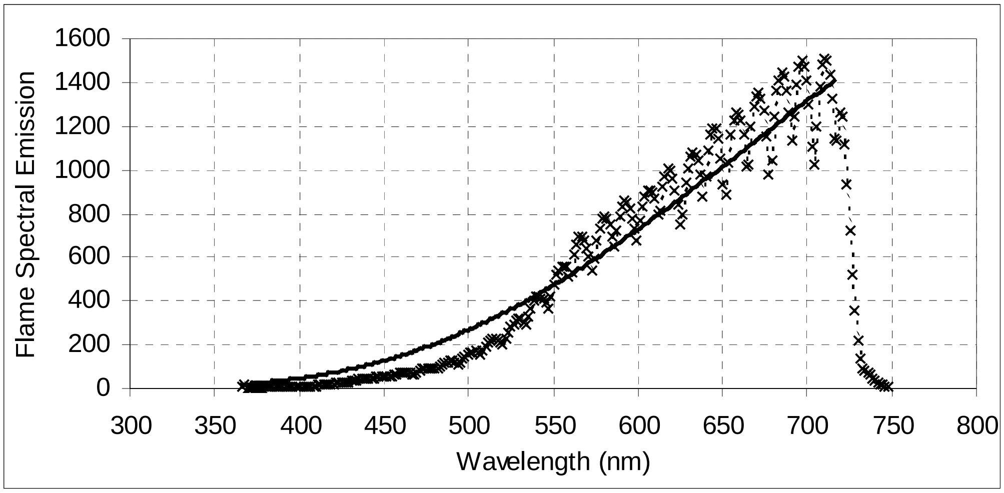

Figure 7.4. Spectral output of the flame with 2.5 W acoustic excitation. Solid line is blackbody curve at 2515 K.

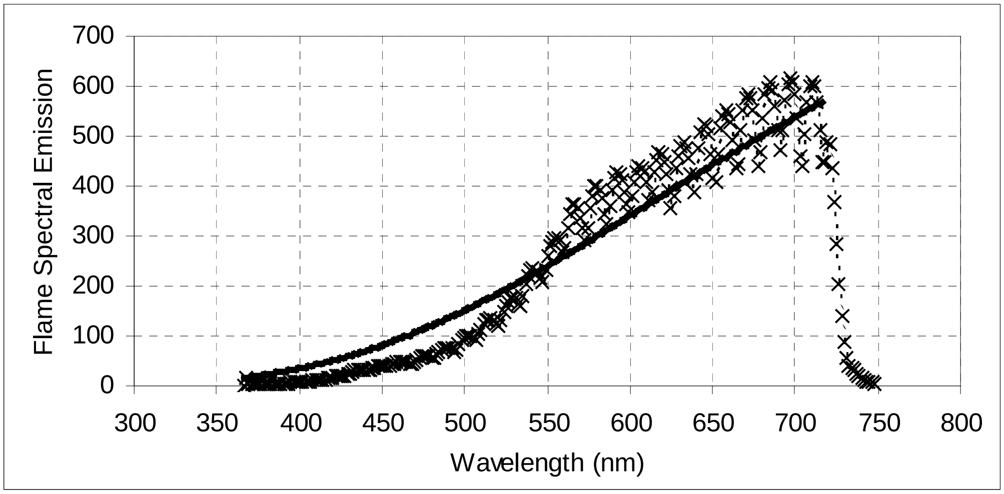

Figure 7.5. Spectral output of flame with 5 W acoustic excitation. Solid line is blackbody curve at 2785 K.

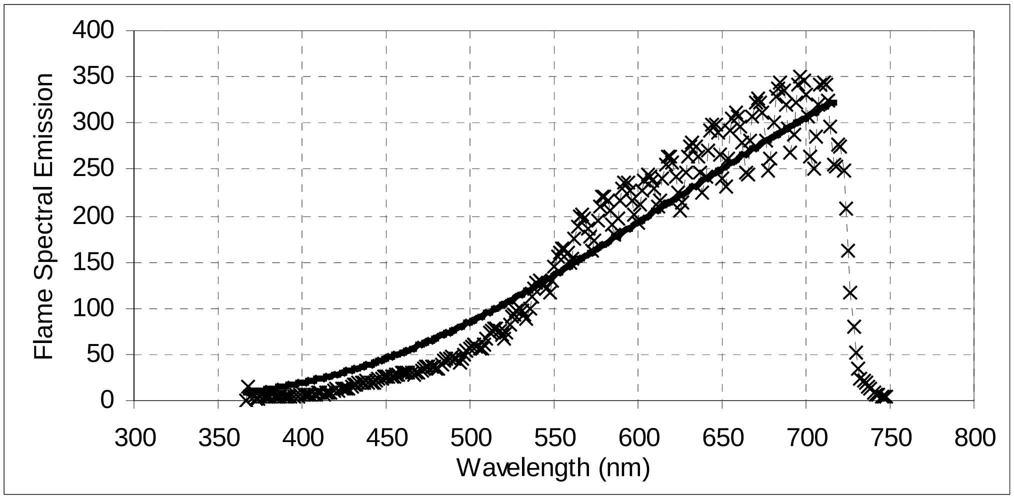

Figure 7.6. Spectral output of flame with 10 W acoustic excitation. Solid line is blackbody curve at 2776 K.

7.3 Discussion of flame spectroscopy: Broadband Spectral Absorption and Emission features

7.3.1 Short wavelength absorption due to pyrolysis

Two competing processes are contributing to the difficulty with the flame spectroscopy. The first is a broadband absorption associated with pyrolysis of a fuel. Parker and Wolfhard (1950) report a substantial absorption by heated ethane, methane, and acetylene, and ethylene. At low temperatures, the absorbed band is purely in the ultraviolet. However, with increasing temperatures, the absorbed band grows into the visible. For ethane at 915^o F, the absorbed band stretches all the way to 550 nm, which is approximately the longest wavelength demonstrating an anomalous dip in radiosity in the current study. Parker and

Wolfhard give less information about acetylene absorption, but they do show an absorption spectrum for acetylene that extends into the blue. Shaddix *et al.* (1994) also note that molecular absorption by gaseous polyaromatic hydrocarbons is significant at short optical wavelengths, but not at long ones. This broadband absorption effect accounts for the dip below the blackbody emission curve seen in the blackbody curve fits. To avoid this complication, wavelengths below 550 nm were not used in the curve fit.

7.3.2 Soot cloud emissivity

The second significant effect modifying the flame emission spectrum is that the cloud of particles which do all the emitting from the flame do not form a truly gray radiator. The emissivity of the flame is related to the optical properties of the soot particles, which were discussed in chapter 2.

The radiant flame can be modeled as a cloud of hot soot in the form of a cylinder of height H and radius r. As seen in figure 5.5, the flame height tends to be around 3 cm, and the radius around 2 mm. The soot particles are assumed to be uniformly distributed throughout the cylinder, and monodisperse in size with the properties given earlier from Köylü and Faeth (1994). The particles throughout the cylinder are furthermore assumed to be at a constant temperature. (These are fairly gross approximations, but they assist in capturing an important point.)

The optical path length, S, through the long, thin cylinder of participating media is given by Siegel and Howell (1992), $S = 1.9\ r$. If the soot is modeled with the Rayleigh Gans optical model, and the volume fraction of the soot in the cloud is f_v, then the spectral absorption coefficient, a_λ of the soot cloud is:

$$a_\lambda = \frac{f_v C_{ext}^{RG}(\lambda)}{\frac{\pi}{6} N d_p^3} \qquad \text{eq. 7.1}$$

Applying Kirchhoff's law, the spectral emissivity of the cloud is then (1992):

$$\varepsilon_\lambda = 1 - \exp(-a_\lambda S) \qquad \text{eq. 7.2}$$

It will be shown in figure 9.19 that the volume averaged soot volume fraction in the flame is between 0.3 and 12 ppm. The spectral emissivity of the flame cylinder at 3 ppm is plotted in figure 7.7. The soot cloud is definitely not gray in the visible range.

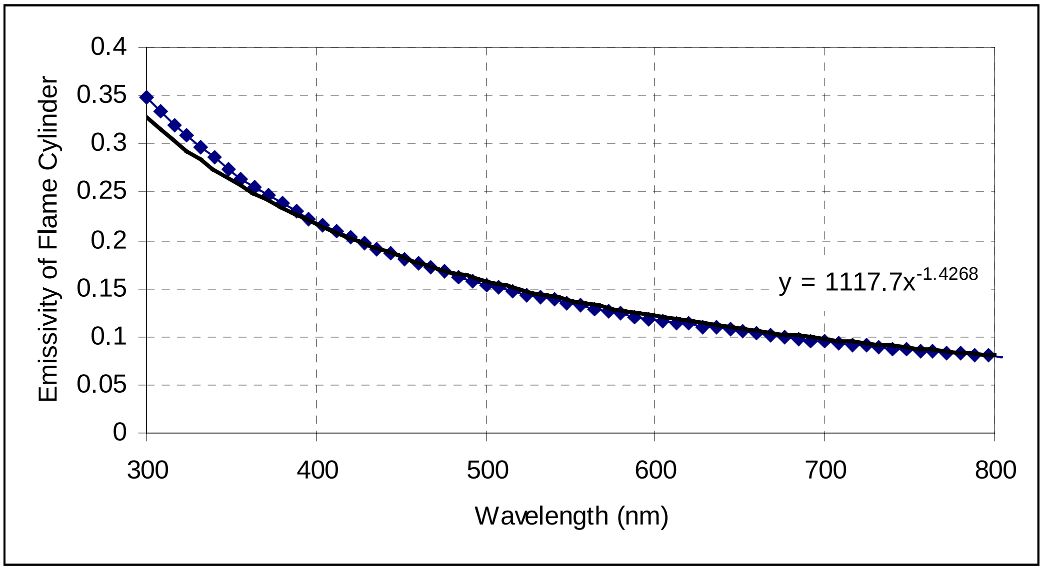

Figure 7.7. Spectral emissivity of soot cloud

The mathematical dependence of the emissivity on wavelength is complex, but a simple power curve fits the model output in the visible range as shown by the solid line in figure 7.7. The exponent in the power law fit for soot volume fractions of 0.3 ppm through 12 ppm is shown in figure 7.8.

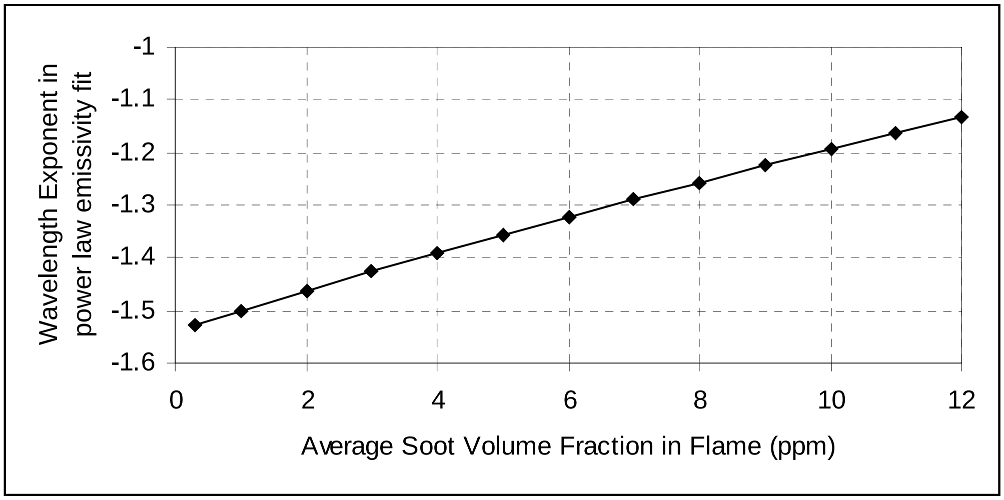

Figure 7.8. Exponent on Wavelength in Power Law Emissivity Fit.

The emission curve that is to be fit to the spectrometer data is the Planck distribution multiplied by the appropriate wavelength dependency, as determined by the average soot volume fraction in the flame. The scale factor (which makes the magnitude of the calculated and measured distributions equal) and temperature are then recalculated. Figure 7.9 shows that this technique produces no worse a fit to the no sound data than the unadjusted fit. Figures 7.10 and 7.11 show that the corrections produce a much better fit to the higher power data, such as the 2.5 and 10 W cases pictured here. Figure 7.12 shows the temperature of the fit emission curve as a function of sound power, accounting for short wavelength attenuation and variable flame emissivity. The temperature of the unforced flame is 1930 K. The maximum radiation temperature is 2637 K, at 7 W power to the speaker. These numbers are still slightly higher than expected, but are well within reason given the assumptions being made regarding temperature and soot distributions.

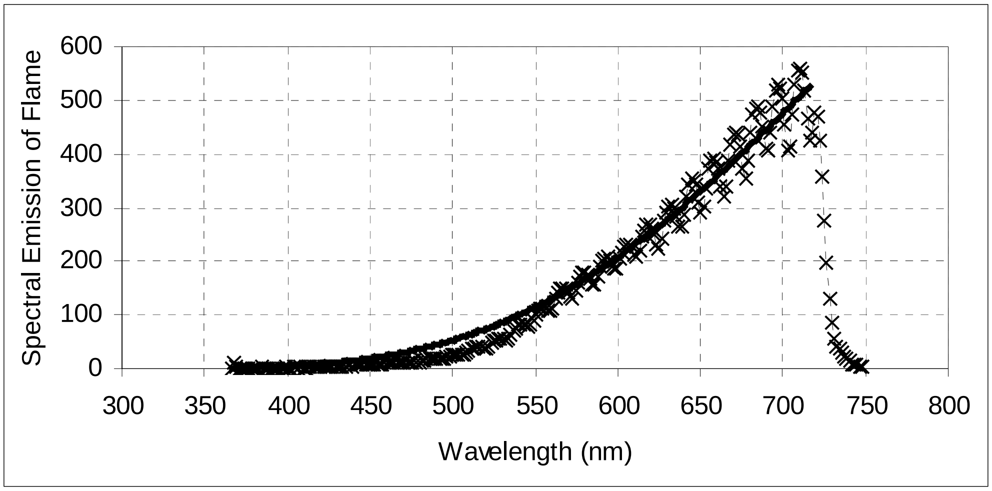

Figure 7.9. No sound spectral emissions, with curve fit accounting for variations in spectral emissivity, and for short wave absorption due to pyrolysis. Solid line is emission curve including variable emissivity, with temperature 1930 K.

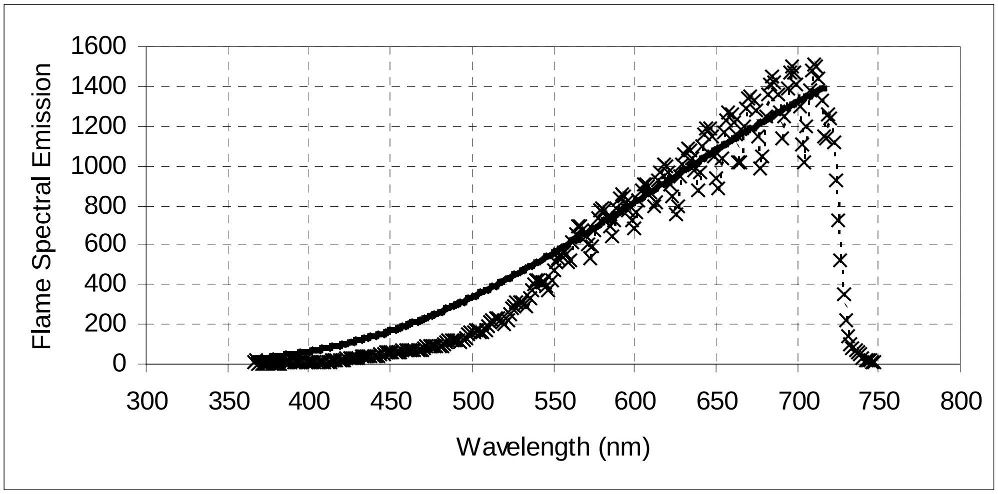

Figure 7.10. 2.5 watt spectral emissions, with curve fit accounting for variations in spectral emissivity, and for short wave absorption due to pyrolysis. Solid line is emission curve including variable emissivity, with temperature 2327 K.

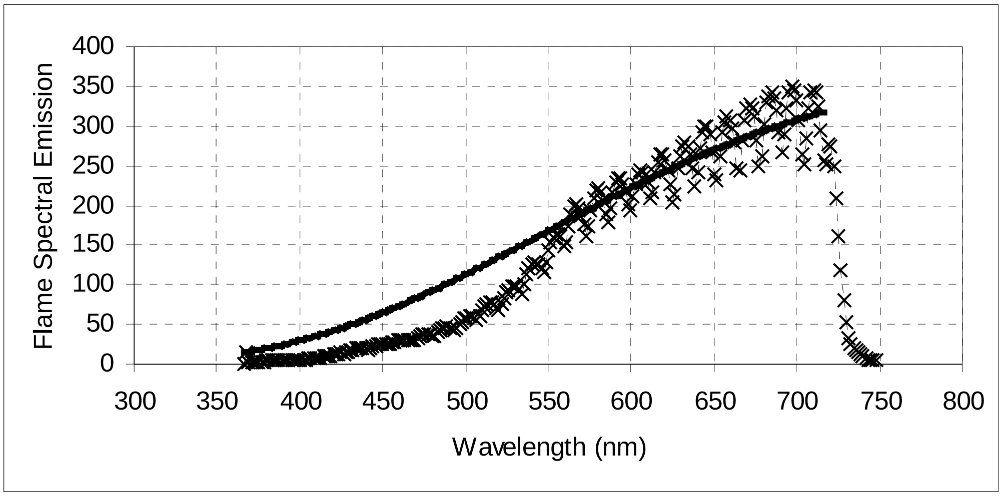

Figure 7.11. 10 watt spectral emissions, with curve fit accounting for variations in spectral emissivity, and for short wave absorption due to pyrolysis. Solid line is emission curve including variable emissivity, with temperature 2576 K.

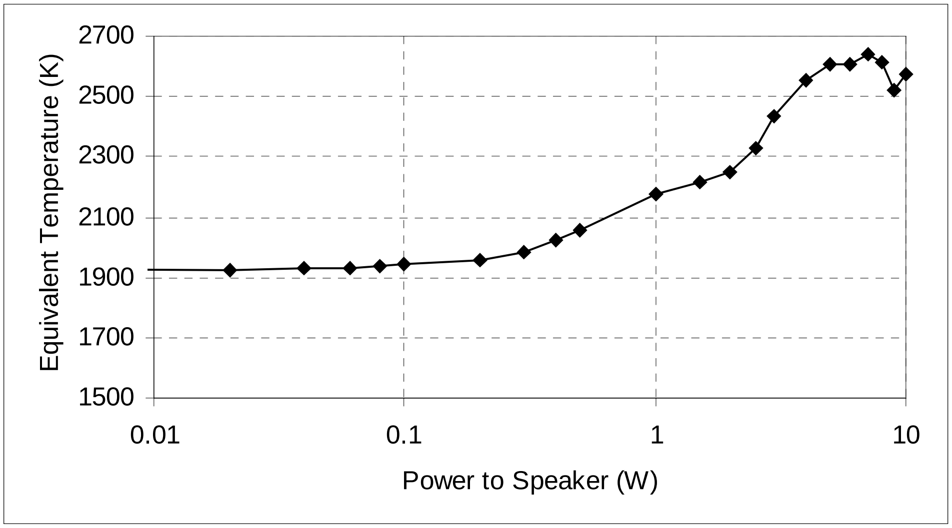

Figure 7.12. Radiation temperature for flames, adjusted for soot cloud emissivity and low wavelength attenuation due to pyrolysis.

8 IN FLAME SOOT PROFILES

In order to more completely understand the effect of acoustics on the flame, and particularly the soot particles therein, it is worthwhile to investigate the changes to the soot concentration in the flame as a result of acoustic forcing. The concentration of soot in the acoustically forced flame will be analyzed with a laser extinction experiment similar to that used in the global soot extinction experiment described in chapter 6. What is added here is spatial resolution. A tomographic reconstruction technique is used to find the radial distribution of soot in the flame, allowing some detail in descriptions of flame structure.

8.1 Experimental apparatus

The extinction measurement was done with an apparatus similar to the one described in section 6.2. The particular construction of the apparatus is shown in figure 8.1, and the numbers in this description refer to the numbered parts in the drawing. A two dimensional traverse is positioned in order to provide controlled vertical and horizontal displacement. The traverse is made of very stiff stainless steel box beams (11), 52 mm on a side, fitted into carriages with precision linear bearings (13). The beam of the vertical traverse is anchored to the optical table (14) supporting the experiment. A jack screw (4) is anchored to the carriage of the vertical traverse, which is in turn attached to the carriage of the horizontal traverse. This allows the horizontal bar to be independently lifted and slid horizontally. A digital caliper (12) is attached to the horizontal carriage and bar to provide a quick and convenient reading on the displacement of the horizontal carriage. The caliper is accurate to ±0.1 mm. The vertical displacement of the carriage assembly was measured relative to the surface of the optical table with a set of vernier calipers (13). The vertical measurement was accurate to ±0.3 mm.

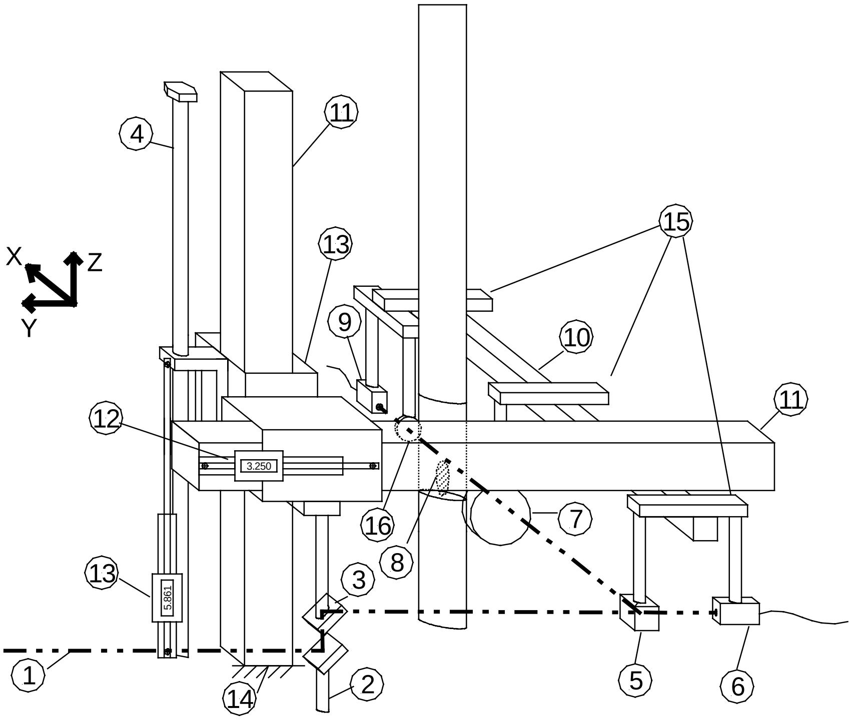

Figure 8.1. In-Flame Extinction Apparatus

An arm (10) is attached to the end of the horizontal bar that supported and aligned most of the optics used in the measurement. The arm was cantilevered out from the horizontal bar, with several mounting stubs (15) attached to the arm. Each stub was designed to support an optical component. All components on the arm are fixed relative to the others, so that the alignment of the optics is fixed.

The optical path begins with an argon ion laser, whose beam (1) is immediately filtered by an ND 2.5 neutral density filter (not shown). This is necessary to reduce the intensity of the laser beam to the linear range of the photodiode detectors used to receive the beam. The beam aims at a mirror (2) directly below the carriage assembly which is mounted to the optical table. This mirror reflects the beam vertically upward to a vertically mobile mirror (3) mounted on the carriage assembly. That mirror reflects the beam along the length of the horizontal beam to a beamsplitter (5) attached to the first mounting stub on the arm. The beamsplitter passes one beam directly to a reference receiver (6). This receiver monitors changes in the beam strength due to laser instability or other attenuation upstream from the beamsplitter. The other beam leaving the splitter travels in the x direction as labeled on the figure and passes through a focusing lens (7). This lens takes the laser beam, approximately 2 mm in diameter, and focuses it at the flame (8) to improve the spatial resolution of the measurement. The beam diameter at the flame is approximately 0.5 mm, which was the narrowest spot achievable. The beam leaves the lens, passes through the glass cylinder surrounding the flame, and attenuates as it passes through the flame. It exits the back of the glass cylinder and passes through a 488 nm laser line filter (16). This filter, which has a full width half max bandwidth of 10 nm, is necessary to minimize noise in the measurement due to broadband radiation from the flame. The filtered beam then goes to the signal receiver (9). Both of the receivers are DET 110 high speed photodetectors from Thorlabs Inc. The devices are 3.6 mm x 3.6 mm silicon photodiodes packaged with a battery, a switch, and a BNC connection. They have a repeatability of ±1%. Each photodetector is terminated with a 50 kΩ resistance, which produces a step-response decay time of 30 microseconds, more than adequate for measurements at 940 Hz. The signals from the two devices were transmitted to a Tektronix TDS

3034 digital phosphor oscilloscope. In the oscilloscope, the voltage from the signal receiver is divided by the voltage from the reference receiver to give the transmittance of the soot cloud in the flame along the line of the laser beam. This transmittance measurement is resolved in terms of time and the y -and z-dimensions of space, however, the variations in time at a point (time was referenced to the phase of the acoustic driving) were small compared to variations with both space and acoustic driving. Time-averaged extinction measurements were quite repeatable, so they were used. The averaging was done over approximately 10 acoustic cycles, a total of 10,000 readings.

Note that, because of refraction due to the glass cylinder surrounding the flame, the position of the beam on the receiver will not be perfectly centered except when the beam goes through the center of the cylinder. A ray transfer matrix calculation (Hecht, 1987) was done to find the ray's departure from its intended position at the flame and at the receiver as a function of the distance from the centerline of the cylinder to the position of the ray entering the glass cylinder. The output of that calculation is shown in figure 8.2. The beam refracts toward the centerline slightly as it enters the glass cylinder, leading to a slight deviation of position toward the centerline at the flame. More significantly, the beam refracts toward the outside substantially as it exits the cylinder. The beam at the receiver has a diameter of 1 mm, and the detector is a square 3.6 mm on a side, so there is substantial signal loss due to the beam missing the detector at radial positions greater than 25 mm from the centerline of the cylinder. Luckily, as shown in chapter 5, the flame is less than 10 mm in diameter, so it is not necessary to take measurements on the outer edge of the cylinder.

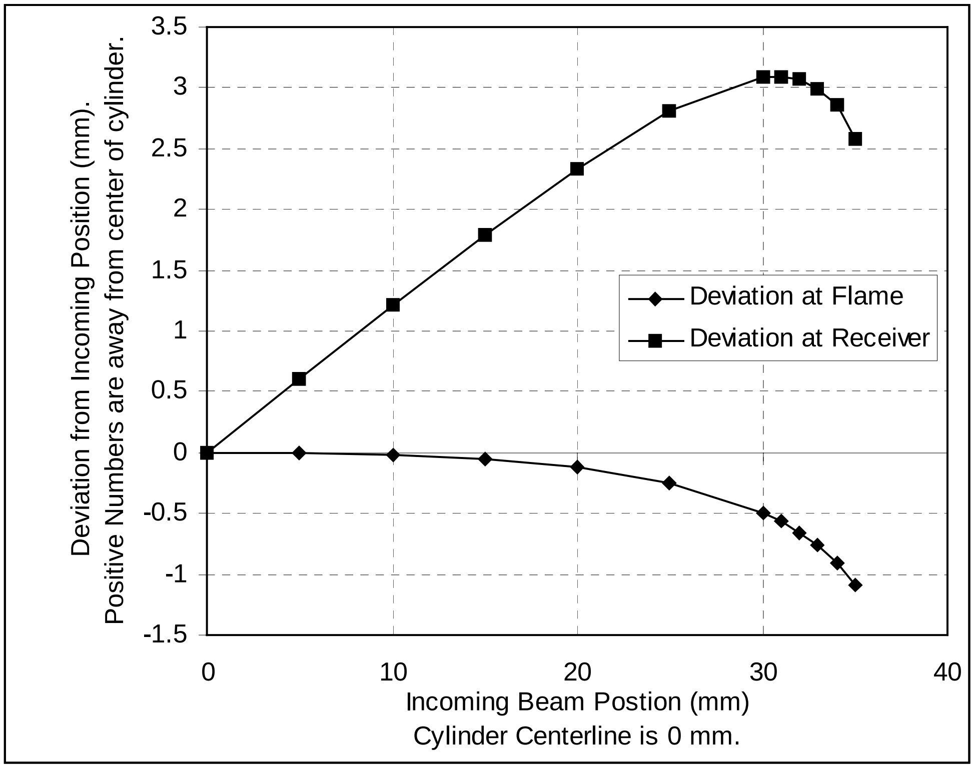

Figure 8.2. Deviation of beam position at the flame and at the receiver increases as the beam moves from the centerline of the cylinder to its edge.

8.2 Tomographic Reconstruction

The primary goal of the measurement was to develop a spatially resolved image of the soot in the flame. The extinction measurement is resolved in the y- and z-dimensions labeled on figure 8.1, but it is an integrated measurement along the path of the laser beam, which is the x-dimension. The flame, however, is an axisymmetric system. Its axial coordinate coincides with the z-dimension, but a series of x-integrated measurements in the y-direction must be analyzed together to reproduce the radial distribution of soot in the flame. This process is known as one dimensional tomography.

The basic problem in one dimensional tomography can be further explained by the simple example of a uniformly absorbing cylinder as pictured in figure 8.3(a). In this example, the cylinder has a radius of 10 units and a turbidity of 0.005 per unit length. Note that such a small number is necessary for this method to work. As shown in eq. 2.18, attenuation of a light beam by a turbid body is an exponential decay. This analysis only works if the attenuation along the total path can be modeled with reasonable accuracy as the sum, rather than the product, of the attenuations per unit length along the path. This is equivalent to saying that the flame must be optically thin i.e. the product of the turbidity τ and diameter *D* of the flame should be less than 0.1.

The origin of the y-coordinate in figure 8.3(a) is along the centerline of the circle. The total attenuation of the laser beam recorded at each point *y* is shown in figure 8.3(b). The problem is to reproduce the situation pictured in (a) from the data of (b).

The deconvolution expression for this operation is known as the Abel transform (Abel, 1826). If a property *B* is distributed axisymmetrically (*B=B(r)*), and the projection to the *y*-axis is *P(y)*, the following will hold:

$$B(r) = -\frac{1}{\pi}\int_r^\infty \frac{\frac{dP(y)}{dy}}{(y^2 - r^2)^{1/2}}\,dy \qquad \text{eq. 8.1}$$

Eq. 8.1 is quite noise sensitive, in that the derivative of experimental data *P(y)* must be calculated, and it is also divergent at $y=r$.

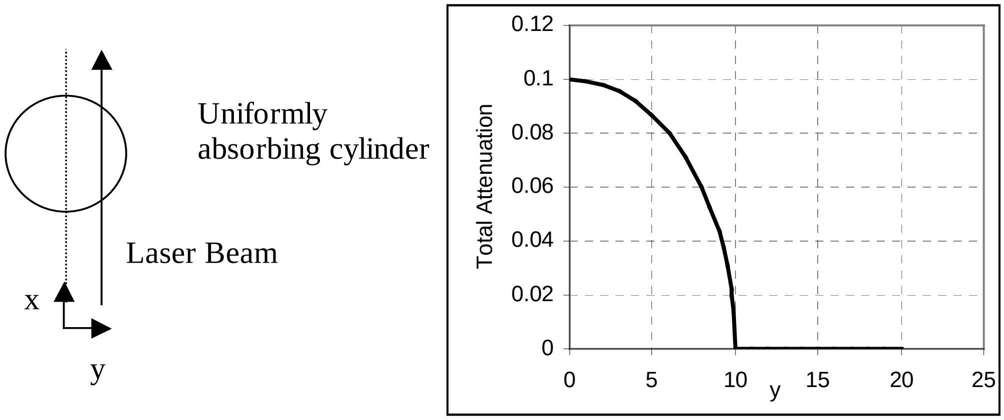

(a) (b)

Figure 8.3. Laser beam passing through a uniformly attenuating cylinder of radius 10. (a) problem geometry. (b) total attenuation at each point.

Various discrete methods for performing the deconvolution were described by Dasch (1992). (Note that there are, by the author's own admission, a number of significant printing errors in this article. Any worker using it should obtain the errata (1992).) Dasch compared two and three point interpolations of the Abel transform with three other methods by other authors. He showed that all of the projection methods fit the general form:

$$B_i^r = \frac{1}{\Delta y} D_{ij} P_j$$

eq. 8.2

B^r_i is the reconstructed, discretized form of $B(r)$, and P_j is the discretized form of $P(y)$. In this formulation, Δy, the step size in the data, and Δr, the step size in the radial distribution, are uniform and equivalent. The deconvolution operator D_{ij} is dominated in all methods by the diagonal and the just-above-diagonal terms, which have opposite signs.

The form for D_{ij} which Dasch finds to minimize the effect of noise in the data is the three point quadratic expansion of the Abel transform. It is also easier to calculate than some of the other transforms he reviews. In this form, D_{ij} is given by the following formulas:

$$D_{ij} = \begin{cases} 0 & j < i-1 \\ H^0_{i,j+1} - H^1_{i,j+1} & j = i-1 \\ H^0_{i,j+1} - H^1_{i,j+1} + 2H^1_{i,j} & j = i \\ H^0_{i,j+1} - H^1_{i,j+1} + 2H^1_{i,j} - H^0_{i,j-1} - H^1_{i,j-1} & j \geq i+1 \\ H^0_{i,j+1} - H^1_{i,j+1} + 2H^1_{i,j} - 2H^1_{i,j-1} & i=0,\ j=1 \end{cases}$$

eq. 8.3

where:

$$H^0_{ij} = \begin{cases} 0 & j=i=0 \text{ or } j<i \\ \dfrac{1}{2\pi}\ln\left\{\dfrac{\left[(2j+1)^2-4i^2\right]^{1/2}+2j+1}{2j}\right\} & j=i\neq 0 \\ \dfrac{1}{2\pi}\ln\left\{\dfrac{\left[(2j+1)^2-4i^2\right]^{1/2}+2j+1}{\left[(2j-1)^2-4i^2\right]^{1/2}+2j-1}\right\} & j>i \end{cases}$$

$$H^1_{ij} = \begin{cases} 0 & j<i \\ \dfrac{1}{2\pi}\left[(2j+1)^2-4i^2\right]^{1/2} - 2jH^0_{ij} & j=i \\ \dfrac{1}{2\pi}\left\{\left[(2j+1)^2-4i^2\right]^{1/2} - \left[(2j-1)^2-4i^2\right]^{1/2}\right\} - 2jH^0_{ij} & j>i \end{cases}$$

eq. 8.4

The first 10x10 entries of the three-point Abel deconvolution operator are plotted in table 8.1. The operator is dominated by positive terms on the main diagonal. Terms above the main diagonal are negative, smaller than the main diagonal term, and tend to decay rapidly to zero as they go farther away from the main diagonal. This means that the absorptance of the part of the flame at $r=y$ has the strongest effect on the measurement. The absorptance due to the flame at $r>y$ has an effect on the measurement which must be subtracted out of the measurement, but that effect diminishes as r becomes larger. Note that the first term below the diagonal is greater than zero. This is essentially data smoothing. Because of this term the three point Abel transform does not precisely obey the hole theorem, which states that the reconstruction of the field at a point does not depend on projections at smaller radii. A hole of radius R_1 in the center of the cylinder should not be detected at $y>R_1$. Violating the hole theorem with a smoothing operation sacrifices some ability to capture sharp edges in exchange for less overall noise sensitivity.

0.525	-0.293	-0.101	-0.039	-0.021	-0.013	-0.009	-0.007	-0.005	-0.004
0.104	0.207	-0.165	-0.049	-0.023	-0.014	-0.009	-0.007	-0.005	-0.004
0.000	0.074	0.154	-0.113	-0.035	-0.018	-0.011	-0.008	-0.006	-0.004
0.000	0.000	0.061	0.129	-0.091	-0.029	-0.014	-0.009	-0.006	-0.005
0.000	0.000	0.000	0.053	0.113	-0.078	-0.024	-0.012	-0.008	-0.006
0.000	0.000	0.000	0.000	0.047	0.101	-0.069	-0.022	-0.011	-0.007
0.000	0.000	0.000	0.000	0.000	0.043	0.093	-0.063	-0.020	-0.010
0.000	0.000	0.000	0.000	0.000	0.000	0.040	0.086	-0.058	-0.018
0.000	0.000	0.000	0.000	0.000	0.000	0.000	0.037	0.081	-0.054
0.000	0.000	0.000	0.000	0.000	0.000	0.000	0.000	0.035	0.076

Table 8.1. Deconvolution Operator D_{ij}: first 10 x 10 values.

Applying the deconvolution operator D_{ij} to the data in figure 8.3b leads to the radial distribution F^r_i shown in figure 8.4, along with the actual (flat) radial distribution $F(r)$. Figure 8.5 shows a ring, 2 sine waves, and an exponential decay profile. The method is more successful at reconstructing smooth profiles than abrupt changes, but it has reasonable success in all cases.

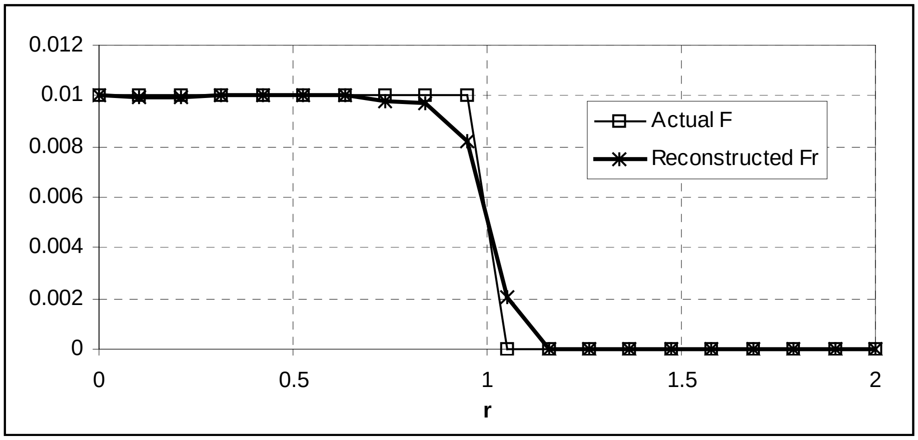

Figure 8.4. Deconvolution of figure 8.3b, compared to actual situation

One situation that the reconstruction has problems with is when the projection does not go to zero at the outermost cell. Practically, this might happen if the zero crossing of the receiving sensor were not set properly, as in figure 8.6a, or if the data simply were not taken far enough out, as in figure 8.6b. In both of these cases the projection does not go to zero at the outer edges of the data. The reconstructed data lies below the actual *F*, except near the outer edge, where the reconstruction turns up. It is very important when using this method that the data actually go to zero at the outside edges. Luckily, the characteristic upturn in the reconstruction at the outer edge consistently occurs when the data does not go to zero, and the error can be easily recognized.

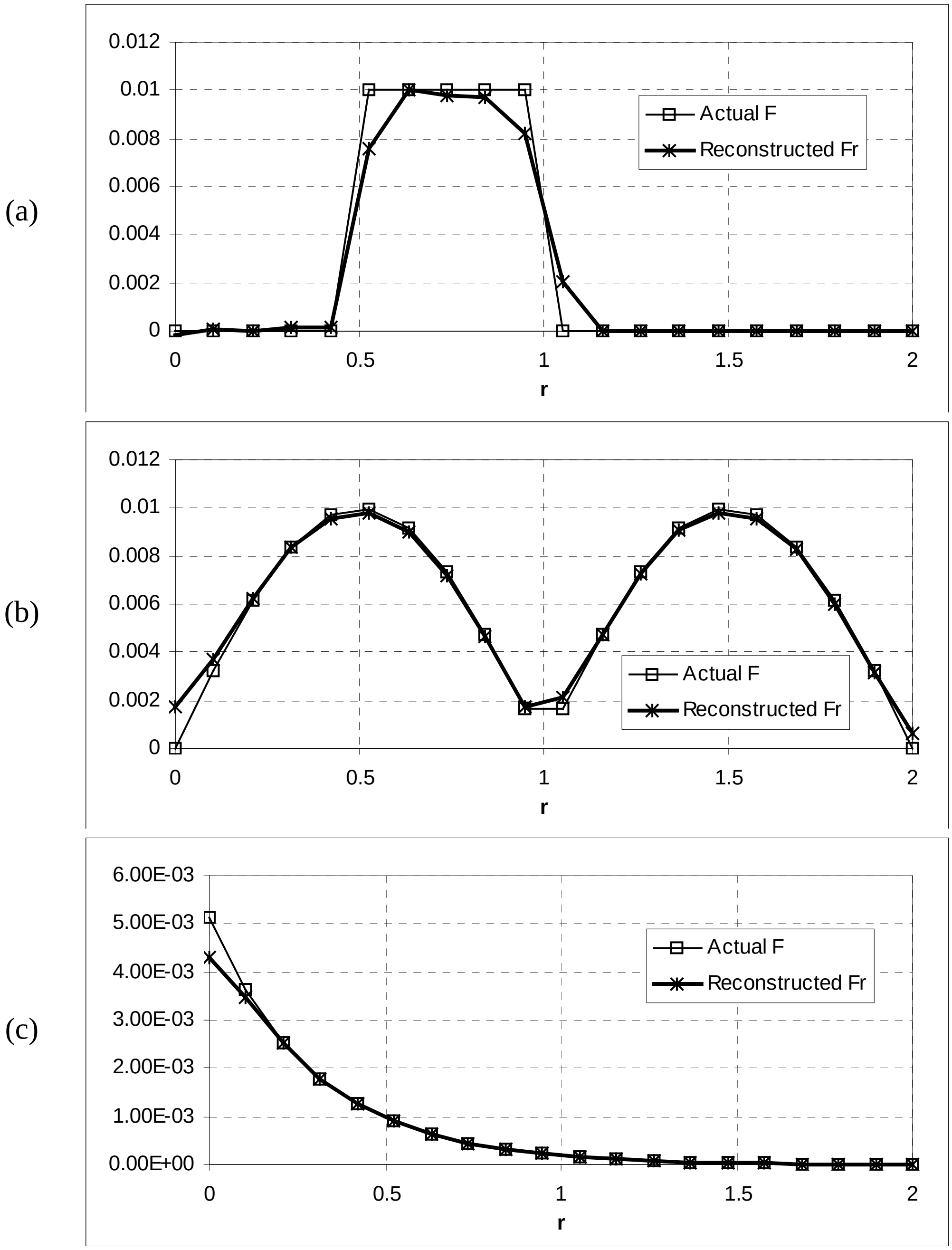

Figure 8.5. Reconstruction of (a) ring, (b) sine, and (c) exponential profiles

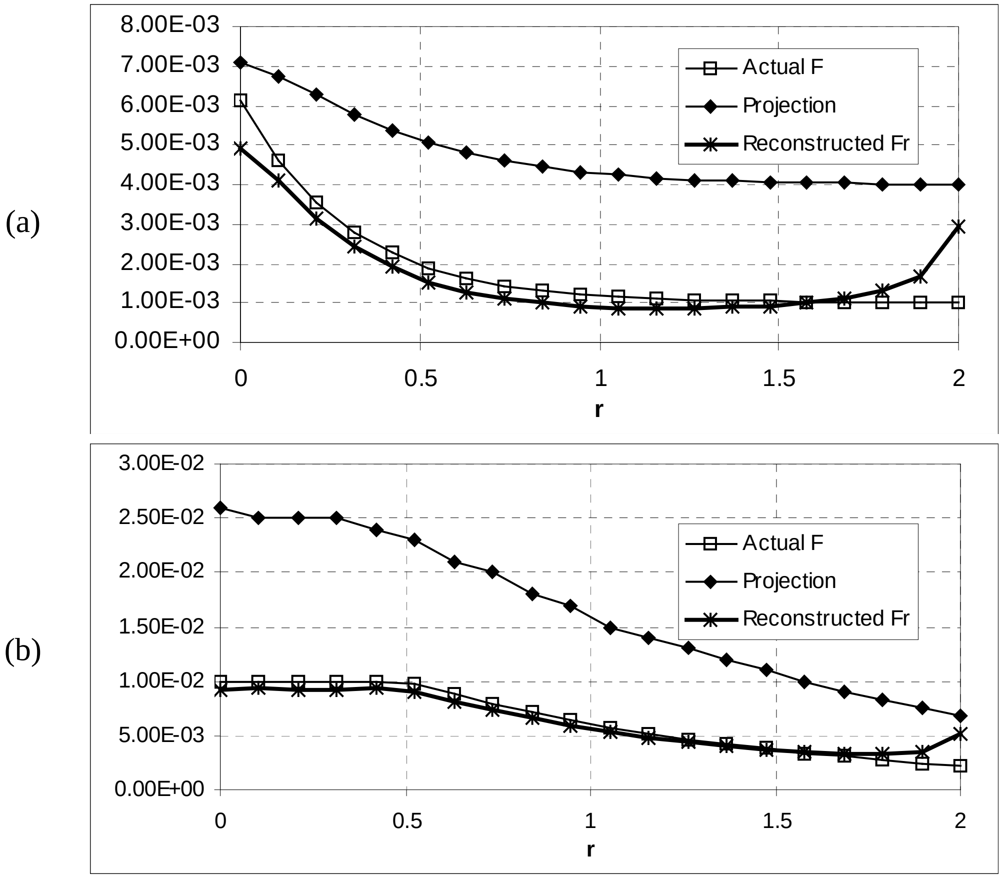

Figure 8.6. Non-zero projections at outside edge lead to errors in reconstruction. (a) Zero Offset. (b) Insufficient outer radius of data.

8.3 Conversion of reconstructed data to soot profiles

The raw data for this measurement is the transmittance of the laser beam through the flame zone. To make this data compatible with the reconstruction technique above, each data value must be subtracted from one to give the absorptance of the flame. The data then goes to zero at the edges of the flame, and tomographic reconstruction will work. The reconstruction process yields the absorptance per unit length at each radial position, which is then multiplied by *Δy*, 0.5 mm, and subtracted from 1 to give the transmittance of the layer, *τ*.

To convert to the concentration of soot particles at each position, the Rayleigh optical model is used. As noted by Lin (1996), the Rayleigh model is still used for soot extinction measurements inside the flame itself, where there has been little time for aggregation. A more detailed model of soot extinction (such as Rayleigh-Gans) would be more accurate if spatially resolved data regarding soot structure were available for the flame. Without that data, the more advanced models are unlikely to provide substantial improvements in accuracy, and they substantially add to the computational complexity of the problem. Given the Rayleigh model, a further simplification can be made by neglecting scattering altogether. Figure 8.7 shows that this simplification represents a 10% error or less for particles 60 nm and smaller. Since the primary particle sizes found by various researchers are generally 50 nm and below (Table 2.1) this should introduce less than 5% error in the volume fraction calculation.

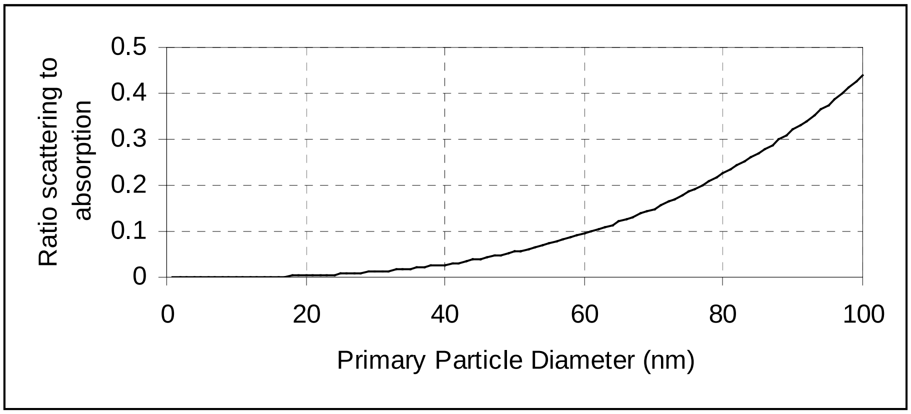

Figure 8.7. Ratio of Scattering to Absorption Cross Sections in the Rayleigh optical model.

With these simplifications, the volume fraction of soot can be calculated quite simply:

$$f_v = \frac{-\ln(\tau)\dfrac{\lambda}{\Delta r}}{6\pi E(m)} \qquad \text{eq. 8.5}$$

8.4 Noise Sensitivity of Tomographic Reconstruction

As expressed in eq. 8.1, the reconstruction requires discretized derivatives of experimental data. This leads to substantial noise sensitivity in the data. Dasch notes that the coefficients in the matrix D_{ij} are not dependent on Δr, which means that there is no accounting for data spacing in the transform. Because of this, the transform can have problems with data sampled so closely that the noise in adjacent measurements is greater than the real difference between points. For this reason, Dasch recommends caution in increasing the density of data samples. It is obvious from figure 8.5, though, that this will reduce the accuracy with which the reconstruction captures sharp changes. In this research, the spatial resolution was restricted to the 0.5 mm diameter of the beam spot at the flame.

The data from this experiment were taken from a point 5 mm on one side of the flame center to a point 5 mm on the other side. The actual flame center was determined by first finding the edges of the flame, which are the points where the derivative of the projection data with respect to y was maximum and minimum (most positive and most negative). The flame center is the point halfway between the flame edges. The data was then “folded,” i.e. each pair of data points equidistant from the center were averaged, to produce a data series that started at y=0 (the flame center) and ended outside the flame, where the absorptance is zero.

Dasch also recommends smoothing any data before deconvoluting it. For this work, it was found that a moving average algorithm, with an averaging window of 3 points, and a center weighting of 7 times the end points was adequate. This is a light smoothing operation, but it did reduce noise effectively.

Because there is a logarithm in the conversion from transmittance to volume fraction, it is not immediately obvious what the effect of error in the projection will be. However, the value of transmittance tends to be very near one. For this reason, the percent error in the projection data propagates on a roughly one to one basis to the error in the volume fraction.

Experimental results indicate the repeatability of the raw projection data (before the data was folded about the center) to be within 50%. This value dropped to within 30% after the flame center was found, indicating that movement of the flame center is a substantial source of variations in the raw projection data. The repeatability of the soot volume fractions was also within 30%.

8.5 Results

The flame was excited at 940 Hz and probed with the in-flame extinction apparatus. The flame was probed at heights of 6, 8, 10, 12, 14, 16, 18, 20, 22, 30, and 70 mm above the burner surface. The heights below 6 mm were obscured by the ring holding the steel screen in place. Beyond the no sound case, 21 power levels were tested, from 20 mW to 10 W.

Figure 8.8 shows the soot profiles at all power levels at 6 mm elevation. The no sound case peaks at 2 mm from the center with a volume fraction of 51 ppm. The flame narrows with increasing power, with the 20 to 40 mW profiles peaking at 2 mm, the 60 to 400 mW profiles peaking at 1.5 mm, the 500 mW to 2.5 W profiles peaking at 1 mm, and the higher powers peak at the centerline. The maximum volume fraction is 68 ppm at 100 mW, r = 1.5 mm. The peak volume fraction for each power level increases with increasing power from 0 to 100 mW, then decreases with further increases in power. The trend of increasing, then decreasing volume fractions with increasing power is consistent at all heights. To reduce some of the clutter in subsequent graphs, only a few representative power levels (0, 100, and 500 mW, 2.5 and 10 W) will be shown at the other heights. Those profiles are in figures 8.9 to 8.18.

At almost every elevation except 70 mm, which is well above the luminous zone, the no sound case exhibits high volume fractions at the outermost radius of any case. The flame tends to narrow with increasing power. It also narrows with increasing height, which is the expected “candle flame” shape. The 100 mW case almost always exhibits the highest soot volume fraction of any case. The no sound case generally peaks slightly lower, while the volume fraction in the high power cases goes below the limits of detection.

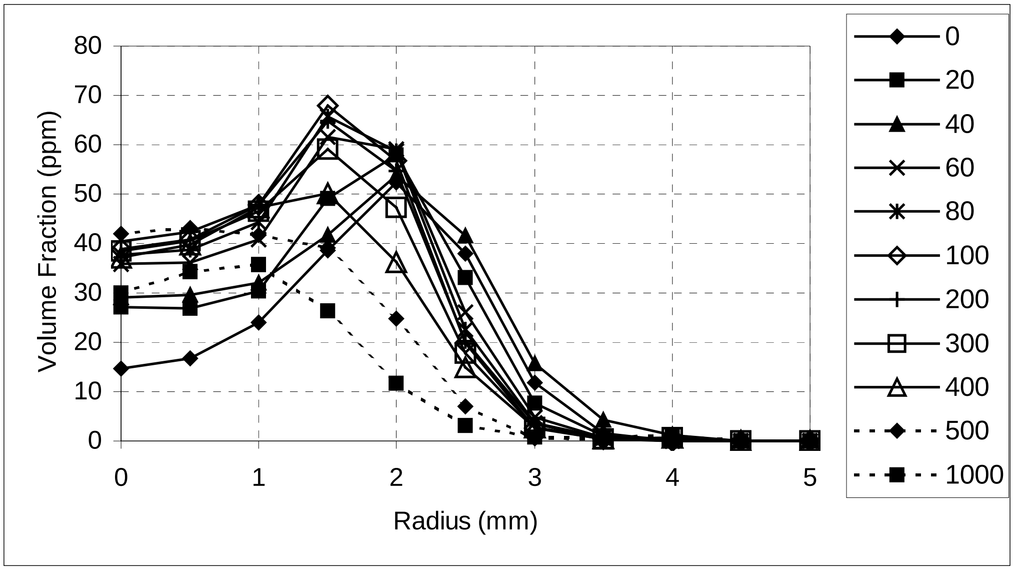

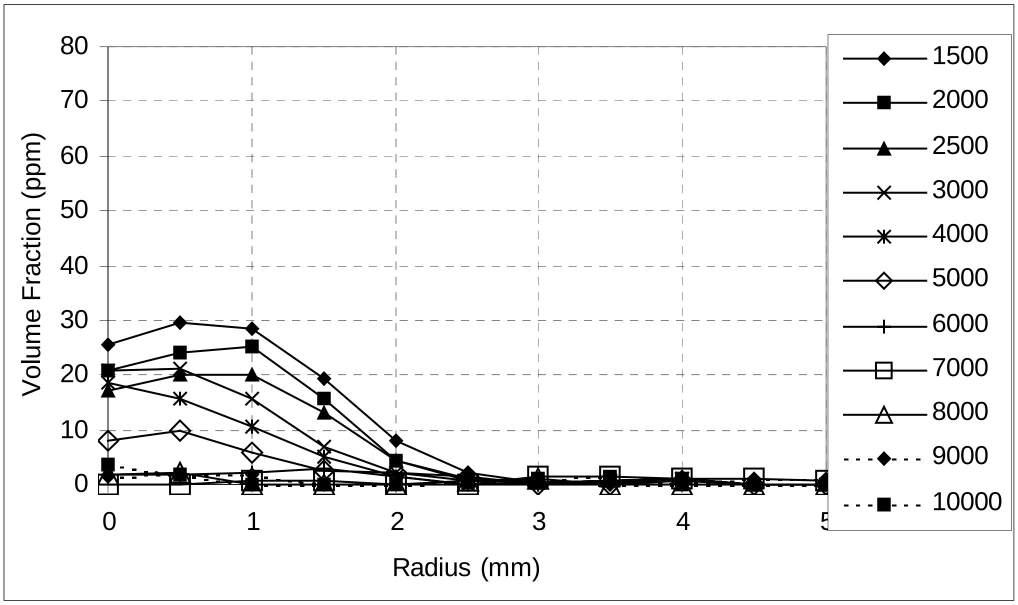

Figure 8.8. Soot volume fraction profiles at all power levels at 6 mm elevation. Labels in legend are power levels in milliwatts.

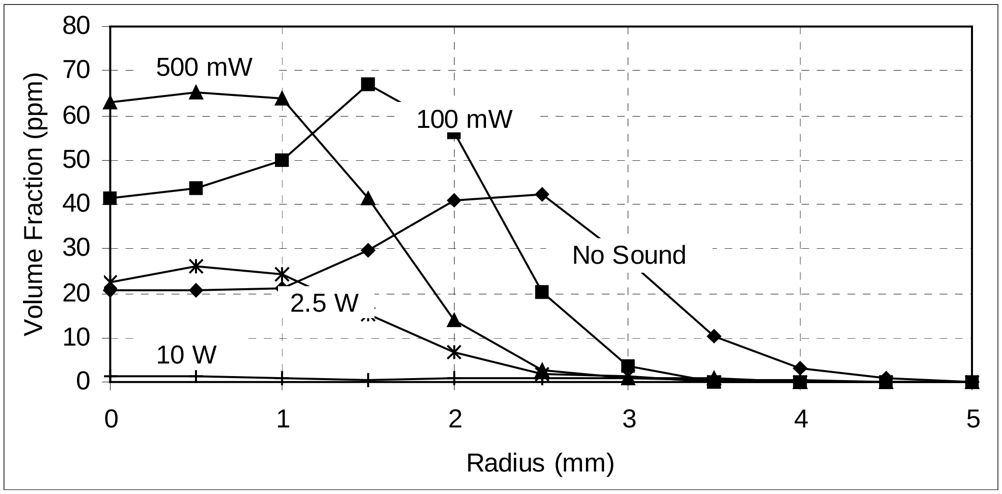

Figure 8.9. Soot volume fraction profiles at 8 mm elevation above burner face at selected sound power levels.

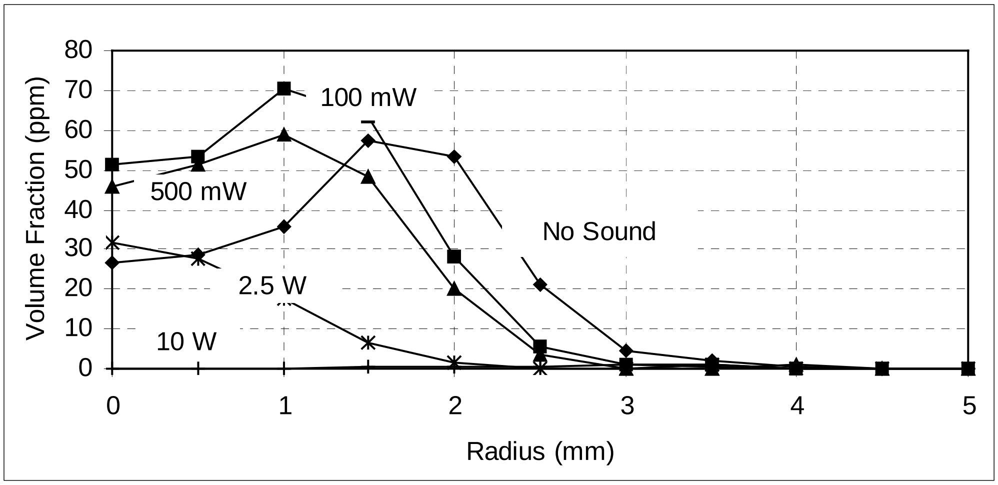

Figure 8.10. Soot volume fraction profiles at 10 mm elevation above burner face at selected sound power levels.

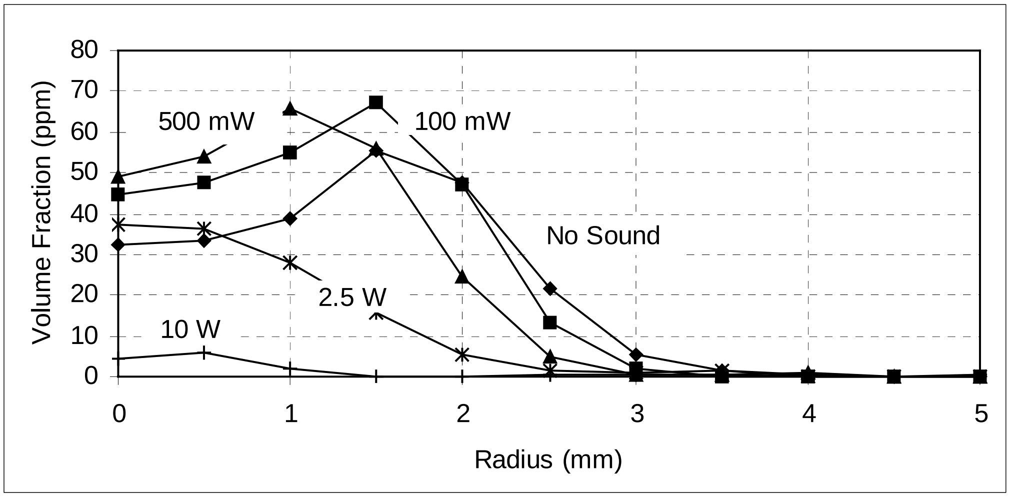

Figure 8.11. Soot volume fraction profiles at 12 mm elevation above burner face at selected sound power levels.

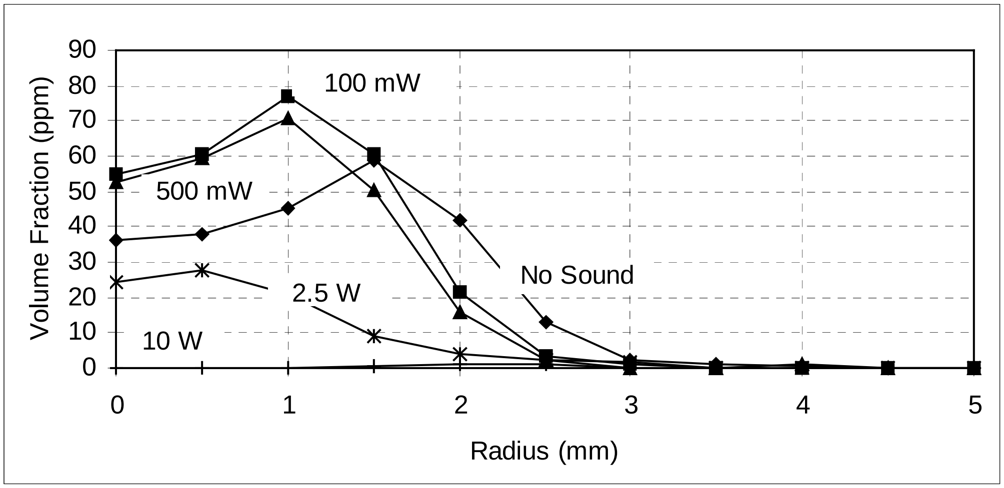

Figure 8.12. Soot volume fraction profiles at 14 mm elevation above burner face at selected sound power levels.

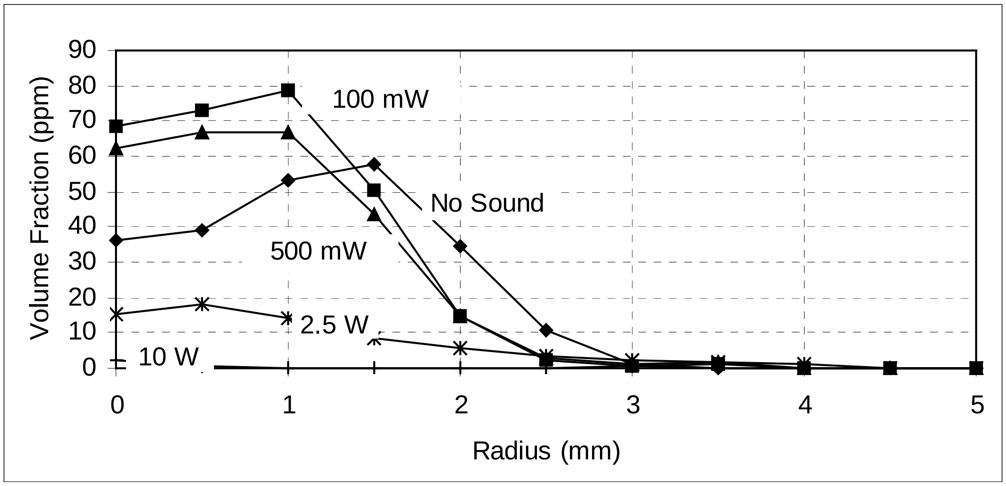

Figure 8.13. Soot volume fraction profiles at 16 mm elevation above burner face at selected sound power levels.

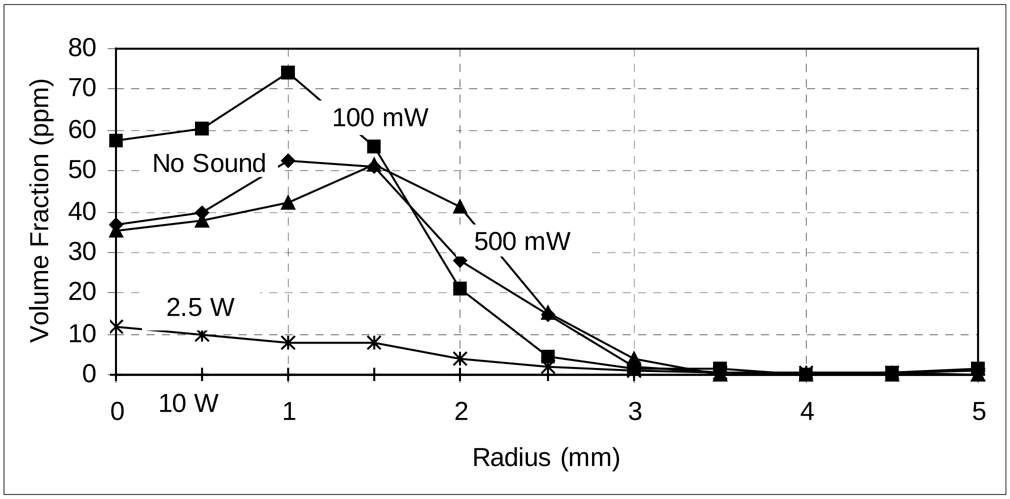

Figure 8.14. Soot volume fraction profiles at 18 mm elevation above burner face at selected sound power levels.

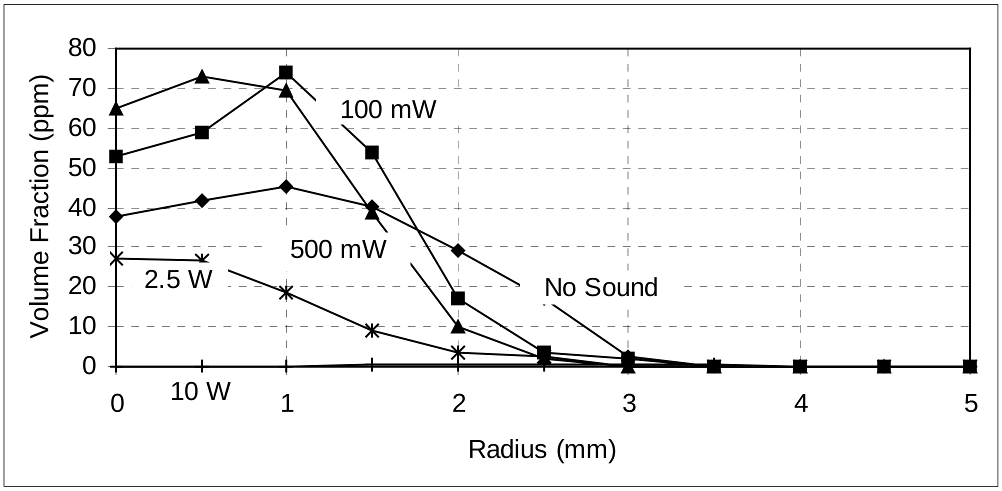

Figure 8.15. Soot volume fraction profiles at 20 mm elevation above burner face at selected sound power levels.

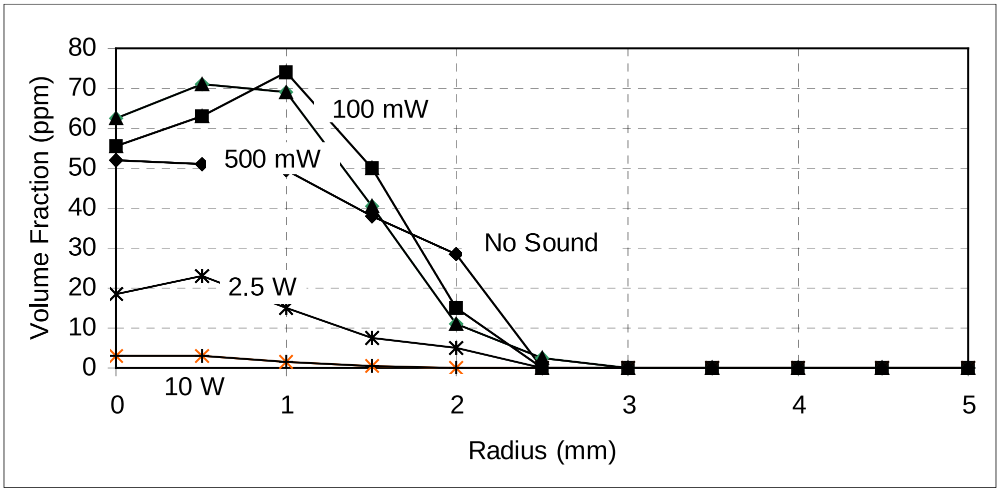

Figure 8.16. Soot volume fraction profiles at 22 mm elevation above burner face at selected sound power levels.

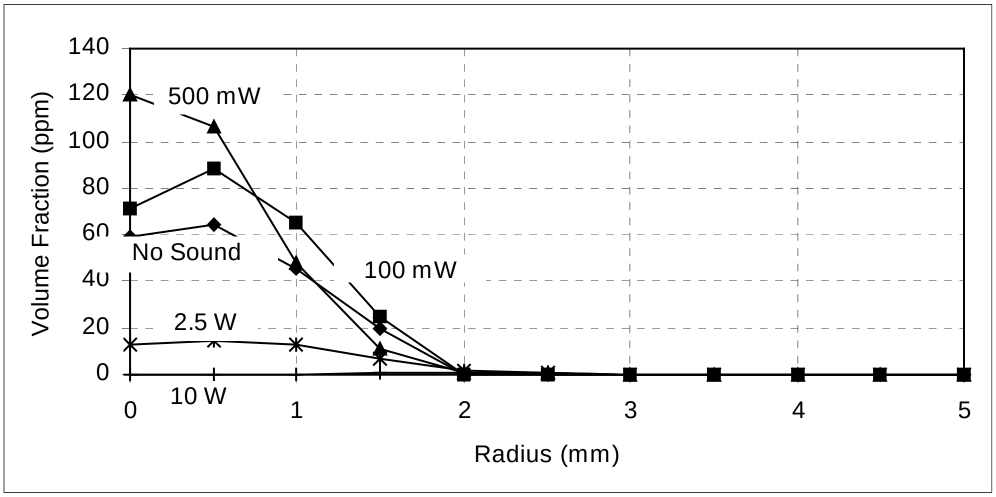

Figure 8.17. Soot volume fraction profiles at 30 mm elevation above burner face at selected sound power levels.

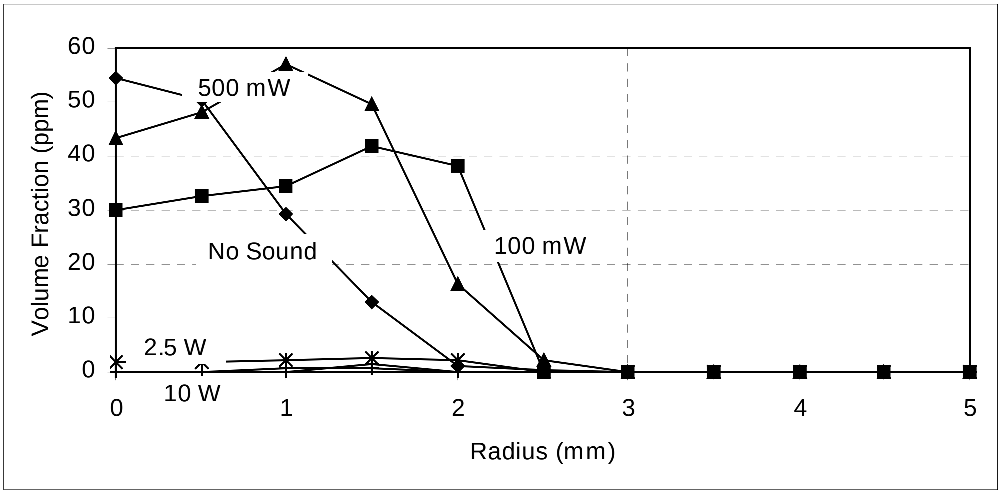

Figure 8.18. Soot volume fraction profiles at 70 mm elevation above burner face at selected sound power levels.

Overall inspection of the effect of acoustic forcing can be done by numerically integrating the soot volume over the entire flame area at any one height, and then dividing by a constant cross-sectional area. In order to compare the total amounts of soot uniformly at different heights (with different exact flame diameters), the flame area was simply defined as a cylinder of radius 5 mm. This is graphed in figure 8.19.

There is little to no change in the soot average soot volume fraction at any one height at powers below 0.4 W. At higher powers, the integrated volume fraction drops off, until it levels out at approximately zero at 6 W.

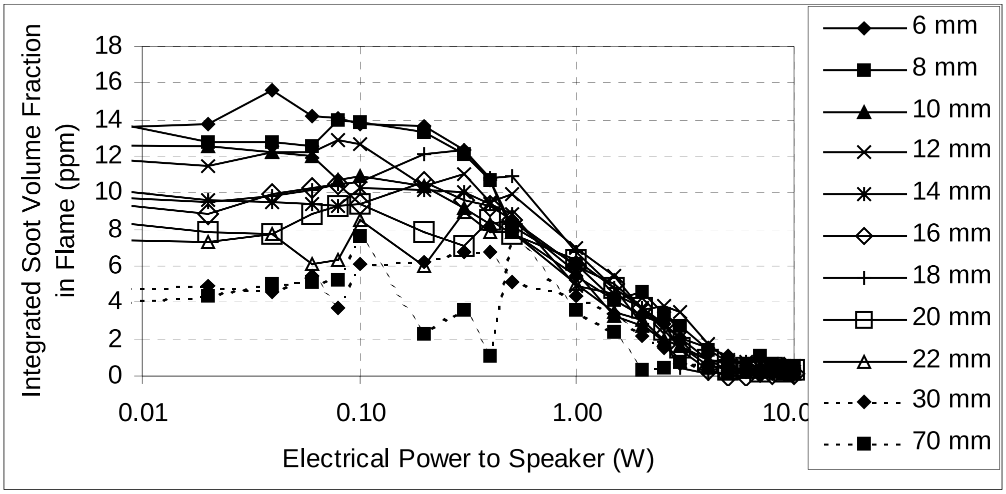

Figure 8.19. Integrated Soot Volume Fraction for Different Acoustic Powers.

9 PARTIALLY PREMIXED FLAMES

In chapter 3, it was stated that the two methods known for suppressing soot in diffusion flames are applying strain to the flame and partially premixing the flame. In this chapter, data on the spectrum of radiant emissions and the volume fraction of soot in the flame are compared for the partially premixed and acoustically forced flames. The similarities between the flames as shown in these measurements lead to the conclusion that the acoustic driving premixes air into the flame.

To test the hypothesis that partial premixing is the primary driver of the effects observed in the flame, air was metered into the fuel flow to produce equivalence ratios from infinity (the baseline non-premixed flame) to 3. The equivalence ratio is the ratio of the fuel/air ratio in the actual case to the fuel/air ratio for stoichiometric combustion. Mathematically,

$$\phi = \frac{\left.\dfrac{\dot{m}_{fuel}}{\dot{m}_{air}}\right|_{actual}}{\left.\dfrac{\dot{m}_{fuel}}{\dot{m}_{air}}\right|_{stoichiometric}} \qquad \text{eq. 9.1}$$

The stoichiometric fuel/air ratio for acetylene is 0.075, which comes from the stoichiometric chemical equation for acetylene combustion with air:

$$C_2H_2 + 2.5\,(O_2 + 3.78\,N_2) \rightarrow 2\,CO_2 + H_2O + 9.45\,N_2$$

Note from eq. 9.1that the purely nonpremixed case, where the air flow rate is zero, corresponds to an equivalence ratio of infinity, while an equivalence ratio of 1 signifies stoichiometric combustion. Equivalence ratios below three led to flashback problems, i.e. the flame would propagate into the fuel tube and extinguish against the flashback arrestor. The premixing was done in all cases with the flow rate of fuel, rather than the velocity of the fuel/air center jet, held constant. This means that the fuel/air flow and the air co-flow were not velocity matched, and there was a shear layer near the flame zone. No flame changes due to flow instabilities were observed during the experiment.

The partial premixing experiments were done by metering air into the fuel line well upstream (about 1 meter, over 100 tube diameters) from the flame. This, and the torturous flow path that the flow must take through a combined check valve and flashback arrestor in the fuel line about 230 mm upstream from the fuel line outlet, assure that the air and fuel are intimately mixed.

The actual flow rates of the air for the premixing experiments are given in Table 9.1. The actual fuel flow rate is 88 mL/min.

Equivalence Ratio, ϕ	Air Flow Rate (mL/min)
∞	0.0
50	20.6
20	51.5
10	103.0
5	206.0
3	343.4

Table 9.1. Air flow rate versus equivalence ratio for partial premixing experiments

9.1 Spectroscopy of Premixed flames

The pattern of increasing and then decreasing soot shown in figure 6.2and 8.19 is reminiscent of the findings of workers in partially premixed flames, such as Chakraborty and Long (1968), Mitrovic and Lee (1998), and Hura and

Glassman (1988). In their studies, the amount of soot produced by a flame increases with small amounts of partial premixing, then drops off with further addition of air to the fuel flow.

Figures 9.1 to 9.4 show the spectra at various equivalence ratios (ϕ). The emission curves are adjusted for short wavelength absorption and variable spectral emissivity as discussed in chapter 7. The data tend to lie quite well on the emission curves for all equivalence ratios tested. As in chapter 7, there are 256 wavelength points on the chart. Each point represents the average of 3 separate measurements. The repeatability of the measurement at each point is within 3%.

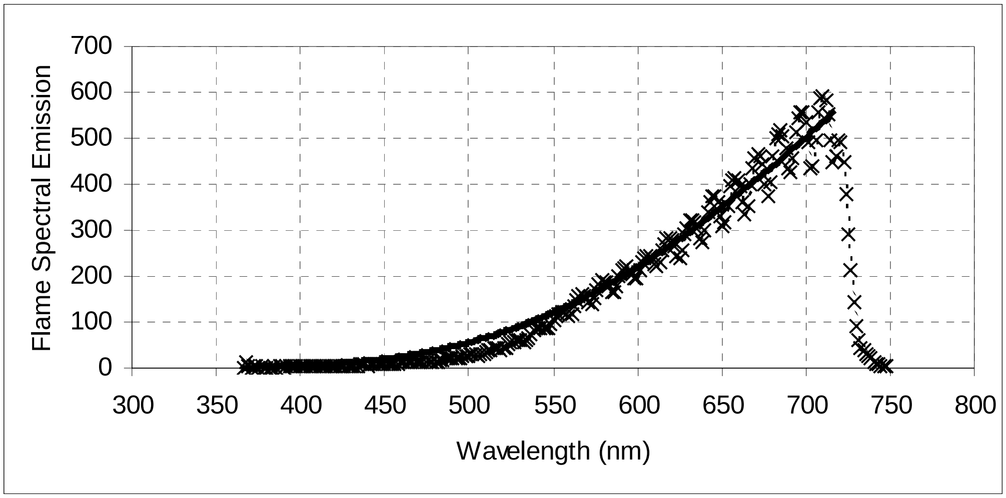

Figure 9.1. Spectral output of flame with partial premixing. $\phi = 50$. Solid line is emission curve including variable emissivity, with temperature 1932 K.

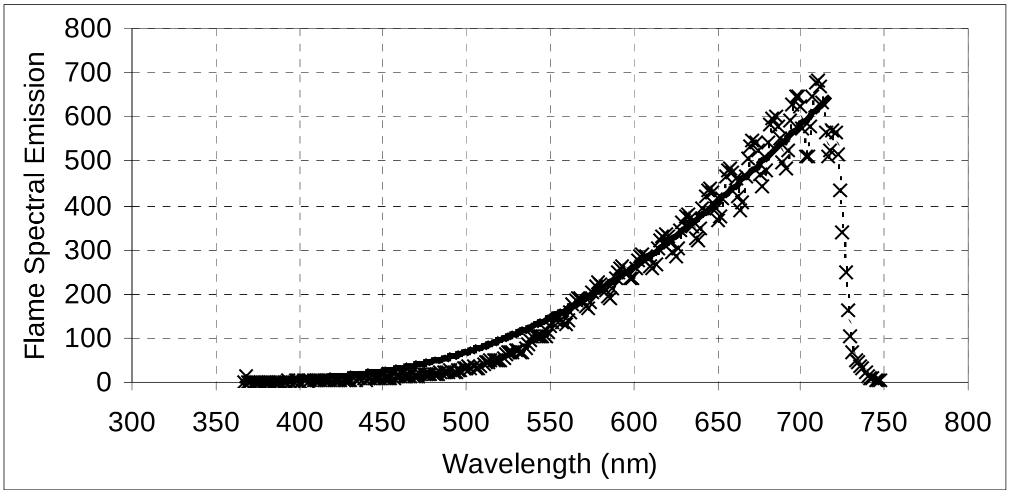

Figure 9.2. Spectral output of flame with partial premixing. $\phi = 10$. Solid line is emission curve including variable emissivity, with temperature 1955 K.

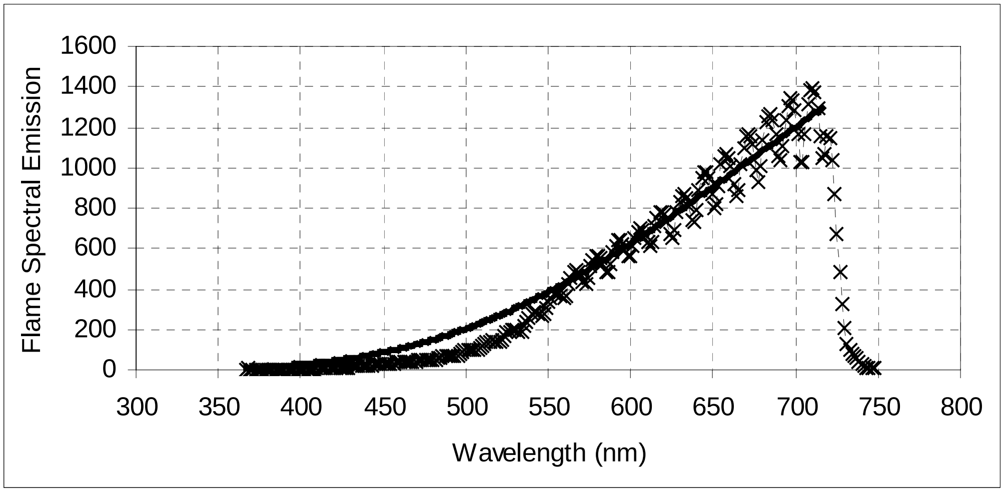

Figure 9.3. Spectral output of flame with partial premixing. $\phi = 4$. Solid line is emission curve including variable emissivity, with temperature 2118 K.

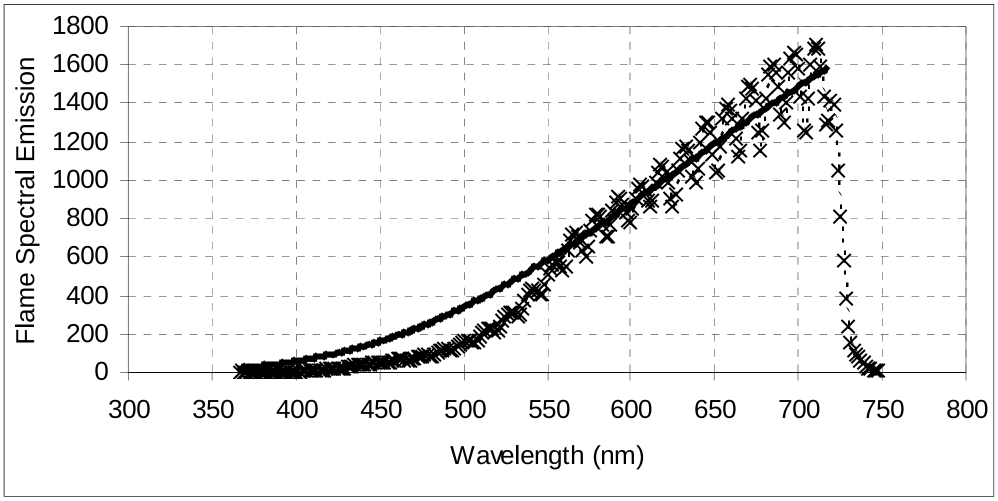

Figure 9.4. Spectral output of flame with partial premixing. $\phi = 3$. Solid line is emission curve including variable emissivity, with temperature 2265 K.

Figure 9.5 shows the temperature versus equivalence ratio for the partially premixed flames. The peak temperature for the curve fits, 2265 K, is at the minimum equivalence ratio (most premixing). The dotted lines and open symbols on the graph are for lower equivalence ratios than could be tested in the experiment. They are adiabatic flame temperatures computed using CET89. The similarity to figure 7.12 is very striking.

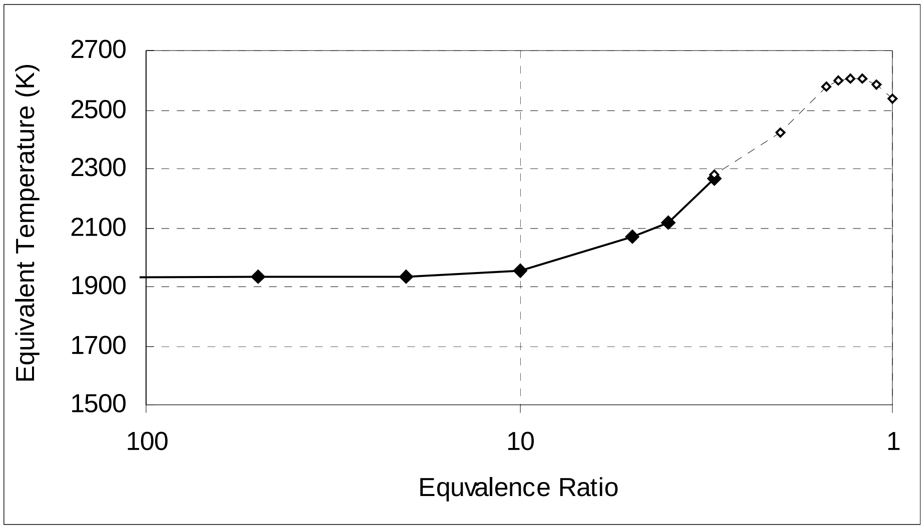

Figure 9.5. Radiation temperature versus equivalence ratio of partially premixed flames. The solid line and markers are the data from the curve fits. The dotted line and open symbols are computed adiabatic flame temperatures for acetylene-air premixed flames.

Figure 9.6 shows the combined data of figures 7.12 and 9.5, with the temperature on the X-axis and the sound power and equivalence ratios on the Y-axes. The match is quite good, and strongly supports the case that premixing is the driving force behind acoustic modifications to the sooting flame.

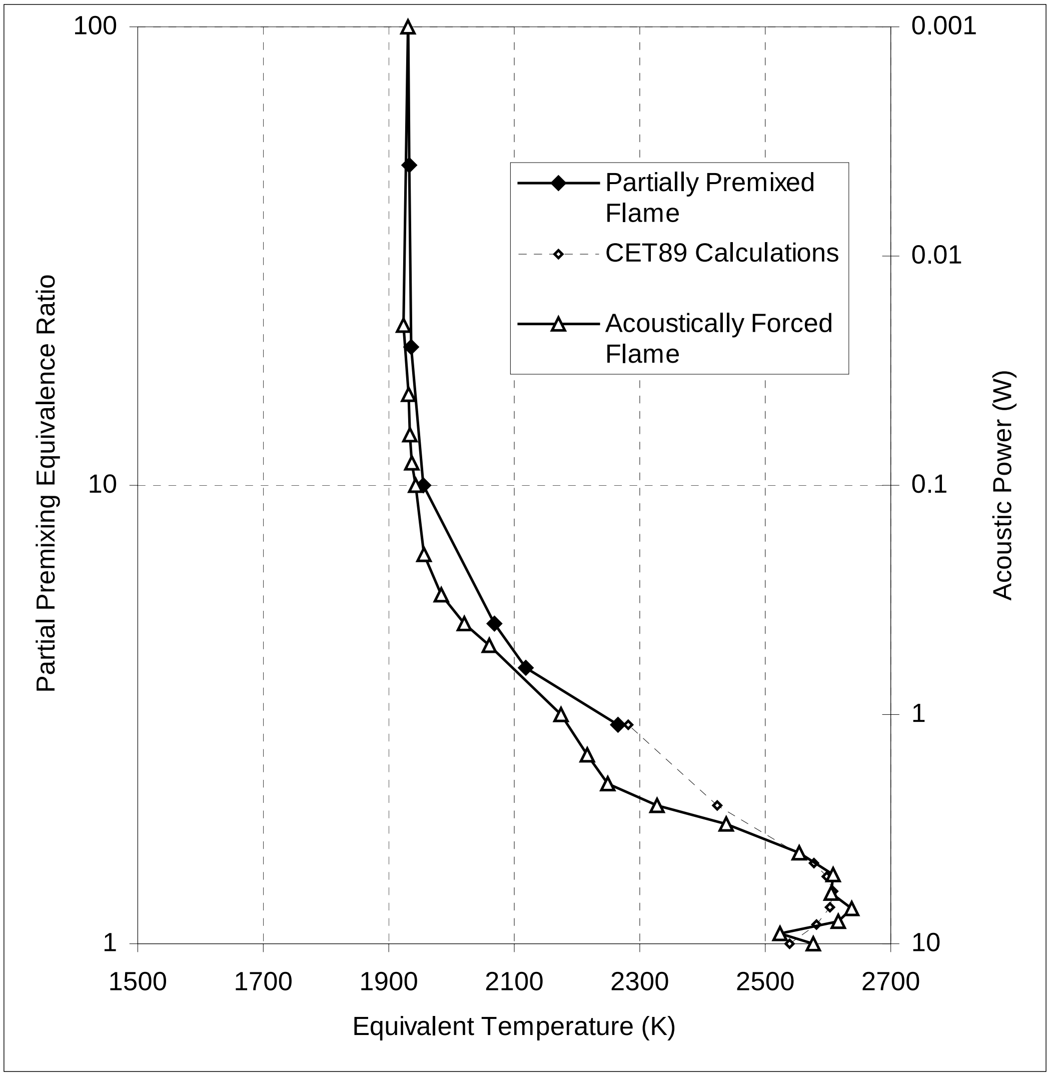

Figure 9.6. Comparison of acoustic forcing and partial premixing based on radiant flame temperature.

9.2 In-Flame Soot Profiles in Partially Premixed Flames

The methods of chapter 8 for reconstructing soot volume fractions from extinction data were applied to the partially premixed flames. This data is shown in figures 9.7 through 9.17. Premixing does not have as strong an effect on the flame shape as does acoustic excitation. The points of peak soot concentration generally do not move inward with decreasing equivalence ratio as they do with increasing sound power. However, the effects of premixing and acoustic driving on soot volume fraction are fairly similar. At high equivalence ratios (limited premixing) and high elevations, the soot volume fraction increases slightly. At low elevations, the volume fraction is little changed with limited premixing. At lower equivalence ratios, the volume fraction decreases. Only at 30 and 70 mm elevations did the ϕ=3 volume fraction curves approach zero.

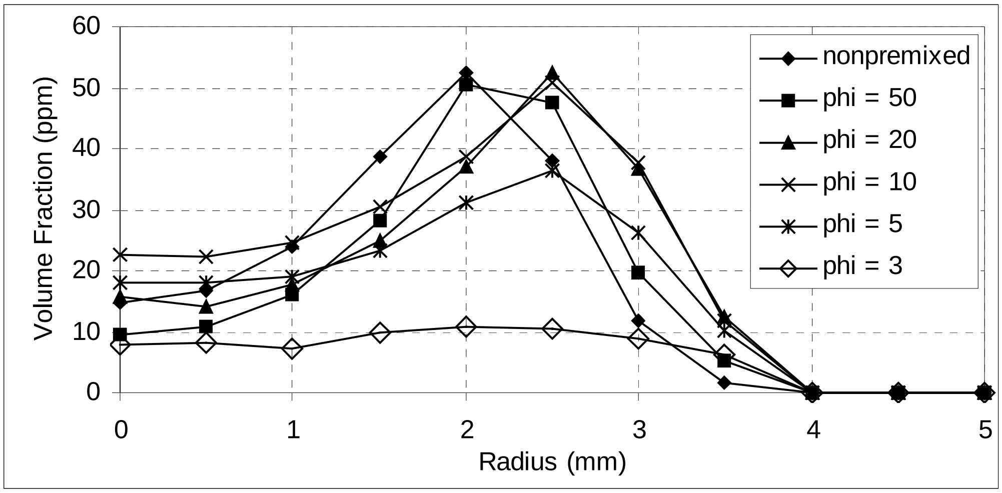

Figure 9.7. Soot volume fraction profiles at 6 mm elevation with varying equivalence ratios.

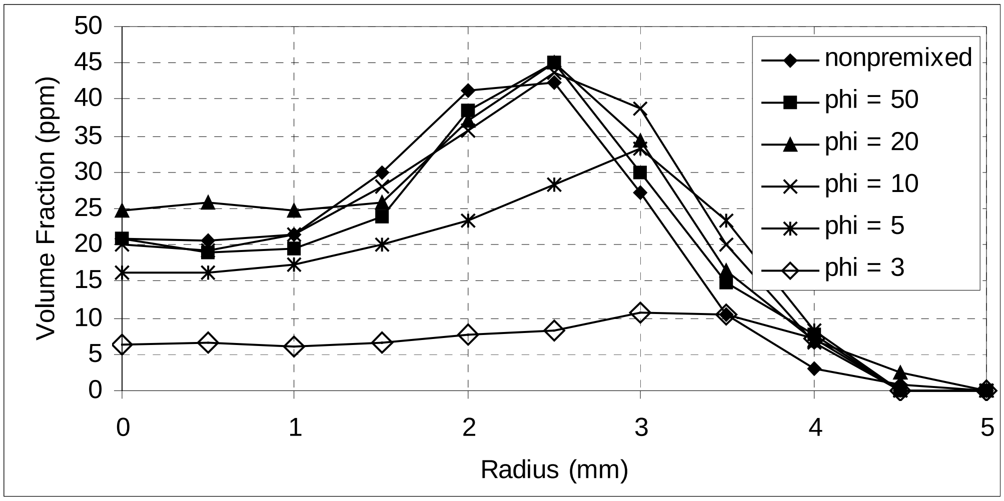

Figure 9.8. Soot volume fraction profiles at 8 mm elevation with varying equivalence ratios.

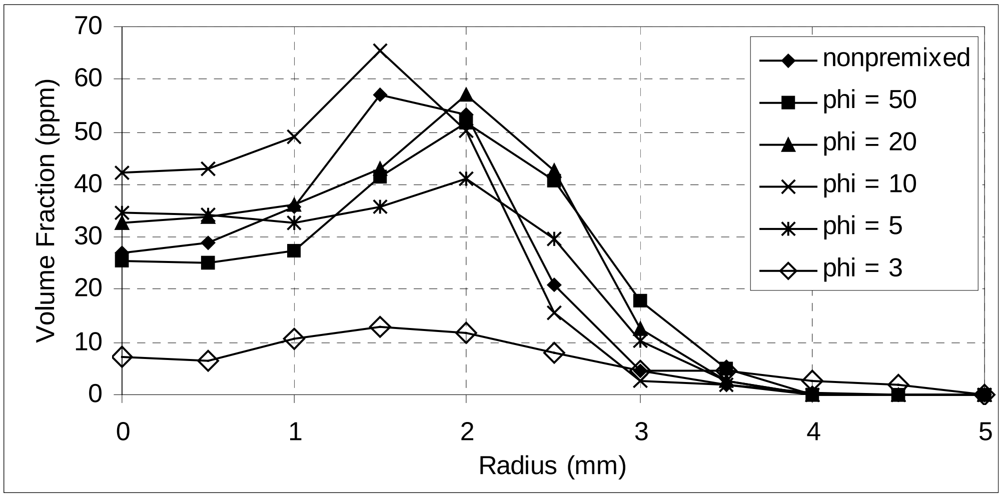

Figure 9.9. Soot volume fraction profiles at 10 mm elevation with varying equivalence ratios.

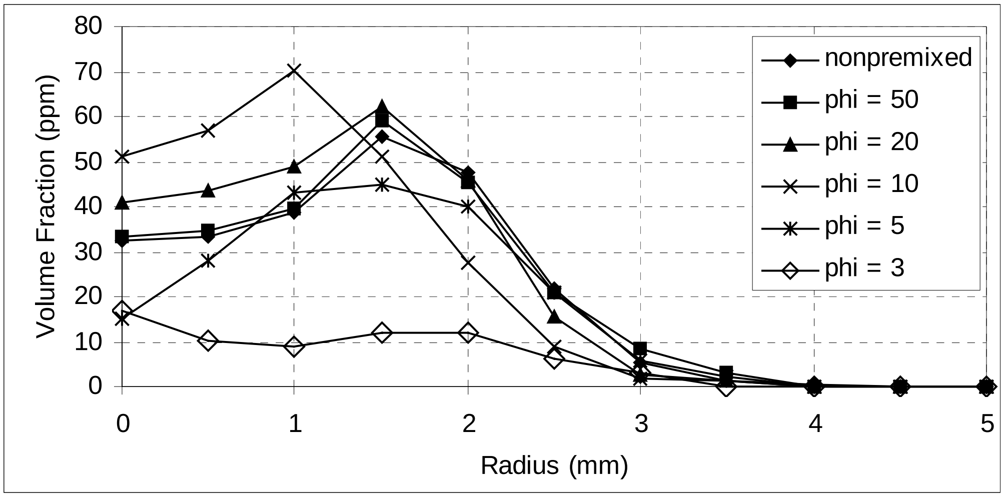

Figure 9.10. Soot volume fraction profiles at 12 mm elevation with varying equivalence ratios.

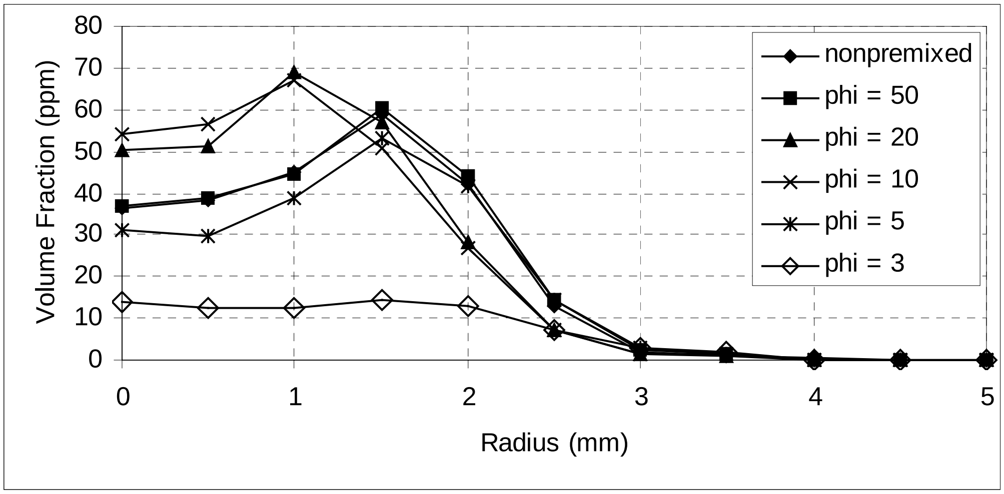

Figure 9.11. Soot volume fraction profiles at 14 mm elevation with varying equivalence ratios.

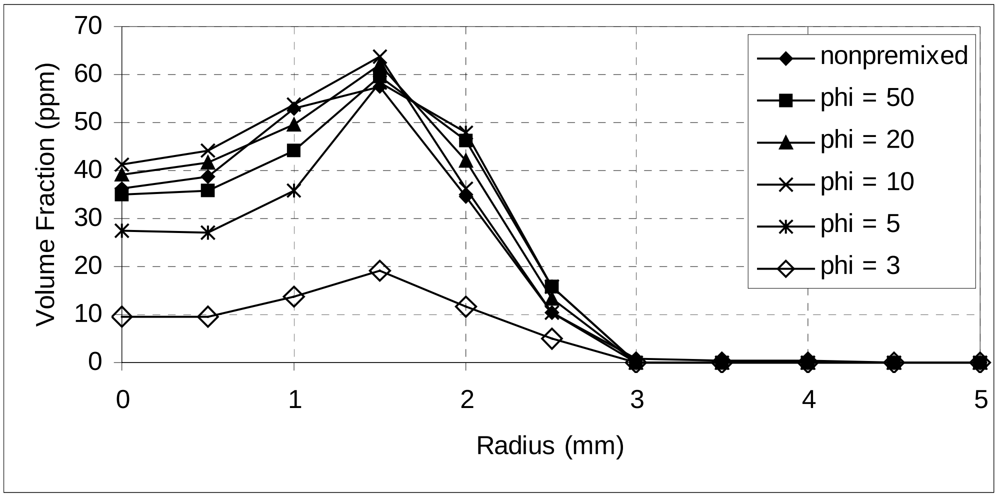

Figure 9.12. Soot volume fraction profiles at 16 mm elevation with varying equivalence ratios.

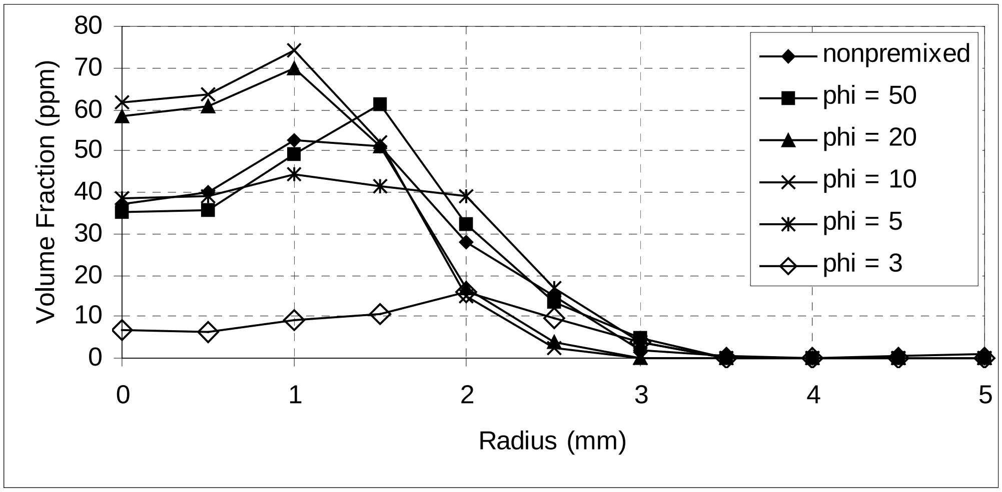

Figure 9.13. Soot volume fraction profiles at 18 mm elevation with varying equivalence ratios.

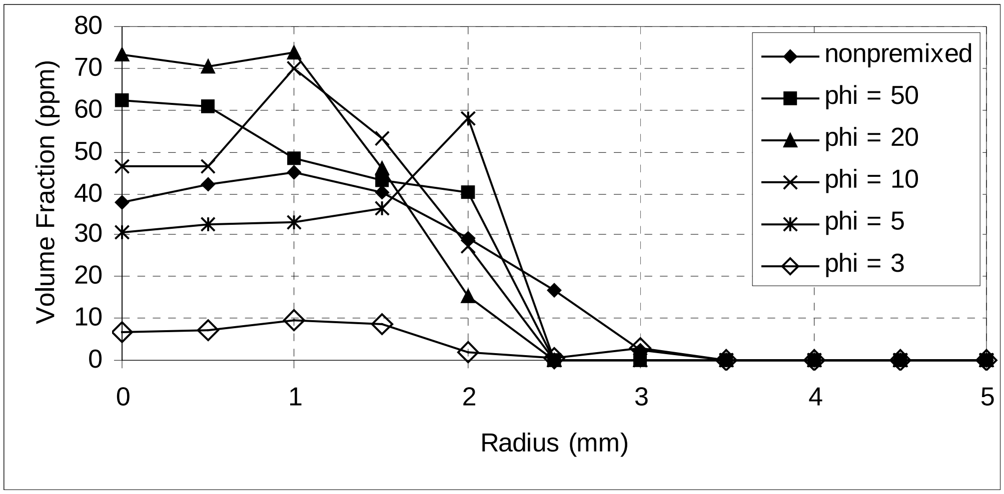

Figure 9.14. Soot volume fraction profiles at 20 mm elevation with varying equivalence ratios.

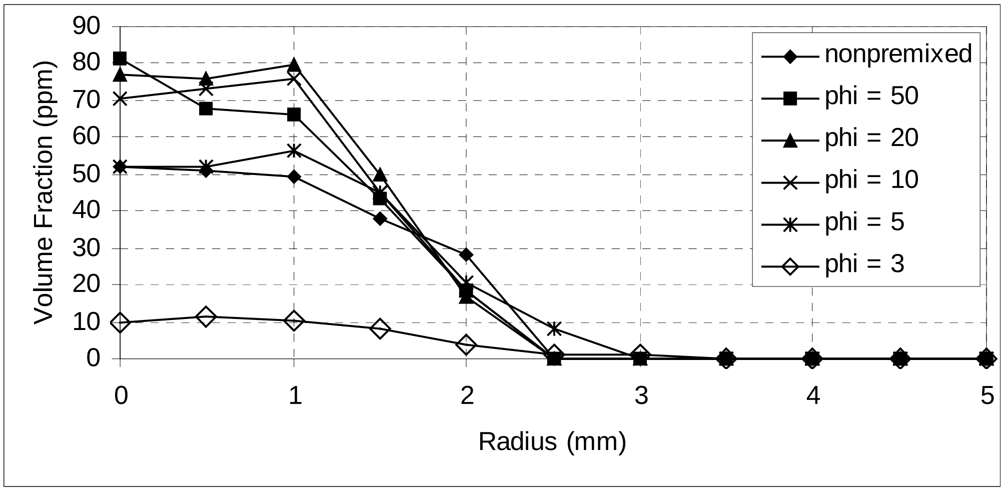

Figure 9.15. Soot volume fraction profiles at 22 mm elevation with varying equivalence ratios.

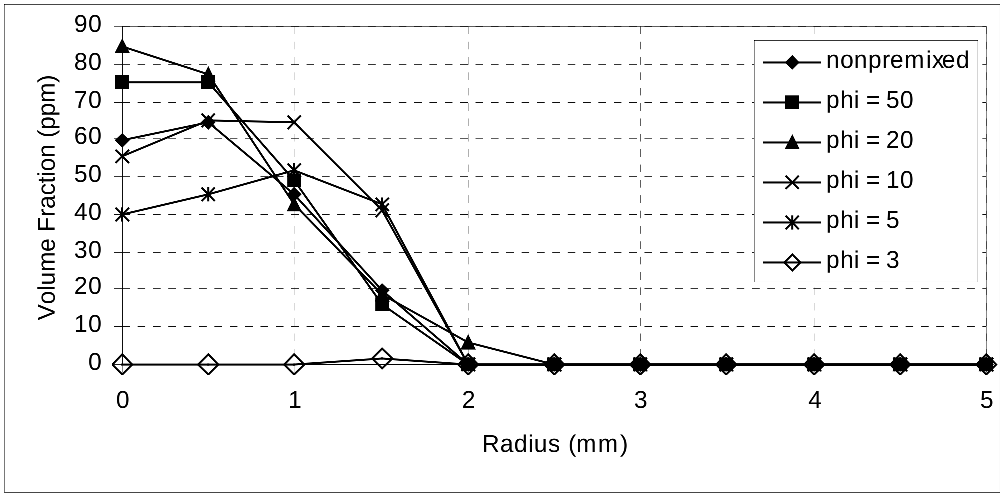

Figure 9.16. Soot volume fraction profiles at 30 mm elevation with varying equivalence ratios.

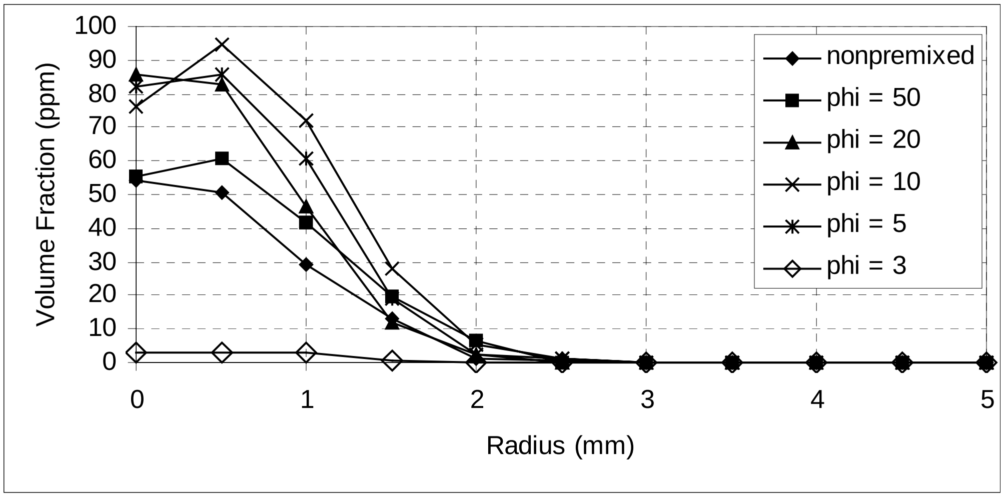

Figure 9.17. Soot volume fraction profiles at 70 mm elevation with varying equivalence ratios.

9.3 Integrated Soot Volume Fractions and Comparisons with Acoustic Cases

It is easier to examine the overall effects of premixing and compare them to acoustic driving by integrating the curves above over area and showing the average soot volume fraction as a function of height and equivalence ratio. That is done figure 9.18. The volume fraction exhibits limited change for equivalence ratios as low as ten. At 5, and more so at 3, the equivalence ratios diminish at all heights. The general shape of the f_v - ϕ curves do not change too strongly at all heights; only the height of the curve changes.

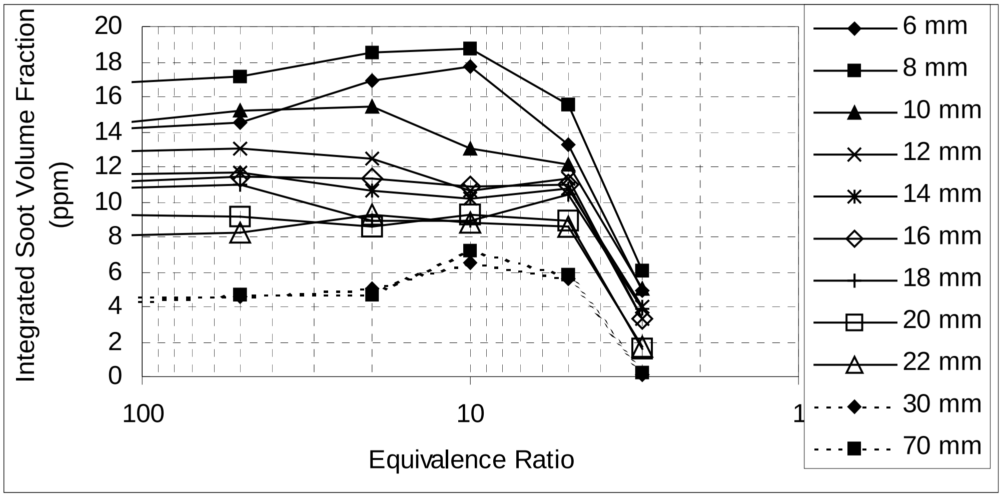

Figure 9.18. Soot volume fractions integrated over cross-sectional area versus height and equivalence ratio.

To ease comparison between the premixed and acoustically forced cases based on soot volume fraction, the soot profiles were integrated again to give an average volume fraction throughout the entire flame as a function of either equivalence ratio or sound power. The average volume fractions are plotted in figure 9.19.

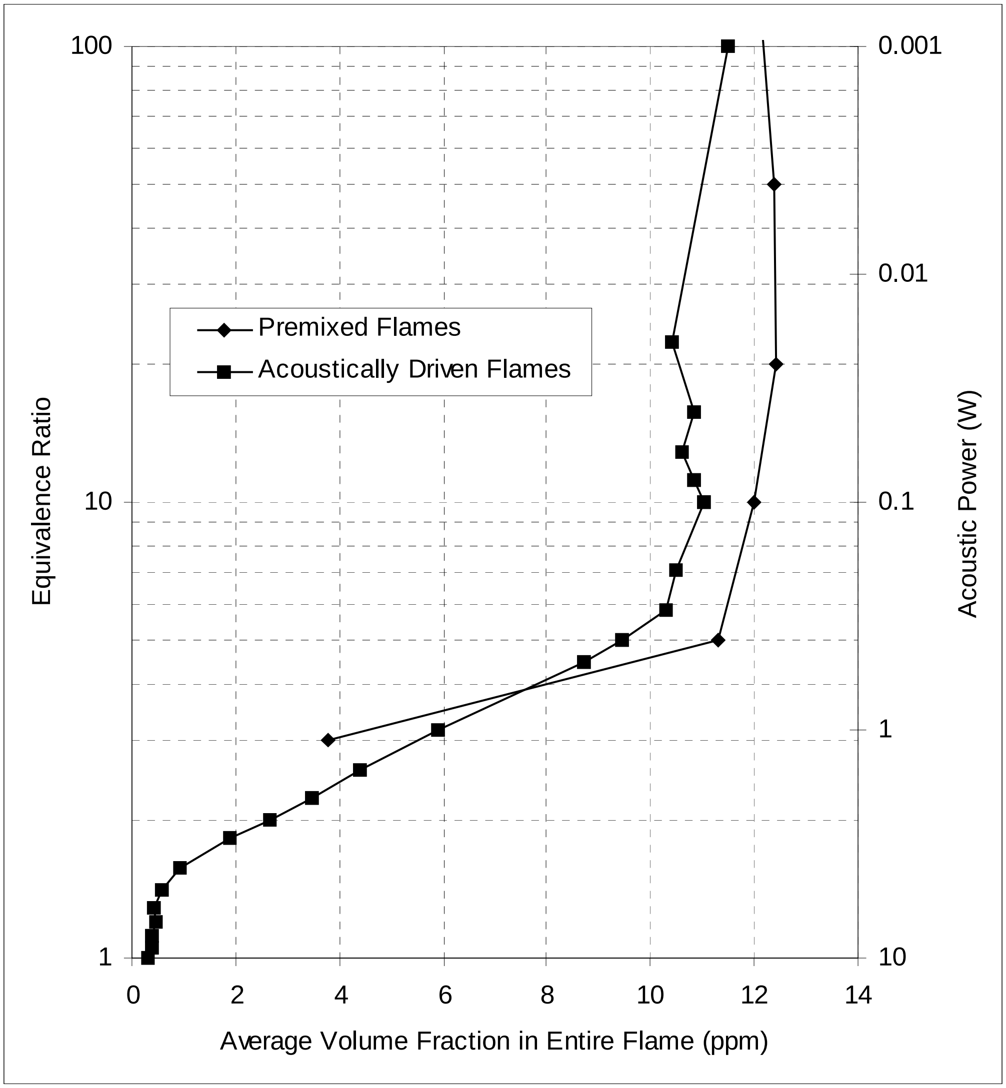

Figure 9.19. Global average soot volume fractions (integrated over area and height) in acoustically driven and premixed flames.

A simple reading of figure 9.6 and 9.19 indicates that the primary action of acoustic forcing is to premix air into the flame. In fact, for this particular setup, the equivalence ratio due to 940 Hz acoustic driving can be found from the simple relation:

$$\phi = \sqrt{\frac{10}{W}} \qquad \text{Eq. 9.2}$$

It is this premixing that drives the decreases in soot seen in chapters 6 and 8, and the increases in temperature seen in chapter 7. The increased temperature would also explain the increased emissions of nitrogen oxide from chapter 6. Acoustic forcing does have other effects, such as the alterations of flame shape seen in chapter 5. It is possible that the fluid mechanical effects illustrated by those altered flame shapes are responsible for the differences in the acoustically driven and partially premixed soot profiles shown in figure 9.19. However, the dominant effect of acoustic forcing is to cause premixing of the fuel and air in a gaseous flame just before the flame region.

9.4 Discussion of Premixing Mechanisms

Having established that acoustic driving causes premixing, the remaining question is how the acoustics lead to premixing of the flame. Although a comprehensive experimental investigation is beyond the scope of this work, a review of pertinent literature and a reconsideration of earlier results offers some guidance.

There are two likely methods of mixing in the system. The first is suction of air into the fuel tube as part of the phenomenon known as a synthetic jet. The second is mixing due to vortices created by acoustic streaming in the flame zone, outside the fuel tube. Each will be discussed below.

9.4.1 Synthetic Jets

Synthetic jet flows are jet flows with no net mass flux, produced by an oscillating velocity through an orifice, rather than a constant flow of material through an orifice. They were first noted by acoustics researchers examining the acoustic impedance of orifices (Bolt et al., 1949; Ingård and Labate, 1950; Thurston and Charles E. Martin, 1953; Ingård and Ising, 1967). Later they were used by acoustics researchers investigating high velocity streaming flows (Mednikov and Novitskii, 1975; Lebedeva, 1980). Recently, researchers in aerospace engineering have examined synthetic jets as ways of changing the apparent flow boundary of surfaces (Coe et al., 1995; James and Jacobs, 1996; Smith and Glezer, 1998; Rizzetta et al., 1999; Bailo et al., 2000).

Synthetic jets can be understood by imagining a tube with a diaphragm on one end and the other end open to a large space, as pictured in figure 9.20. When the diaphragm pulls in, the tube end acts as a point sink, and fluid enters the tube uniformly from all angles. When the diaphragm pushes fluid out, the behavior of the outflow from the tube varies according to the Reynolds number of the flow. In Stokes flow ($Re < 0.1$), the outflow and inflow are identical, and the tube exit acts as a point source. However, as the Reynolds number increases (momentum becomes more important) the edge of the exiting flow separates from the end of the tube and forms a toroidal vortex, which convects in the jet direction. The core of the exiting jet goes straight out of the tube with limited diffusive spreading. As the diaphragm oscillates, the process simply repeats. Rizzetta *et al*. (1999) show that the time average of the flow driven by the oscillating process is an outflow through the core of the tube and an inflow around the edges.

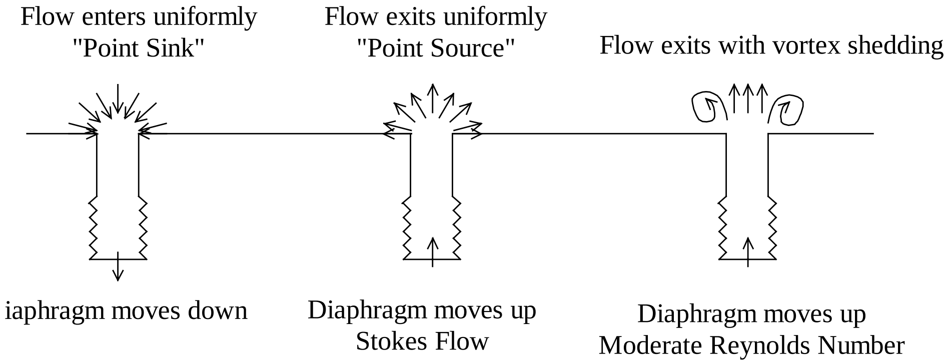

Figure 9.20. Schematic of a Synthetic Jet

Lebedeva (1980) performed a streaming experiment in an apparatus that is fairly similar to the apparatus of this work. The apparatus is shown in figure 9.21. A high intensity acoustic source is placed at one end of a tube 926 mm long and 23.5 mm in diameter. At the other end, an orifice is fixed with an inside diameter of 7.5 mm and a length of 2 mm. Beyond the orifice is placed a rigidly terminated tube whose length varies with frequency so that it is always one quarter wavelength long. This is done to produce a velocity maximum at the orifice. The system was driven at a 147 dB sound pressure level (velocity amplitude 1.2 m/s) in the tube, at frequencies of 500 and 1600 Hz. Due to constriction of the flow, the velocity of the first order oscillation in the orifice was quite high, 17.8 m/s. Streaming velocities as high as 10 m/s were observed a short distance from the outlet. Lebedeva also notes that reverse flows (into the orifice) were observed at the edges of the orifice, balancing the strong outward flow in the center, a pattern also observed in Rizzetta *et al.*'s (1999) numerical simulations. By varying the intensity of the driving, the streaming velocities were shown to be proportional to the acoustic driving velocity, a result also found by Ingård and Labate (1950) and Mednikov and Novitskii (1975).

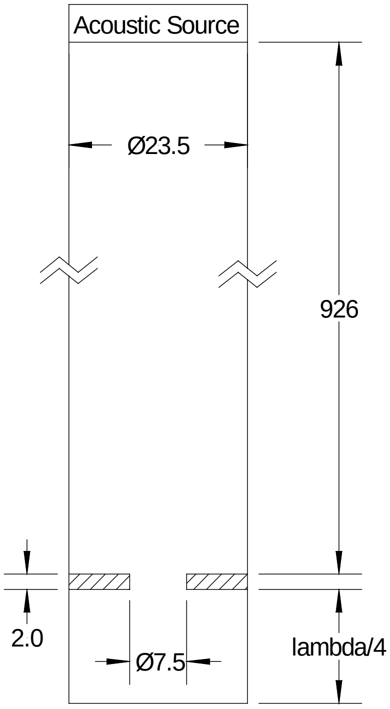

Figure 9.21. Streaming Apparatus of Lebedeva (1980).
All dimensions in millimeters.

Comparing Lebedeva's experiment with this research, many similarities are seen. The geometry is quite similar, with the acoustic driver at the far end of a large tube. Lebedeva's tube is about one third the diameter of the flame zone and exhaust stack in this work, but his orifice is just under twice the diameter of the fuel tube. In section 5.2, the velocity of the burning fuel slugs was shown to be proportional to the driving velocity, with a magnitude between 1 and 10 m/s. That behavior is quite similar to that observed by Lebedeva. The "orifice" in the current work is one-sided, being the end of the fuel tube, rather than an actual orifice, but there is certainly a sharp enough edge to produce flow separation in the direction of the fuel flow. The orifice in the current work is a screened bead layer, not a rigid termination, but the reflection coefficient is near to 1 (a rigid termination would give a reflection coefficient of 1) as shown in figure 4.5. Another similarity is in the edge flow. Just as was noted by Lebedeva and Rizetta *et al.*, soot particles in the current experiment have been observed being drawn radially inward along the face of the steel screen on top of the burner and into the fuel tube.

Another indication that there is a synthetic jet operating in the current setup comes from Thurston and Martin (1953). They show several photos of the flow from an orifice being driven by a piston oscillating at 10 Hz. The photos show a similar pulsed flow structure to that shown in the flame pictures of figures 5.3 and 5.4.

It is also important to note that the average Reynolds number of the cold fuel flow is 45, which is high enough to drive periodic flow structures (Panton, 1984, chapter 15). The elevated temperatures due to the flame will increase the viscosity and decrease the Reynolds number somewhat. Bird, Stewart, and Lightfoot (2001) show that the viscosity of a low density gas well above its critical temperature will increase as temperature to roughly the 0.6 power. The temperature at the fuel tube exit is uncertain, but even were it 2600 K, the maximum temperature for a near-stoichiometric acetylene-air flame predicted by the chemical equilibrium code, (figure 9.6), the viscosity would only increase by a factor of 3.7 from its cold value. This gives a Reynolds number of 12 for the unforced flow, which is sufficiently high to generate at least limited momentum effects in some cases. A steady cross flow over a cylinder at Reynolds numbers from 4 to 40 generates standing vortices on the back of the cylinder (Panton, 1984).

One point differentiating the current apparatus from many synthetic jet experiments is that there is no designed-in resonant cavity in the current apparatus.

9.4.2 Vortices outside the fuel jet: Rayleigh Streaming

While synthetic jet flows depend on the presence of an orifice to produce vortical flow structures, another mode of acoustic streaming that may drives one of the patterns seen in the experimental apparatus is driven by the presence of a high intensity standing wave inside the exhaust stack. The two-dimensional version of this problem, a standing wave propagating between two planar walls, was considered first by Lord Rayleigh(1945), and the result was corrected by Westervelt (1953) and also discussed in the review by Nyborg (1965). The cylindrical form of the problem, which is directly relevant to the current situation, was done analytically by Schuster and Matz (1940), and an English language discussion was written by Ilinskii (2001). Essentially, an acoustic wave in a closed cylinder attenuates in the viscous boundary layer near the cylinder wall. The momentum being carried by the wave must be conserved, so it is transferred to a DC flow of the fluid. This produces a series of counterrotating cells spaced every half-wavelength along the tube, as pictured in figure 9.22. Note that the solution graphed is only valid outside the acoustic boundary layer, the area near the wall where viscosity dominates. Mathematically, this is expressed as $R-r >> 1/\beta$, where R is the outer radius of the tube and $1/\beta$ is the boundary layer thickness, given by $\beta = \sqrt{\frac{\pi f}{\nu}}$. ν is the kinematic viscosity of the gas (mostly air) and f is the driving frequency. The acoustic boundary layer thickness for this work varies from 39 to 144 μm in cold flow in the 70 mm exhaust stack. With the flame burning, the viscosity of the fluid at the wall is uncertain, but as noted earlier it is no more than 3 times the cold flow level, which means that the boundary layer thickness increases by no more than 73% i.e. it is no more than 430 μm thick for the peak temperature and the lowest frequency (230 Hz). The Schuster and Matz solution is then valid across most of the tube with respect to the acoustic boundary layer thickness.

The flow patterns in Rayleigh streaming are very similar to the patterns observed in the 3100 Hz flame. This indicates that Rayleigh streaming drives the flow at 3100 Hz (in balance with buoyancy, as discussed in chapter 5). This is in spite of the fact that the calculated maximum velocity of the streaming flow at the peak velocity for 10 W, 3100 Hz is only 0.5 cm/s, much smaller than the cold flow velocity of the fuel and air (10 cm/s). Clearly, though, the velocity is sufficient to dominate the flow. This may be due to perturbations of the acoustic field driven by the elevated temperatures around the flame.

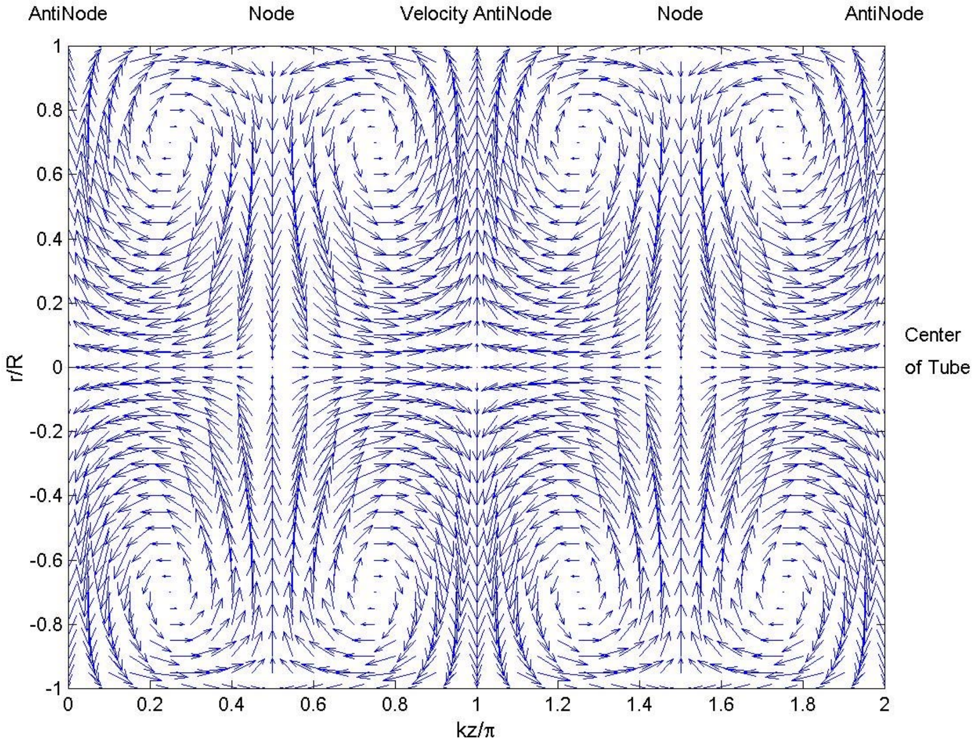

Figure 9.22. Diagram of streaming in a tube, based on Schuster and Matz (1940). The peak velocity is 5 mm/s at a frequency of 3100 Hz and first-order particle velocity of 1.5 m/s (from figure 4.4).

It may be significant that the 3100 Hz field is not necessarily composed of only plane waves. The exhaust tube is in cutoff (waves will not propagate well down its length) for all but plane waves in the 230 and 940 Hz cases. However, the cutoff frequency for the (1,1,0) mode (first angular mode) is 2871 Hz in the cylindrical exhaust stack (Blackstock, 2000). The driving applied by the horn driver is essentially axisymmetric, but there are non-axisymmetric features in the tube wall (particularly the tee where the exhaust exits the system) which may contribute to formation of an angular mode. No solution for this problem has been found in the literature. Other modes that are not in cutoff are all in the (1,1,N) family, where N denotes axial variations. No higher radial or angular modes are not in cutoff. The existence of angular modes in the exhaust stack admits the possibility of streaming flows moving angularly around the circumference of the stack, but that was not observed in the motion of soot in the glass-enclosed flame zone.

9.4.3 Comparison of Synthetic Jet and Rayleigh Streaming

Both synthetic jet flow and Rayleigh streaming produce some vortex flow, due either to separation from a lip, or to viscous attenuation at a wall. There are several important differences. In the case of Rayleigh streaming, the vortical flow is stationary relative to the wall. Its geometry is determined solely by the standing wave pattern, which is essentially determined by the geometry of the enclosure and the frequency of the acoustic source. This is consistent with the flame geometry seen in the 3100 Hz case. By contrast, the synthetic jet streaming produces structures that are not anchored to any solid body. As shown by Lebedeva (1980), Ingård and Labate (1950), and Mednikov and Novitskii (1975), the vortices convect away from the orifice generating them at velocities comparable to the acoustic driving velocity. This is consistent with the excess velocities seen in the 230 and 940 Hz cases, and the behavior of the structures seen in the high films that generated the photos in chapter 5.

Although it is generally possible that flow in the flame zone can produce sufficient mixing to suppress soot (Dubey et al., 1997), and can also produce strain rates that suppress soot (Du et al., 1988), little change in global soot output was observed in the 3100 Hz case. This indicates that Rayleigh streaming, while sufficient to modify the flame shape, is not adequate to drive substantial premixing or otherwise cause soot suppression. It is synthetic jet streaming, which causes air to flow into the fuel tube before expelling it with the fuel, that drives premixing in this study.

10 CONCLUSION

10.1 Summary

It has been shown that acoustic driving can strongly influence the flame shape, sooting tendencies, and radiant characteristics of a non-premixed acetylene flame over the range of conditions tested. At the appropriate frequency and intensity, the soot production of the normally heavily sooting flame can be almost completely suppressed, with soot emissions cut to almost zero. At other conditions, the soot (both number concentration and volume fraction) produced by the flame can be increased by 3 to 4 times, with a concurrent reduction in the particle diameter of 15 to 20%. There is some indication that the soot suppression effect scales with an acoustic Reynolds number, $U_{ac}^2/f\nu$.

When the flame is acoustically driven at frequencies below about 1000 Hz, high-speed flame pictures show that it develops a series of regular bulbous pulses, with very thin sections in between. At low frequencies, the thin sections can even be pinched off, turning the flame into a series of luminous slugs. Information on the spacing between the pulses can be used to determine the velocity with which the pulses travel. It was found that the magnitude of the acoustically induced velocity increases proportionally to the oscillating (first order) acoustic velocity. The luminous length of the flame can increase or decrease with increasing acoustic power, according to frequency. In some cases, it increases at low power, then decreases at higher powers.

Besides changing the soot emissions of the flame, acoustic driving affects other pollutant emissions as well. Nitrogen oxides generally increase with acoustic driving, probably due to an increase in the temperature of the flame. This is supported by spectrometer measurements on the radiant output of the flame. Carbon monoxide and unburnt hydrocarbons can increase or decrease with increasing power, depending on the frequency of the acoustic driving.

The total radiant emissions from the acoustically forced flame exhibit two conflicting tendencies. At moderate acoustic powers, the increased temperature of the flame leads to an increase in total radiant output. However, at higher powers, reduced flame height leads to reduced radiant area, and reduced radiant output. In spite of the reduced total radiant output, spectrometer measurements at visible wavelengths show that the temperature in the flame increases almost purely monotonically with increasing power.

Tomographic reconstruction techniques applied to an extinction measurement in the flame show that, at low powers, the concentration of soot in the flame increases with increased acoustic driving. This is true of the peak soot concentration, as well as the average concentration in the flame. However, at higher powers, the soot concentration drops off, and eventually goes to near zero.

A partially premixed flame was created by metering air into the fuel line far upstream from the flame. Stable flames with equivalence ratios as low as 3 could be achieved in this manner. The partially premixed flame was subjected to the spectrometry and in-flame extinction measurements, and the results compared to the results for the acoustically driven flame. It was found that the behavior of the flame at 940 Hz with increased acoustic driving power and that of the flame with increased premixing was quite similar. For this reason, it is concluded that acoustic pulsations serve to premix air into the fuel line of a diffusion flame.

The available data indicate that the premixing is caused by a synthetic jet flow between the fuel tube and the flame zone. It draws air from the sides of the stack into the fuel tube, where the air and fuel premix, then exit through the center of the tube. This pulsing flow causes the wrinkled shape of the flame and the increased flow velocity in the flame.

10.2 Discussion

Figures 10.1 to 10.4 presents a schematic of the premixing flow at 4 times in the acoustic cycle. The first is the point of maximum outflow from the nozzle. At that point, vortex roll up has begun on the sides of the exiting jet, mixing outside air into the exiting fluid. The center flow is fairly uniform. Well down in the tube, the flow is uniformly out of the tube. The velocity along the face of the burner, caused by the action of the toroidal vortex, is inward toward the center.

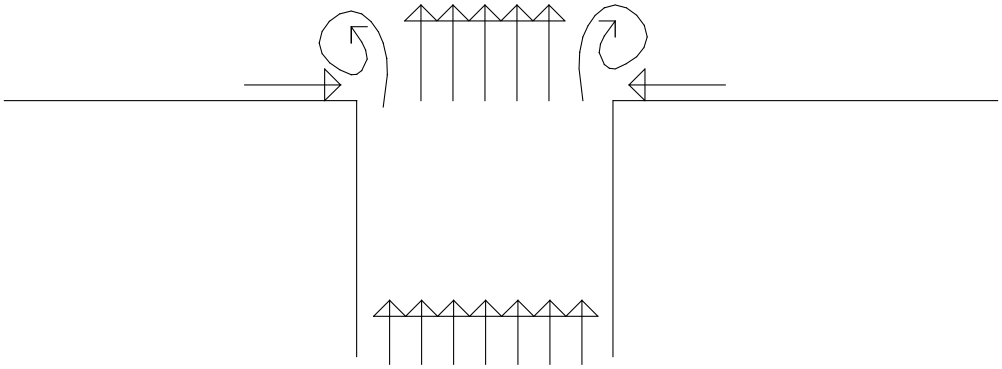

Figure 10.1. Schematic of synthetic jet premixing: Maximum outflow velocity. Vortex roll-up begins around the edges of the tube. Vortex drives inflow horizontally along burner face.

Figure 10.2 shows the flow at the zero velocity point after outflow, before inflow has started. The main jet and the toroidal vortex have moved away from the burner due to both advection during the outflow and self-propagation by the vortex. Some inward flow along the burner face continues.

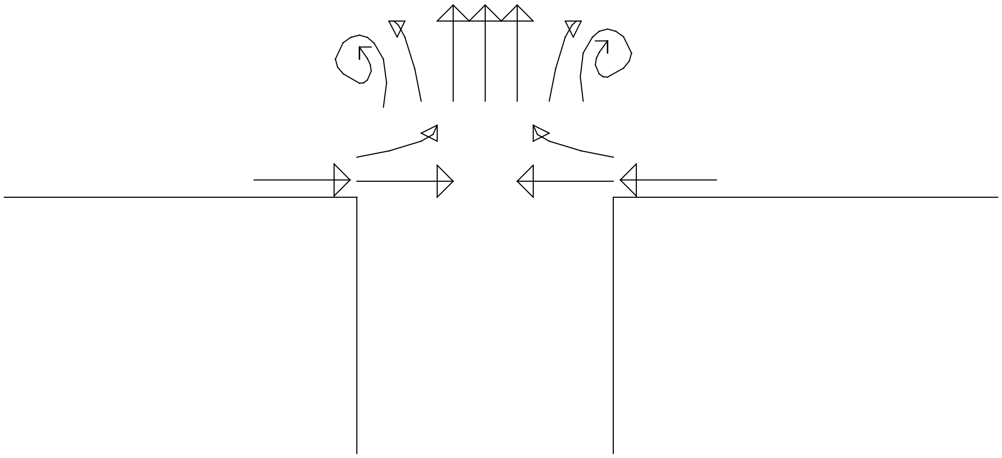

Figure 10.2. Schematic of synthetic jet premixing: Velocity zero after outflow. Vortices have moved away from the nozzle due to both advection and self propagation.

Figure 10.3 shows the situation during inflow. At this point, the vortex has moved far enough out that it is not sucked back into the nozzle, although its propagation will be slowed or halted momentarily. The radial inflow driven by the vortex along the burner face is now increased as air is sucked into the nozzle. This inflow does see an edge at the nozzle lip that may cause a separation vortex there, driving mixing of the new air from the surroundings with the fuel in the tube.

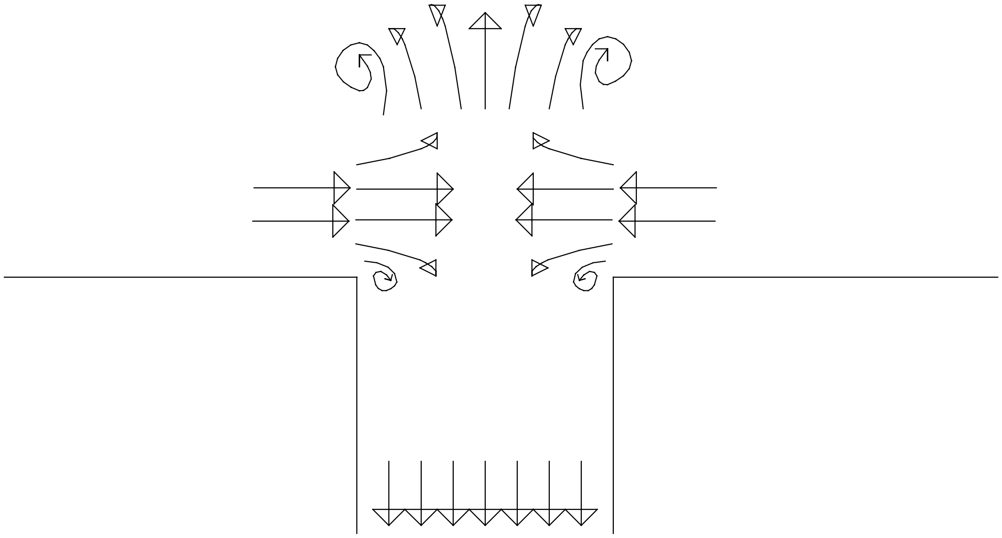

Figure 10.3. Schematic of synthetic jet mixing: Maximum inflow velocity. The vortex has moved far enough from the burner to not be sucked back into the nozzle. Air inflow is primarily radial.

Figure 10.4 shows the velocity zero after inflow. At this point, the vortex has propagated further from the nozzle, but it is also losing strength. (Smith and Glezer (1998) have shown experimentally that the vortex only survives for about 1 acoustic cycle before dissipating.) More importantly, the air and fuel continue to mix in the top of the fuel nozzle. When the next cycle occurs, the fuel issuing from the nozzle will already have air mixed into it, as required by the soot suppression observed in the core of the jet at even the lowest elevations (e.g. 6 mm in figure 8.8.

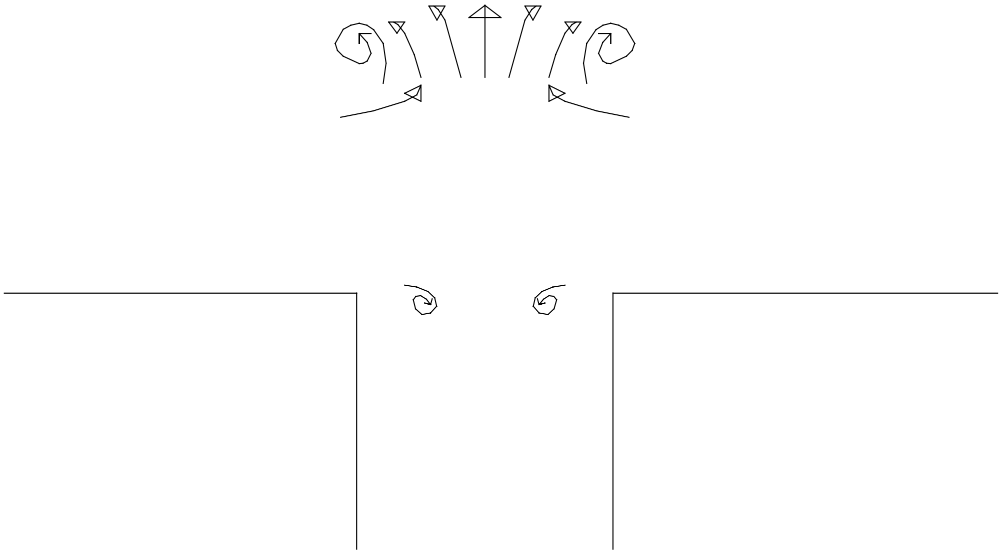

Figure 10.4. Synthetic jet mixing: Velocity zero after inflow. The toroidal vortex continues to propagate outward, but loses strength. Mixing occurs in the top of the tube.

It should be clear from this discussion that premixing by synthetic jets is a fluid mechanical effect. High intensity sound is not required to cause synthetic jet flows. An oscillating flow driven by some sort of valve (Parikh and Moffat, 1981) or plunger (Mednikov and Novitskii, 1975) arrangement , an acoustic driver attached to the fuel tube only (Lovett and Turns, 1990), and a piezoelectric driver disc with no nozzle, orifice, or cavity at all have all (Smith and Glezer, 1998) have all been used to produce synthetic jets. Any mechanism that provides at least some small cavity before the flame zone should produce the a similar level of premixing without the objectionable noise. A more focused method for driving the oscillations would also likely be far more efficient than the current method.

Effective acoustic driving as done in this work requires 1 to 5 watts, a significant fraction of the 75 watt flame power.

There are benefits to synthetic jet mixing, particularly for small, laminar flames. Comparing synthetic jet mixing to conventional premixing (the addition of air far upstream of the burn zone), the synthetic jet flow allows much nearer-stoichiometric operation. In this work, the conventionally premixed flame flashes back at equivalence ratios below 3, while the synthetic jet flame is stable to an equivalence ratio near 1. Put another way, the fuel flow rate of a conventionally premixed flame operating near stoichiometric conditions can only be turned down to a certain level, below which the flame will propagate up the fuel nozzle faster than the fuel/air mixture is moving. The synthetic jet flame is stable at much lower fuel flow rates. This is a flexibility that could be attractive in some situations.

Future work in this field should focus on developing a more detailed understanding of the velocity conditions that produce premixing. A key unanswered question is exactly what velocity conditions lead to synthetic jet flows without nozzle caking. In this study, frequencies from 200 to 300 Hz cause lobed structures, and the global soot measurements indicate the start of premixing, but the effect is less pronounced at any given power than at higher frequencies. This can be understood by considering that the low end of the nominal frequency range of the acoustic driver is 500 Hz, so the output at lower frequencies is of course less strong. Frequencies above 1300 Hz were completely ineffective in premixing the flame or even changing the flame shape (except for the 3100 Hz case). The highest frequency used in the synthetic jet studies reviewed was 1140 Hz (Smith and Glezer, 1998), so synthetic jets do seem to be low-frequency phenomena. However, the behavior from 300 to 800 Hz is not so easy to explain.

Lobed structures indicative of some synthetic jet flow were observed at these intermediate frequencies (as seen in the 500 Hz case in figure 5.4). This implies that similar pulsing and therefore similar premixing was occurring at these intermediate frequencies. However, it was impossible to perform detailed measurements on the flame at these frequencies because the fuel nozzle would rapidly cake with a conical sheet of soot, which obscured the fuel nozzle and radically changed the flame structure. The mechanism causing or preventing the caking at different frequencies remains undetermined.

The broad band in which sound is effective in wrinkling the flame shows that it is unlikely that the premixing effect requires a resonance in the stack, the fuel tube, or any other section of the apparatus. Resonant frequencies are discrete, with non-resonant bands in between, so any phenomenon that happens over a broad frequency range is unlikely to be driven by resonance. The notion of a resonance driving the mixing is not well founded in any case, because a resonance is simply a frequency where pressure and velocity amplitudes are maximized. Driving a cavity at frequencies other than its resonance still leads to oscillating velocities, and driving it hard enough, even off resonance, will produce high amplitude oscillations. Resonant cavities are used in most synthetic jet experiments in order to maximize the particle velocity amplitude at the orifice, but they are simply a tool for amplification. They do not create a situation that cannot be achieved without resonance given sufficient driving power.

The acoustically driven flames investigated in this and other works have shown promise in terms of decreased pollutants and increased efficiency. A clearer understanding of the velocity conditions associated with premixing of the flame would enable the development of design tools for efficient pulsating burners, with acoustic power focused and applied for maximum positive effect.

Such design tools would allow exploitation of this technology in commercial devices.

APPENDIX 1. VARIABLE NOMENCLATURE

A1.1. Arabic Characters

Symbol	Description
A	projected area of a primary or aggregate (e.g. in a micrograph)
a_λ	spectral absorption coefficient
B	axisymmetrically distributed property (from tomographic resonstruction)
C	optical cross section
D	Diameter of a sphere, or unspecified length scale of an aggregate
d_0	diameter of a primary particle
D_{ae}	Aerodynamic equivalent diameter, the diameter of a sphere with the density of water that would have the same settling velocity in air as the particle in question
D_f	fractal dimension
D_{ge}	geometric diameter, the diameter of the smallest sphere that can circumscribe the aggregate
D_{ij}	Deconvolution matrix, for tomographic reconstruction
$E(m)$	function of index of refraction, $E(m)$ = Im [G]
E_a	activation energy, from Arrhenius reaction rate equation
F	Force on a particle
$F(m)$	function of index of refraction, $F(m) = \|G\|^2$
f_{struct}	differential structure function light scattering by aggregates
f	frequency

f_v	volume fraction of soot particles
g	acceleration due to gravity, 9.81 m/s^2
g_{struct}	integrated structure function for light scattering by aggregates
$G(m)$	function of complex index of refraction, $G = (m^2-1)/(m^2+2)$
I	intensity of light
H	function used in the tomographic deconvolution matrix
h	depth of the air cavity in the burner beneath the bead layer
J	mass moment of inertia
k	wave number, $2\pi/\lambda$
k_2	wavenumber for the acoustic wave traveling through the bead layer in the burner
k_a	multiplier used to correct for projection of 3-D aggregates onto 2-D pictures
k_f	fractal prefactor
L	spacing between pulsations in the pulsed flame
M	aggregate mass
m	index of refraction (can be complex)
m_p	mass of solid matter in the bead bed that moves back and forth with acoustic driving
N	number of primaries in a particle
n	number concentration (particles / unit volume)
P	projection of an axisymmetrically distributed property onto a plane
P^+	amplitude of the forward traveling wave in a standing wave field
p_p	volume fraction of beads in the bead bed
q	angle function for aggregate scattering

R	ideal gas constant, 8.314 joule/mol Kelvin
R_{ac}	acoustic reflection coefficient of the burner
R_g	radius of gyration
R_{ge}	Geometric radius, ½ D_{ge}
R_h	Hydraulic radius, the radius of a sphere with the same density as the particle in question which has the same terminal velocity in response to an applied force
R_{stack}	radius of exhaust stack
r	radius
r_i	radius of the ith particle
r_p	pressure drop due to flow resistance through the bead layer
Re_{ac}	Acoustic Reynolds number
S	optical path length
S_{ac}	particle displacement due to oscillating acoustic velocity
T	temperature
U	particle velocity in Stokes' drag law
U_{ac}	oscillating particle velocity due to acoustics
U_{dc}	Constant velocity due to acoustics
U_{jet}	velocity due to fuel jet
U_{tot}	total velocity of flame pulsations
U_{ts}	Terminal settling velocity of a particle in air
W	electrical power to speaker
x	distance from extinction device to centerline of stack
x_p	optical size parameter, $\pi d_p / \lambda$
Z_1	acoustical impedance of the air above the burner surface

Z_2	acoustical impedance of the bead layer
Z_3	acoustical impedance of the air cavity in the burner beneath the bead layer
z	height above the burner surface in the exhaust stack

A1.2. Superscripts and Subscripts

Symbol	Description
$\parallel$	relating to light polarizations parallel to the scattering plane
$\perp$	relating to light polarizations perpendicular to the scattering plane
a	aggregate
abs	optical absorption
ext	optical extinction, absorption plus scattering
p	primary particle
ps	porous sphere model property
RG	Rayleigh Gans scattering
sca	optical scattering
λ	spectral property

A1.3. Greek Characters

Symbol	Description
α	exponent used to correct for projection of 3-D aggregate shapes onto 2-D pictures

β	1 / acoustic boundary layer thickness
δ	ratio of radius of gyration to hydraulic radius
ε_λ	spectral emissivity
ϕ	equivalence ratio
γ	ratio of specific heats
η_v	volume fraction of particles in the sphere circumscribing an aggregate
λ	wavelength
μ	gas viscosity
ν	kinematic viscosity
ρ	density
ρ_a	ratio of optical scattering cross section to optical absorption cross section
ρ_o	density of the base material in an aggregate
τ	optical transmittance

APPENDIX 2. DASCH ERRATA

The methods for 1-D tomographic reconstruction described in (Dasch, 1992) are very important for this work. Unfortunately, there is an error in one of the key equations in that paper that is rather difficult to find. Dasch provided a discussion and errata by personal communication. The errata is reproduced here, because of the inherent non-archival nature of a personal communication.

Tomography of cylindrical objects. Copyright C. Dasch, GM Corp., 1992
Based on C.J. Dasch, Applied Optics Vol. 31, pp. 1146-1152 (1992).
Questions? Contact

Cameron Dasch
Physics Department
General Motors Research and Development Center
Warren, MI 49090-9055
Tel. (810) 986-0588
FAX (810) 986-3091

Misprints in the Applied Optics article (the calculations were correct):

Eq. 7: should be $-2j\ I_{ij}$ not $+2j\ I_{ij}$

Eq. 9: j>i should be $\{[j^2-i^2]^{1/2} + j\}$ not $\{[(j-1)^2 - i^2]^{1/2} + j]$

Eq. 17: upper integral limit is π, not infinity

Eq. 19: $C_1(o,j) = 2\ \pi\ C_2(j)$ not $C_1(o,j) = C_2(j)$

Fig. 7: onion-peeling was calculated for a ring between 7.5 and 14.5 not 7.25 and 14.75.

BIBLIOGRAPHY

Abel, N. H. (1826). Auflosun einer mechanischen Aufgabe. Journal fur die reine und angewandte Mathematik v. 1 p. 153-157.

Allen, M. D. and Raabe, O. G. (1985). Slip Correction Measurements for Aerosol Particle of Doublet and Triangular Triplet Aggregates of Spheres. Journal of Aerosol Science v. 16 n. 1 p. 57-67.

Allen, M. D. and Raabe, O. G. (1985). Slip correction measurements of spherical solic aerosol particles in an improved Millikan apparatus. Aerosol Science and Technology v. 4 p. 269-286.

(ASTM) (1998). Standard Test Method for Impedance and Absorption of Acoustical Materials by the Impedance Tube Method.

Bailo, K. C., Brei, D. E. and Calkins, F. T. (2000). Investigation of PVdF Active Diaphragms for Synthetic Jets. Smart Structures and Materials 2000: Industrial and Commerial Applications of Smart Structures Technologies. J. H. Jacobs, SPIE. 3991.

Benelli, G., Michele, G. d., Cossalter, V., Lio, M. d. and Rossi, G. (1992). Simulation of Large Non-linear Thermo-acoustic Vibrations in a Pulsating Combustor. Twenty-Fourth Symposium (International) on Combustion, The Combustion Institute.

Benítez, J. (1993). Process Engineering and Design for Air Pollution Control. Englewood Cliffs, New Jersey, Prentice-Hall, Inc.

Berry, M. V. and Percival, I. C. (1986). Optics of Fractal Clusters Such as Smoke. Optica Acta v. 33 p. 577-591.

Bird, R. B., Stewart, W. E. and Lightfoot, E. N. (2001). Transport Phenomena. 2nd ed. New York, John Wiley and Sons.

Blackstock, D. T. (2000). Fundamentals of Physical Acoustics. New York, Wiley.

Bockhorn, H. (1994). A Short Introduction to the Problem. Soot Formation in Combustion. H. Bockhorn. Berlin, Springer-Verlag.

Bolt, R. H., Labate, S. and Ingård, U. (1949). The Acoustic Reactance of Small Circular Orifices. Journal of the Acoustical Society of America v. 21 n. 2 p. 94-97.

Cai, J., Lu, N. and Sorensen, C. M. (1993). Comparison of size and morphology of soot aggregates as determined by light scattering and electron microscope analysis. Langmuir v. 9 p. 2861-2867.

Carvalho, J. A., Jr., Ferreira, M. A., Bressan, C. and Ferreira, J. L. G. (1989). Definition of Heater Location to Drive maximum Amplitude Acoustic Oscillations in a Rijke Tube. Combustion and Flame v. 76 p. 17-27.

Chakraborty, B. B. and Long, R. (1968). The formation of soot and polycyclinc aromatic hydrocarbons in diffusion flames III - Effect of additions of oxygen to ethylene and ethane respectively as fuels. Combustion and Flame v. 12 p. 469-476.

Chen, Z.-Y., Meakin, P. and Deutch, J. M. (1987). Comment on "Hydrodynamic Behavior of Fractal Aggregates". Physical Review Letters v. 59 n. 18 p. 2121.

Coe, D. J., Allen, M. G., Smith, B. L. and Glezer, A. (1995). Addressable Micromachined Jet Arrays. The 8th International Conference on Solid-State Sensors and Actuators, Stockholm, Sweden.

Colbeck, I. and Wu, Z. (1994). Measurement of the fractal dimensions of smoke aggregates. Journal of Physics D: Applied Physics v. 27 p. 670-675.

Cook, C. A., Charagundia, S. R., Presser, C., Dressler, J. L. and Gupta, A. K. (1996). Effects of Acoustic Atomization on Combustion Emissions. Proceedings of the ASME Heat Transfer Division, ASME.

Dalzell, W. H. and Sarofim, A. F. (1969). Optical constants of soot and their application to heat flux calculations. Journal of Heat Transfer v. 91 n. 1 p. 100-104.

Dasch, C. J. (1992). One-dimensional tomography: a comparison of Abel, onion-peeling, and filtered backprojection methods. Applied Optics v. 31 p. 1146-1152.

Dasch, C. J. (1992). Tomography of cylindrical objects, and errata for "One Dimensional Tomography", Applied Optics, 1992. By Personal Communication. cameron.j.dasch@gm.com.

Dobbins, R. A. and Megaridis, C. M. (1987). Morphology of Flame Generated Soot as Determined by Thermophoretic Sampling. Langmuir v. 3 p. 254-259.

Dobbins, R. A. and Megaridis, C. M. (1991). Absorption and Scattering of Light by Polydisperse Aggregates. Applied Optics v. 30 p. 4747-4754.

Du, D. X., Axelbaum, R. L. and Law, C. K. (1988). Experiments on the Sooting Limits of Aerodynamically-Strained Diffusion Flames. Twenty-Second Symposium (International) on Combustion, The Combustion Institute.

Dubey, R. K., Black, D. L., McQuay, M. Q. and J. A. Carvalho, J. (1997). The Effect of Acoustics on an Ethanol Spray Flame in a Propane-Fired Pulse Combustor. Combustion and Flame v. 110 p. 25-38.

(EIA) (1997). Annual Energy Review. <http://www.eia.doe.gov/emeu/aer/contents.html>.

(EPA) (1997). Fact Sheet: EPA's Revised Particulate Matter Standards. <http://ttnwww.rtpnc.epa.gov/naaqsfin/pmfact.htm>.

Eroglu, H. and Chigier, N. (1991). Initial Drop Size and Velocity Distributions for Airblast Coaxial Atomizers. Journal of Fluids Engineering v. 113 p. 453-459.

Farias, T. L., Carvalho, M. G., Köylü, Ü. Ö. and Faeth, G. M. (1995). Computational Evaluation of Approximate Rayleigh-Debye-Gans/Fractal-Aggregate Theory for the Absorption and Scattering Properties of Soot. Journal of Heat Transfer v. 117 p. 152-159.

Forrest, S. R. and Jr., T. A. W. (1979). Long-range corrlations in smoke particle aggregates. Journal of Physics A: Mathematical and General v. 12 n. 5 p. L109-L117.

Glassman, I. (1996). Combustion. 3rd ed. San Diego, Academic Press, Inc.

Gordon, S. and McBride, B. J. (1976). Computer program for calculation of complex chemical equilibrium compositions, rocket performance, incident and reflected shocks, and Chapman-Jouget detonations, SP-273, National Aeronautics and Space Administration

Haile, E., Delabroy, O., Lacas, F., Veynante, D. and Candel, S. (1996). Structure of an Acoustically Forced Turbulent Spray Flame. Twenty-Sixth Symposium (International) on Combustion, The Combustion Institute.

Hawthorne, W. R., Weddel, D. B. and Hottel, H. C. (1949). . Third International Symposium on Combustion, Baltimore, Maryland, Williams and Wilkins.

Hecht, E. (1987). Optics. 2nd ed. Reading, Massachusetts, Addison Wesley.

Hess, W., Frisch, H. L. and Klein, R. (1986). On the hydrodynamic behavior of colloidal aggregates. Feitschrift für Physik B - Condensed Matter v. 64 p. 65-67.

Hura, H. S. and Glassman, I. (1988). Soot formation in diffusion flames of fuel/oxygen mixtures. Twenty Second Symposium (International) on Combustion, The Combustion Institute.

Hwang, J. Y., Chung, S. H. and Lee, W. (1998). Effects of oxygen and propane addition on soot formation in couterflow ethylene flames and the role of C3 chemistry. Twenty Seventh Symposium (International) on Combustion, The Combustion Institute.

Ilinskii, Y. (2001). Acoustic Streamin in Standing Waves in a Cylindrical Tube. By Personal Communication. U. o. T. a. A. c/o Professor Mark Hamilton.

Ingård, U. and Ising, H. (1967). Acoustic Nonlinearity of an Orifice. Journal of the Acoustical Society of America v. 42 n. 1 p. 6-17.

Ingård, U. and Labate, S. (1950). Acoustic circulation effects and the nonlinear impedance of orifices. Journal of the Acoustical Society of America v. 22 n. 2 p. 211-218.

Iskander, M. F., Chen, H. Y. and Penner, J. E. (1989). Optical Scattering and Absorption by Branched Chains of Aerosols. Applied Optics v. 28 n. 15 p. 3083-3091.

Ito, H., Fujita, O. and Ito, K. (1994). Agglomeration of soot particles in diffusion flames under microgravity. Combustion and Flame v. 99 p. 363-370.

James, R. D. and Jacobs, J. W. (1996). A Round Turbulent Jet Produced by an Oscillating Diaphragm. Physics of Fluids v. 8 n. 9 p. 2484-2495.

Kang, K. T., Hwang, J. Y. and Chung, S. H. (1997). Soot Zone Structure and Sooting Limit in Diffusion Flames: Comparison of Counterflow and Co-Flow Flames. Combustion and Flame v. 109 p. 266-281.

Kaplan, C., Shaddix, C. R. and Smyth, K. (1996). Computations of Enhanced Soot Production in Time-Varying CH4 / Air Diffusion Flames. Combustion and Flame v. 106 p. 392-405.

Köylü, Ü. Ö. and Faeth, G. M. (1992). Structure of Overfire Soot in Buoyant Turbulent Diffusion Flames at Long Residence Times. Combustion and Flame v. 89 p. 140-156.

Köylü, Ü. Ö. and Faeth, G. M. (1994). Optical Properties of Overfire Soot in Buoyant Turbulent Diffusion Flames at Long Residence Times. Journal of Heat Transfer v. 116 p. 152-159.

Köylü, Ü. Ö. and Faeth, G. M. (1994). Optical Properties of Soot in Buoyant Laminar Diffusion Flames. Journal of Heat Transfer v. 116 p. 971-979.

Köylü, Ü. Ö., Faeth, G. M., Farias, T. L. and Carvalho, M. G. (1995). Fractal and Projected Structure Properties of Soot Aggregates. Combustion and Flame v. 100 p. 621-633.

Ku, J. C., Griffin, D. W., Greenberg, P. S. and Roma, J. (1995). Buoyancy induced differences in soot morphology. Combustion and Flame v. 102 p. 216-218.

Lebedeva, I. V. (1980). Experimental study of acoustic streaming in the vicinity of orifices. Soviet Physics - Acoustics v. 26 n. 4 p. 331-333.

Lin, K.-C. and Faeth, G. M. (1996). Hydrodynamic Suppression of Soot Emissions in Laminar Diffusion Flames. Journal of Propulsion and Power v. 12 p. 10-17.

Lovett, J. A. and Turns, S. R. (1990). Experiments on Axisymmetrically Pulsed Turbulent Jet Flames. AIAA Journal v. 28 n. 1 p. 38-46.

Lovett, J. A. and Turns, S. R. (1993). The Structure of Pulsed Turbulent Nonpremixed Jet Flames. Combustion Science and Technology v. 94 p. 193-217.

Magill, J. (1991). Fractal Dimension and Aerosol Particle Dynamics. Journal of Aerosol Science v. 22S1 p. S165-S168.

Mandelbrot, B. B. (1977). Fractals: Form, Chance, and Dimension. San Francisco, W. H. Freeman and Company.

Mandelbrot, B. B. (1983). Fractal Geometry of Nature. New York, W. H. Freeman and Company.

Margolis, S. B. (1993). The Nonlinear Dynamics of intrinsic Acoustic Oscillations in a Model Pulse Combustor. Western States Section 1993 Fall Meeting, Menlo Park, California, The Combustion Institute.

Martin, K. M. (1997). Acoustic Filtration in a Closed System. Master's Thesis. Available from the General Libraries, The University of Texas at Austin, Austin, Texas.

Martin, K. M. and Ezekoye, O. A. (1997). Acoustic Filtration and Sedimentation of Soot Particles. Experiments in Fluids v. 23 p. 483-488.

Matta, L. M., Zhu, C., Jagoda, J. I. and Zinn, B. T. (1996). Mixing by Resonant Acoustic Driving in a Closed Chamber. Journal of Propulsion and Power v. 12 n. 2 p. 366-370.

Matta, L. M., Zinn, B. T. and Jagoda, J. I. (1997). Experimental Study of Acoustic Velocity Effects on Simulated Solid Fuel Pyrolysis. AIAA Journal v. 35 n. 9 p. 1493-1498.

McEnally, C. S. and Pfefferle, L. D. (2000). Experimental study of nonfuel hydrocarbons and soot in coflowing partially premixed ethylene/air flames. Combustion and Flame v. 121 p. 575-592.

McQuay, M. Q. and Dubey, R. K. (1998). The Interaction of Well-Characterized, Longitudinal Acoustic Waves with a Nonreacting Spray. Atomization and Sprays v. 8 n. 4 p. 419-437.

McQuay, M. Q., Dubey, R. K. and Nazeer, W. A. (1998). An Experimental Study on the Impact of Acoustics and Spray Quality on the Emissions of CO and NO from an Ethanol Spray Flame. Fuel v. 77 n. 5 p. 425-435.

Meakin, P., Chen, Z.-Y. and Deutch, J. M. (1985). The translational friction coefficient and time dependent cluster size distribution of three dimensional cluster-cluster aggregation. Journal of Chemical Physics v. 82 n. 8 p. 3786-3789.

Medalia, A. I. (1967). Morphology of Aggregates I. Calculation of Shape and Bulkiness Factors; Application to Computer Simulated Random Flocs. Journal of Colloid and Interface Science v. 24 p. 393-404.

Medalia, A. I. and Heckman, F. A. (1971). Morphology of Aggregates VII. Comparison Chart Mechod for Electron Microscoping Determination of Carbon Black Aggregate Morphology. Journal of Colloid and Interface Science v. 36 n. 2 p. 173-190.

Mednikov, E. P. and Novitskii, B. G. (1975). Experimental study of intense acoustic streaming. Soviet Physics - Acoustics v. 21 n. 2 p. 152-154.

Megaridis, C. M. and Dobbins, R. A. (1990). Morphological Description of Flame-Generated Materials. Combustion Science and Technology v. 71 p. 95-109.

Megaridis, C. M. and Dobbins, R. A. (1990). Morphological description of flame-generated materials. Combustion Science and Technology v. 71 p. 95.

Meriam, J. L. and Kraige, L. G. (1986). Engineering Mechanics Vol. 2: Dynamics. New York, John Wiley and Sons.

Michel, B. (2000), "MieCalc," http://www.lightscattering.de/MieCalc/eindex.html.

Mitrovic, A. and Lee, T.-W. (1998). Soot formation characteristics of laminar partially premixed flames. Combustion and Flame v. 115 p. 437-442.

Morse, P. M. (1948). Vibration and Sound. second ed. New York, Acoustical Society of America.

Morse, P. M. and Ingard, K. U. (1968). Theoretical Acoustics. New York, McGraw-Hill.

Mountain, R. D. and Mulholland, G. W. (1988). Light Scattering from Simulated Smoke Aggregates. Langmuir v. 4 p. 1321-1326.

Mountain, R. D., Mulholland, G. W. and Baum, H. R. (1986). Simulation of Aerosol Agglomeration in the Free Molecular and Continuum Flow Regimes. Journal of Colloid and Interface Science v. 114 p. 67-81.

Nyborg, W. L. M. (1965). Acoustic Streaming. Physical Acoustics - Principles and Methods. W. P. Mason. New York, Academic Press. IIB: 265-332.

Nyeki, S. and Colbeck, I. (1994). The Measurement of the Fractal Dimension of Individual *In Situ* Soot Agglomerates using a Modified Millikan Cell Technique. Journal of Aerosol Science v. 25 n. 1 p. 75-90.

Palacios, C., Martin, K. M. and Ezekoye, O. A. (2001). Correlation of Aerodynamic and Geometric Particle Size Properties of Soot Generated by an Acetylene Diffusion Flame. Second Joint Meeting of the U.S. Sections of the Combustion Institute, Oakland, CA, Western States Section of the Combustion Institute.

Panton, R. L. (1984). Incompressible Flow. 1st ed. New York, John Wiley and Sons.

Parikh, P. G. and Moffat, R. J. (1981). Mixing Improvement in a Resonantly Pulsed, Confined Jet. Fluid Mechanics of Combustion Systems. T. Morel, R. P. Lohmann and J. M. Rackley. New York, ASME: 251-256.

Parker, W. G. and Wolfhard, H. G. (1950). Carbon Formation in Flames. Journal of the Chemical Society v. 21 p. 2038-2049.

Ponizy, B. and Wojcicki, S. (1984). On Modeling of Pulse Combustors. Twentieth Symposium (International) on Combustion, The Combustion Institute.

Pont, G., Cadou, C. P., Karagozian, A. R. and Smith, O. I. (1998). Emissions Reduction and Pyrolysis Gas Destruction in an Acoustically Driven Dump Combustor. Combustion and Flame v. 113 p. 249-257.

Poppe, C., Sivasegaram, S. and Whitelaw, J. H. (1998). Control of NO_X Emissions in Confined Flames by Oscillations. Combustion and Flame v. 113 p. 13-26.

Puri, R., Santoro, R. J. and Smyth, K. C. (1994). The Oxidation of Soot and Carbon Monoxide in Hydrocarbon Diffusion Flames. Combustion and Flame v. 97 p. 125-144.

Rayleigh, J. W. S. (1945). The Theory of Sound. 2nd ed. New York, Dover Publications.

Rizzetta, D. P., Visbal, M. R. and Stanek, M. J. (1999). Numerical Investigation of Synthetic-Jet Flowfields. AIAA Journal v. 37 n. 8 p. 919-927.

Rogak, S. N. and Flagan, R. C. (1990). Stokes Drag on Self-Similar Clusters of Spheres. Journal of Colloid and Interface Science v. 134 n. 1 p. 206-218.

Rosemount Analytical Inc. (1997). Model 400A Hydrocarbon Analyzer Instruction Manual. Anaheim, CA.

Rosemount Analytical Inc. (1997). Model 880A Non-Dispersive Infrared Analyzer Instruction Manual. Anaheim, CA.

Rosemount Analytical Inc. (1997). Model 951A NO/NO$_X$ Analyzer Instruction Manual. Anaheim, CA.

Samson, R. J., Mulholland, G. W. and Gentry, J. W. (1987). Structural analysis of soot agglomerates. Langmuir v. 3 p. 272-281.

Santoro, R. J. and Miller, J. H. (1987). Soot Particle Formation in Laminar Diffusion Flames. Langmuir v. 3 n. 2 p. 244-254.

Santoro, R. J., Semerjian, H. G. and Dobbins, R. A. (1983). Soot Particle Measurements in Diffusion Flames. Combustion and Flame v. 51 p. 203-218.

Santoro, R. J., Yeh, T. T., Horvath, J. J. and Semerjian, H. G. (1987). The Transport and Growth of Soot Particles in Laminar Diffusion Flames. Combustion Science and Technology v. 53 p. 89-115.

Schuster, K. and Matz, W. (1940). Über Stationäre Strömungen im Kundtschen Rohr (On Stationary Streaming in Kundt Tubes). Akustische Zeitschrift v. 5 n. 6 p. 349-352.

Shaddix, C. R., Harrington, J. E. and Smyth, K. C. (1994). Quantitative Measurements of Enhanced Soot Production in a Flickering Methane / Air Diffusion Flame. Combustion and Flame v. 99 p. 723-732.

Siegel, R. and Howell, J. R. (1992). Thermal Radiation Heat Transfer. Third ed. Washington, Hemisphere Publishing.

Smith, B. L. and Glezer, A. (1998). The Formation and Evolution of Synthetic Jets. Physics of Fluids v. 10 n. 9 p. 2281-2297.

Smyth, K. C., Harrington, J. E., Johnsson, E. L. and Pitts, W. M. (1993). Greatly Enhanced Soot Scattering in Flickering CH4 / Air Diffusion Flames. Combustion and Flame v. 95 p. 229-239.

Smyth, K. C. and Shaddix, C. R. (1996). the Elusive History of m=1.57-0.56 i for the Refractive Index of Soot. Combustion and Flame v. 107 p. 314-320.

Strayer, B. A., Dunn-Rankin, D. and Jabbari, F. (1998). A Comparison Between Frequency and Amplitude Modulated Adaptive Control of a Non-Premixed Flame. Twenty-Seventh Symposium (International) on Combustion, Pittsburgh, The Combustion Institute.

Sujith, R. I., Chen, F., Daniel, B. R., Jagoda, J. I. and Zinn, B. T. (1992). Acoustic Characteristics of Pulse Combustor Mixing Chambers. Twenty-Forth Symposium (International) on Combustion, The Combustion Institute.

Sujith, R. I., Waldherr, G. A., Jagoda, J. I. and Zinn, B. T. (1996). On the Effect of Evaporation on Droplet Drag. Journal of Fluids Engineering v. 118 p. 862-864.

Sujith, R. I., Waldherr, G. A. and Zinn, B. T. (1995). An Exact Solution for One-Dimensional Acoustic Fields in Ducts with an Axial Temperature Gradient. Journal of Sound and Vibration v. 184 n. 3 p. 389-402.

Thurston, G. B. and Charles E. Martin, J. (1953). Periodic Fluid Flow through Circular Orifices. Journal of the Acoustical Society of America v. 25 n. 1 p. 26-31.

TSI (1997). Model 3302A Diluter Instruction Manual. St. Paul, Minnesota.

TSI (1997). Model 3320 Aerodynamic Particle Sizer Spectrometer Instruction Manual. St. Paul, Minnesota.

van de Hulst, H. C. (1981). Light Scattering by Small Particles. New York, Dover.

Westervelt, P. J. (1953). The Theory of Steady Rotational Flow Generated by a Sound Field. Journal of the Acoustical Society of America v. 25 p. 60-67.

Wiltzius, P. (1987). Hydrodynamic Behavior of Fractal Aggregates. Physical Review Letters v. 58 n. 7 p. 710--713.

Zinn, B. T. (1992). Pulse Combustion: Recent Applications and Research Issues. Twenty-Fourth Symposium (International) on Combustion, Pittsburgh, The Combustion Institute.

VITA

Karl Matthew Martin was born in Virginia Beach, Virginia on December 6, 1972, the son of Beverly S. (Buddy) and Jean T. Martin. He grew up in Virginia Beach, where he attended Princess Anne High School, graduating as salutatorian. He entered Virginia Polytechnic Institute and State University (Virginia Tech) in the fall of 1990. He worked as a cooperative education student for E. I. Dupont de Nemours company in Richmond, Virginia. He graduated summa cum laude from Virginia Tech in May 1994, and married his wife, Cheryl, in the same month. He was employed at Electro-Tec Corporation in Blacksburg, Virginia as a design and testing engineer until entering graduate school at the University of Texas at Austin in the fall of 1995. In December 1997 he received his Master's Degree in Mechanical Engineering. In January 2000 he started work at Nanotechnologies, Inc., a nanoparticle manufacturing startup company in Austin, Texas. He currently holds the position of engineering manager at Nanotechnologies, and will continue to work there after graduation.

Permanent Address: 3928 Sierra Drive
Austin, TX 78731

This thesis was typed by the author.